الجمهورية الجزائرية الديمقراطية الشعبية
People's Democratic Republic of Algeria
وزارة التعليم العالي والبحث العلمي
Ministry Of Higher Education & Scientific Research

University of Echahid Hamma Lakhdar,
El-oued
Faculty of Exact Sciences
Department of physics
Ref/./P/2022.

جامعة الشهيد حمّه لخضر الوادي
كلية العلوم الدقيقة
قسم الفيزياء
المرجع:.Ref//P/2022

A thesis submitted for the fulfillment of
the degree of

Doctorate of Science

Option: physics

Green synthesis and characterization of Fe2O3 nanoparticles using Phoenix dactylifera L leaf extract and their applications.

Presented by :

Asma Labbi

The public thesis defense on 14 /5 / 2023

Board of Examiners :

Dr. Beggas Azzeddine	**MCA**	**Chairperson**	**University of El-Oued.**
Pr. Benhaoua Boubaker	**Professor**	**Supervisor**	**University of El-Oued.**
Pr. Abdallah Attaf	**Professor**	**Examiner**	**University of Biskra.**
Pr. Lakel said	**Professor**	**Examiner**	**University of Biskra.**
Pr. Benramache said	**Professor**	**Examiner**	**University of Biskra.**
Dr. Rahal Achour	**MCA**	**Examiner**	**University of El-Oued.**

- إهـــداء -

الحمد لله رب العالمين والصلاة والسلام على خاتم الأنبياء والمرسلين

الحمد لله الذي أنار لنا درب العلم والمعرفة وأعاننا ووفقنا إلى انجاز هذا العمل الذي أهديه إلى:

إلى من غمراني بالدفء والحنان وعلماني الصبر والمثابرة "ماما "مليكه" و" بابا "محمد علي"

رحمه الله واسكنه فسيح جناته.

إلى أولادي: محمد وعبد النور.

إلى إخوتي: "ياسين" قدوتي، و"عزّ الدين" و"وليد" و"أحمد" وأختاي: "إيمان و"آمنة".

إلى جدتي العزيزة "عائشة".

إلى كافة الأهل والأقارب خاصة خالي عادل ومحمد.

إلى كافة الصديقات والزميلات.

إلى كل من علمني بدأً من معلمي الابتدائية ثمّ أساتذة المتوسطة والثانوية وأخيرا أساتذة الجامعة.

إلى كل من يطلب العلم والمعرفة.

Acknowledgments

First of all, I would like to thank God Allah for giving me strength, courage, patience and serenity during all these years of study.

I wish to express my sincere gratitude to my supervisor Prof. Benhaoua BOUBAKER, who have been a constant source of guidance, support and encouragement throughout my Project. his extensive knowledge, rigorous research attitude, diligent working and creative thinking have inspired me and will definitely benefit my career.

My deepest gratitude is also due to the members of the jury: Dr. Beggas Azzeddine, Prof. Abdallah Attaf., Prof. Lakel said, Prof. Benramache said and Dr. Rahal Achour, for serving as my committee members and taking the time to revise my thesis. I am thankful that in the midst of all their activity, they accepted to be members of the reading committee.

I also want to express my special appreciation to my parents (Malika&Mohammed Ali) for their love and continued support. I also want to thank all my family ; my children, my sisters (Amena and Imene) and my brothers (Ahmed, Walid, Ezzeddine and Yacine), and all my family and friends for their support and encouragement.

Finally to anybody who attempts to develop the ideas presented here, I hope they can be of use.

Asma Labbi

Green synthesis and characterization of Fe2O3 nanoparticles using Phoenix dactylifera L leaf extract and their applications.

Abstract

Green synthesis of metal oxide nanoparticles using plant extracts. It is a promising alternative to the traditional method of chemical synthesis.The present work aims to develop and characterize oxide nanoparticles from iron by green chemistry process using phoenix leaf extract Dactylifera L. leaves ethanolic extract as polyphenols source and $FeCl_3$aqueoussolution as the precursor, where the volume ratio was 1/2. The concentration of $FeCl_3$ was varied from 0.01M–0.02M–0.03M–0.04M. To characterize the obtained iron oxide NPs XRD, SEM, UV-VIS and FTIR technics were used.

XRD analyses shows the existence of three iron oxide NPs essentials compounds: maghemite phase, hematite phase and Fe_2O_3While the grain size was varied in 22.91-37.40nm, 20.41–31.32nm and 17.96–25.25nm respectively. SEM images analysis showed that all sample having. Where UV-VIS analysis showed that the variation of the concentration of $FeCl_3$had an effect on direct band gap in the range 2.162–2.358eV. FTIR study confirms the abundance of Fe-O bond in all samples.

Also The effect of annealing time within the extract and the 500°C annealed products for (0–3) hours for concentrations0.03M on their structural and optical properties have been studied.

XRD analyses avowed the formation tow of irons oxides before annealing treatment, namely magnetite and wüstite. Also show the existence of three iron oxide essentials compounds after annealing treatment, namely maghemite, hematite and β-Fe_2O_3 with concentration 0.03M. SEM images showed that all samples having spherical shaped particles. With direct band gap in the range of 2.031-2.732eV. FTIR spectrum affirms the abundance of Fe-O bond.

Keywords: NPs of Fe_2O_3, Maghemite Fe_2O_3, Hematite Fe_2O_3, beta phase β-Fe_2O_3, Magnetite Fe_3O_4, Wüstite, green synthesis, PHEONIXDACTYLIFERA.L.

Synthèse verte et caractérisation de nanoparticules de Fe2O3 à l'aide d'extrait de feuille de Phoenix dactylifera L et leurs applications.

Résumé

Synthèse verte de nanoparticules d'oxydes métalliques à partir d'extraits de plantes. C'est une alternative prometteuse à la méthode traditionnelle de synthèse chimique. Le présent travail vise à développer et caractériser des nanoparticules d'oxyde de fer par procédé de chimie verte en utilisant l'extrait de feuilles de phénix Dactylifera L. extrait éthanolique de feuilles comme source de polyphynols et une solution aqueuse de FeCl3 comme précurseur, où le rapport volumique était de 1/2. La concentration de FeCl3 variait de 0,01 M-0,02 M-0,03 M-0,04 M. pour carectériser les NP d'oxyde de fer obtenues, des techniques XRD, SEM, UV-VIS et FTIR ont été utilisées.

Les analyses XRD montrent l'existence de trois composés essentiels des NPs d'oxyde de fer: la phase maghémite, la phase hématite et Fe2O3 Alors que la taille des grains variait en 22,91-37,40 nm, 20,41-31,32 nm et 17,96-25,25 nm respectivement. L'analyse des images SEM a montré que tous les échantillons avaient. Où l'analyse UV-VIS a montré que la variation de la concentration de FeCl3 avait un effet sur la bande interdite directe dans la gamme 2.162-2.358eV. L'étude FTIR confirme l'abondance de la liaison Fe-O dans tous les échantillons.

De plus, l'effet du temps de recuit dans l'extrait et les produits recuits à 500°C pendant (0-3) heures pour concentrations 0,03 M sur leurs propriétés structurelles et optiques a été étudié.

Les analyses XRD ont avoué la formation d'oxydes de fer avant le traitement de recuit, à savoir la magnétite et la wüstite. Montrer également l'existence de trois composés essentiels d'oxyde de fer après traitement de recuit, à savoir la maghémite, l'hématite et le β-Fe2O3 pour les concentrations 0,03 M. Les images SEM ont montré que tous les échantillons avaient des particules de forme sphérique. Avec une bande interdite directe dans la plage de 2.031-2.732eV. Le spectre FTIR confirme l'abondance de la liaison Fe-O.

Mots clés: NPs de Fe2O3, Maghémite Fe2O3, Hématite Fe2O3, phase bêta β-Fe2O3, Magnétite Fe3O4, Wüstite, synthèse verte, PHEONIXDACTYLIFERA.L.

التوليف الأخضر وتخليق الجسيمات النانوية Fe2O3 باستخدام مستخلص أوراق النخيل(Pheonixdactylifera. L) وتطبيقاتها.

الملخص

يعتبر التوليف الأخضر لجسيمات أكسيد المعادن النانوية باستخدام المستخلصات النباتية بديل واعد للطريقة التقليدية للتوليف الكيميائي. يهدف العمل الحالي إلى تخليق جسيمات أكسيد الحديد النانوية بواسطة عملية الكيمياء الخضراء باستخدام مستخلص أوراق النخل .Dactylifera L مستخلص الأوراق الإيثانولي كمصدر متعدد الفينول ومحلول FeCl3 المائي بنسبة حجم 2/1 و بتركيز متغير من (0.01 - 0.02 - 0.03 - 0.04) مول. لدراسة خصائص جسيمات أكسيد الحديد النانوية المحضرة استخدمت تقنيات XRD و SEM و UV-VIS وFTIR .

أظهر تحليل الأشعة X وجود ثلاثة مركبات أساسية من أكسيد الحديد النانوية : الطور غاما ، الطور الفا و β-Fe2O3 بينما تباين الحجم الحبيبي لجسيمات أكسيد الحديد النانوية : 22.91-37.40 نانومتر ، 20.41-31.32 نانومتر و 17.96-25.25 نانومتر على التوالي. وأوضحت صور الماسح ألمجهري الالكتروني أن جميع الجسيمات المحضرة لهل شكل كروي. وأظهر تحليل الأشعة فوق البنفسجية (UV-VIS) أن اختلاف تركيز الملح كان له اثر على فجوة النطاق المباشرة في المجال 2.162-2.358 إلكترون فولت . كما تؤكد أطياف الأشعة الحمراء (FTIR) وفرة الرابطة Fe-O في جميع العينات المحضرة.

وتمت دراسة ايضا تأثير زمن التلدين عند 500درجة مئوية لمدة (0-3) ساعات للعينات المحضرة بتركيز: 0.03 مول على الخواص التركيبية والبصرية. أقر تحليل الأشعة X على تكوين أكاسيد الحديد النانوية قبل المعالجة بالتلدين وهما أكسيد الحديد الأسود والويستيت. وأظهر أيضًا وجود ثلاثة مركبات أساسية من أكسيد الحديد بعد المعالجة بالتلدين وهي الميغاميت و الهيماتيت وβ-Fe2O3 للعينات المحضرة بتركيز 0.03 مول. وأظهرت صور الماسح ألمجهري الالكتروني أن جميع العينات تحتوي على جسيمات كروية الشكل. مع فجوة نطاق مباشرة في حدود 2.031-2.732 إلكترون فولت . ويؤكد طيف FTIR على وفرة رابطة Fe-O .

كلمات مفتاحية: جسيمات أكسيد الحديد النانوية ، الميغاميت ، الهيماتيت ، β-Fe2o ، المغنتيت ، الوستيت ، التخليق الأخضر ، .Pheonixdactylifera.L

List of figures

List of tables

List of Abbreviations

TiO_2	titanium dioxide
ZnO	zinc oxide
Bi_2O_3	bismuth oxide
Cu_2O_3	copper dioxide
Fe_2O_3	iron (III) oxide
AF	antiferromagnet
WF	ferromagnetism
XRD	X-ray diffraction
SEM	scanning electron microscopy
FTIR	fourier Transform Infrared Spectroscopy
$FeCl_3$	iron chloride
L.E.L.E	liquid ethanolic leaves extract
FWHM	the full width at half-maximum
Eg	band gap,

List of Symbols

Ag	silver
Au	gold
ZnO	oxides of some metals such as zinc oxide
CuO	copper oxide
TC	curie temperature
T_{t1}, T_{t2}	transition temperatures
T_m	melting temperature
Fe^{2+}	ferrous ions
Fe^{3+}	ferric ions
α-Fe_2O_3	hematite
Fe_3O_4	magnetite
γ-Fe_2O_3	maghemite
λ	the wavelength of the X-rays.
d	the interreticular distance.
θ	the angle of incidence of the X-rays
D	the grain size in nm.
β	the width at half height expressed in radians.
I_0	intensity of incident light.
I	intensity of light transmitted by the sample solution.
c	sample concentration.
l	sample path length.
ε	molar absorption coefficient.
I/I_0	ratio is known as the transmittance (T) and the logarithm of the inverse ratio
hv	the photon energy.
E_g	the band gap energy of the sample
d_{hkl}	the inter-planer distance
hkl	Miller indices
'*a*' and 'c'	the values of lattice parameter '*a*' and 'c'
D	the crystallite size
β	the full width at half-maximum
α	the absorption parameter
h	Planck constant
v	the photon frequency
E_g	gap energy
A	is a constant and

Table of Contents

Chapter **Title** **Page N°.**

General Introduction

In the last years, nanoparticles taking a lots of interest because of their use in the medical environment and related laboratory applications due to their physical properties which offers a higher intrinsic reactivity of their surface sites area [1]. And because the NPs have an enhanced magnetic, optical, electronic, catalytical and biological properties that differ from those in the solid or partial materials, due to their size and shape characteristics, the NPs are widely used in a different fields applications; especially in the biomedical field (treatment of hyperthermia for cancer cells), in molecular biology (DNA and cell purification, protection of human cells from ultraviolet rays), in earth science and in the industry sector; they have made it possible to develop applications in magnetic recording, magnetic refrigeration, magnetic printing, catalysis, ion recovery, magnetic membranes, gas detectors, bacterial reagents, treatment of water from microbial contamination, the stability and non-toxic nature of the iron oxides make them suitable for use as coatings [2].

There are many physical and chemical methods are implied to the synthesis of iron oxide NPs, which use toxic chemicals such as the reaction of iron (II) salts or iron (III) with sodium borohydride as a reducing factor [3–4], vacuum sputtering [5], and the decomposition of irons precursors in organic solvents [6], but these methods are expensive and use special equipment that require high energy and involve hazardous, corrosive and flammable chemicals materials [7]. Moreover, using the above–mentioned methods are likely to arise conglomerates that reduce the surface reactivity and instability of these particles [8]. Also, the sizes, morphologies, shapes, compositions and cristalinty of nano materials, are depend on the used techniques, are highly affect the products properties. The cited methods suffered from an inability to control NPs size. Composition and size control need others methods such as green ones. It is worth noting that green synthesis are adopted for this purposes due to greater stability of the products and to their low costs and no toxic yield. Stability of the products refers to phytochemical compounds from food sources such as peel [9], fruits [10], and seeds [11]. Palm leaves

(DACTYLIFERA L) are fewly used to synthesis NPs [12]. Eventhough green synthesis of iron nanoparticles has emerged using different parts of the plant and herbal materials (such as stems, roots, leaves, and seeds), which are a simple, low cost, more safety, and environmentally friendly compared to the previous cited methods [13].

The metal oxides morphology can be affected by several factors, the most important of which are: the effect of the ratio between the plant extract and the precursor [12], the effect of extract plant [14], the effect of precursor concentration [15], the effect of precursor type [16], the effect of the solvent [17], the effect of the reaction time [18], the effect of the temperature of the reaction [19], the effect of PH [20], the effect of the annealing time [21], the effect of the annealing temperature [22].

After a general introduction to the undertaken work and the presented literature review, the main plan of the thesis is structured as follows:

An arts of state is presented in chapter 1. Chapter 2 presents the methodology of synthesis and characterization techniques. Chapter 3 presents study the physical properties of iron oxides nanoparticles greenly synthesized by reacting the ethanolic extract of Phoenix dactylifera. L with different iron chloride ($FeCl_3$) salt concentration in aqueous solution. Chapter 4 provides a to study the physical properties of iron oxides nanoparticles greenly synthesized by reacting the ethanolic extract of Pheonix dactylifera. L with concentration 0.03 M of iron chloride ($FeCl_3$) salt in aqueous solution With the change of annealing time at 500°C for (0-3) hours. The contributions of the dissertation along with the scope for future research in this area find a place in general conclusion.

References

[1] Zhang, Xin, et al. "Kaolinite-supported nanoscale zero-valent iron for removal of Pb2+ from aqueous solution: reactivity, characterization and mechanism." Water Research 45.11 (2011): 3481-3488.

[2] El Mendili, Yassine. Etude des propriétés structurales et magnétiques de nanoparticules de maghémite dispersées dans une matrice de silice. Diss. Université du Maine, 2011.

[3] Zhang, Rui, and P. Somasundaran. "Advances in adsorption of surfactants and their mixtures at solid/solution interfaces." Advances in colloid and interface science 123 (2006): 213-229.

[4] Wang, Chuan-Bao, and Wei-xian Zhang. "Synthesizing nanoscale iron particles for rapid and complete dechlorination of TCE and PCBs." Environmental science & technology 31.7 (1997): 2154-2156.

[5] Kuhn, L. Theil, et al. "Structural and magnetic properties of core–shell iron–iron oxide nanoparticles." Journal of Physics: Condensed Matter 14.49 (2002): 13551.

[6] Karlsson, M. N. A., et al. "Size-controlled nanoparticles by thermal cracking of iron pentacarbonyl." Applied Physics A 80 (2005): 1579-1583.

[7] Shahwan, Talal, et al. "Green synthesis of iron nanoparticles and their application as a Fenton-like catalyst for the degradation of aqueous cationic and anionic dyes." Chemical Engineering Journal 172.1 (2011): 258-266.

[8] O'Carroll, Denis, et al. "Nanoscale zero valent iron and bimetallic particles for contaminated site remediation." Advances in Water Resources 51 (2013): 104-122.

[9] Wei, Yufen, et al. "Green synthesis of Fe nanoparticles using Citrus maxima peels aqueous extracts." Materials Letters 185 (2016): 384-386.

[10] Rostamizadeh, Elham, et al. "Green synthesis of Fe 2 O 3 nanoparticles using fruit extract of Cornus mas L. and its growth-promoting roles in Barley." Journal of Nanostructure in Chemistry 10 (2020): 125-130.

[11] Rahmani, Reyhaneh, et al. "Green synthesis of 99mTc-labeled-Fe3O4 nanoparticles using Quince seeds extract and evaluation of their cytotoxicity and biodistribution in rats." Journal of Molecular Structure 1196 (2019): 394-402.

[12] Berra, D., et al. "Green synthesis of copper oxide nanoparticles by pheonix dactylifera l leaves extract." Digest Journal of Nanomaterials and Biostructures 13.4 (2018): 1231-1238.

[13] Rahmani, Reyhaneh, et al. "Green synthesis of 99mTc-labeled-Fe3O4 nanoparticles using Quince seeds extract and evaluation of their cytotoxicity and biodistribution in rats." Journal of Molecular Structure 1196 (2019): 394-402.

[14] Stozhko, Natalia Yu, et al. "The effect of the antioxidant activity of plant extracts on the properties of gold nanoparticles." Nanomaterials 9.12 (2019): 1655.

[15] Ayed, Rihab Ben, Mejda Ajili, and Najoua Kamoun Turki. "Physical properties and Rietveld analysis of Fe2O3 thin films prepared by spray pyrolysis: effect of precursor concentration." Physica B: Condensed Matter 563 (2019): 30-35.

[16] Limaye, Amit U., and Joseph J. Helble. "Effect of precursor and solvent on morphology of zirconia nanoparticles produced by combustion aerosol synthesis." Journal of the American Ceramic Society 86.2 (2003): 273-278.

[17] Qin, Xiao, et al. "Flame synthesis of Y2O3: Eu nanophosphors using ethanol as precursor solvents." Journal of materials research 20.11 (2005): 2960-2968

[18] Karade, V. C., et al. "Effect of reaction time on structural and magnetic properties of green-synthesized magnetic nanoparticles." Journal of Physics and Chemistry of Solids 120 (2018): 161-166.

[19] Samy, Ahmed, Amal E. El-Sherbiny, and A. A. Menazea. "Green synthesis of high impact zinc oxide nanoparticles."Egyptian Journal of Chemistry 62.The First

International Conference on Molecular Modeling and Spectroscopy 19-22 February, 2019 (2019): 29-37.

[20] Zamri, Muhammad Syahin Firdaus Aziz, and Norzahir Sapawe. "Effect of pH on phenol degradation using green synthesized titanium dioxide nanoparticles." Materials Today: Proceedings 19 (2019): 1321-1326.

[21] Jafari, A., et al. "Effect of annealing temperature on magnetic phase transition in Fe3O4 nanoparticles." Journal of Magnetism and Magnetic Materials 379 (2015): 305-312

[22] Laid, Tedjani Mohammed, et al. "Optimizing the biosynthesis parameters of iron oxide nanoparticles using central composite design." Journal of Molecular Structure 1229 (2021): 129497.

CHAPTER I

Arts of state

I.1. Introduction:

This chapter presents a bibliographic study on Green synthesis of nano-materials, metal oxides and the photo catalyzes. It is divided into three parts.

The first one presents different methods for the green synthesis of nanoparticles. The second one concerns the properties of metal oxides. In which bibliographical elements concerning structural the phases of iron Oxide and magnetic properties and electrical and optical properties of these oxides will be presented, which make such oxides interesting for different fields of application. The third part of the chapter presents principle of photo catalysis and photo-catalytic degradation of pollutants using iron oxide.

I.2. Green synthesis of nano-materials:

I.2.1. Introduction:

The origin of the word "nano" is Greek, which means "dwarf". Also nano is one part of a billion, and therefore nanometer(nm) is equivalent 10^{-9}m.It is known that nanomaterials do not exceed 100nm in dimensions [1]. A science which deals with the applications of these nanomaterials is called the science of nanotechnology [2].

Recently, green synthesis technique to obtain nanoparticles using plants and microorganisms has gained wide interest and great attraction because it is biologically safe, environmentally friendly and cost-effective [3-5], and it is considered as an important tool for reducing the devastating effects associated with traditional methods [6].Nanoparticles have many applications in various fields including biomedicine, catalysis, chemical industries, cosmetics, drug delivery, electronics, environment, energy sciences, food and feed, healthcare, mechanics, optics, space industries, non-

linear optical devices, single-electron transistors, and photo-electrochemical sciences [7-9].

I.2.2. Methods for the synthesis of nanoparticles:

There are two methods of nanoparticle synthesis: **Construction from top to bottom and Upward construction from bottom to top.** The first one starts from the larger structure of matters is broken down into small pieces using chemical, physical and biological energy such as milling and techniques of lithography and spraying. The second in which substances are synthesized from their ions using chemical, physical or biological reactions. Such as chemical vapor deposition, sol-gel processes, spray pyrolysis, laser pyrolysis, atomic/molecular condensation, and green synthesis [10].

I.2.3. Biological components for “green” synthesis:

The physical and chemical methods used in the manufacture of nanoparticles are blamed for that they take longer, and use harmful substances and dangerous solvents that may be difficult to get rid of, and their effects remain in the environment, in addition to their great need for energy. On the contrary, green synthesis requires relatively low energy and is cost-effective [11].

The nanoparticles morphology can be affected by several factors, including the effect of the ratio between the plant extract and precursor [12], the extract plant [13], the precursor concentration of metals salts [14], the precursor type [15], the extracting solvent [16], the reaction time [17], the temperature of the reaction [18], the PH [19], and the annealing time and annealing temperature [20, 21].

A biosynthesis of nanoparticles is carried out using microorganisms (bacteria, fungi, yeasts...) or plant extracts. Organisms have advanced to endure in environments with high concentrations of minerals [22–23]. These organisms may change the chemical nature of toxic metals by reducing their toxicity or making them non-toxic [24–26]. Nanoparticles constitute the "result" of the organism's resistance mechanism in contrast to a specific metal. The synthesis of "natural" bio-metal nanoparticles is divided into two categories.

(a) Bio reduction: More stable forms of metal ions can be achieved by chemical reduction using biological means and is achieved by reducing exchange metals. The metal ion is reduced and the enzyme is oxidized [27]. This ends

up producing powerless metallic nanoparticles that can be recovered without damage from a contaminated sample.

(b) Bio sorption: Metal ions bind to the same organism from a water sample or soil sample. Either the metal ions are bound to the cell wall or the peptides are synthesized by some plants, bacteria and fungi, and these synthesized peptides assemble into stable nanostructures [28].

I.2.3.1. Bacteria:

Bacteria possess the ability to reduce metal ions and are momentous candidates in nanoparticles preparation [29]. Bacterial species have been generally utilized for commercial biotechnological applications such as bioremediation, bioleaching, and genetic engineering [30]. An example is the synthesis of silver nanoparticles from bacteria Bacillus cereus, It is used as antibacterial activity against Escherichia coli, Pseudomonas aeruginosa, Staphylococcus aureus, Salmonella typhimurium, and Klebsiella pneumoniae bacteria [31].

I.2.3.2. Fungi:

Fungal-mediated biosynthesis of metallic/metal oxide nanoparticles is also a very efficient process for the generation of monodisperse nanoparticles with well-defined shapes. They serve as better biological agents for the preparation of metal oxide and metal nanoparticles, due to the presence of a diversity of enzymes within cells [32]. A larger amounts of nanoparticles can be synthesized using competent fungi than bacteria [33]. Moreover, fungi have many advantages over other organisms because of the presence of enzymes/proteins/reductive components on their cell surfaces [34]. The possible mechanism of metal nanoparticle formation is enzymatic reductase in the cell barrier or inside the fungal cell [6]. Several fungal species are used to synthesize metal/metal oxide nanoparticles such as silver which was used as bactericidal and catalytic [35]. Gold which was used as biomedical field [36]. Titanium dioxide which was used as catalysis, bio-sensing, drug delivery, molecular diagnostics, solar cell, optoelectronics, cell labeling, and imaging [37]. Zinc oxide which was used as plant nutrient fertilizer [38].

I.2.3.3. Yeast:

Yeasts are single-celled microorganisms found in eukaryotic cells. A total of 1500 species of yeast have been identified [39]. Yeasts can absorb a large quantity of deadly metals from their surroundings due to their wide surfaces [40–41].

The biosynthesis of silver and gold nanoparticles by a silver-tolerant yeast strain and Saccharomyces Cerevisiae broth has been reported which was used as catalysis [42].

I.2.3.4. Plants:

Plants contain organic compounds such as flavonoids, amino and carboxylic acids, ketones, phenols and proteins [43]. These materials play an important role in the recovery of mineral salts and the production of nanoparticles in easy, fast and environmentally safe ways. The green synthesis of nanoparticles was achieved using different parts of the plants such as roots, seeds, leaves, stems, flowers, peels, and fruits.

I.2.3.4.1. Mechanism of green synthesis of nanoparticles by plant extracts:

In general, the metal bio reduction mechanism in plant extracts includes three main phases: activation phase, growth phase and termination phase.

- The primary step is the activation phase in which metal ions are recovered from their salt precursors by the action of plant metabolites, biomolecules with reduction capacities. In addition, the metal ions change from a mono- or divalent oxidation state to a zero valence state and the nucleation of the reduced metal atoms takes place [44].
- The growth phase, referring to the spontaneous coalescence of nanoparticles in which small adjacent nanoparticles spontaneously unite into larger particles, which is accompanied by an increase in the thermodynamic stability of the nanoparticles [45].
- The final step of synthesis is the termination phase during which the nanoparticles reach their maximum possible activity, this process is strongly influenced by the ability of a plant extract to stabilize the metallic nanoparticles [46].

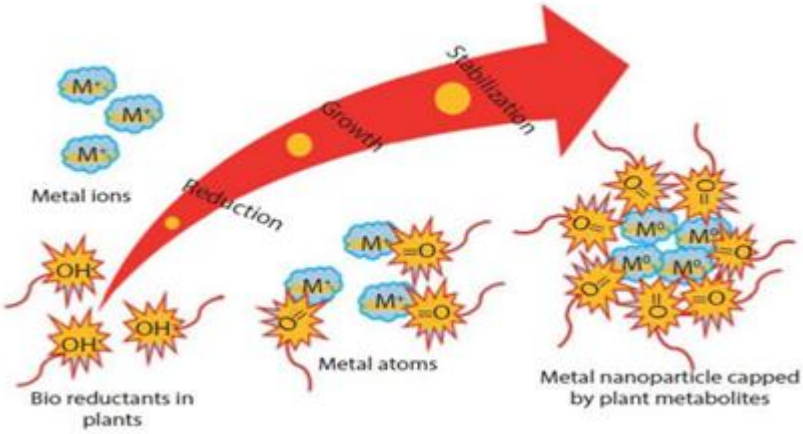

Figure I.1: *Mechanism of green synthesis* [47].

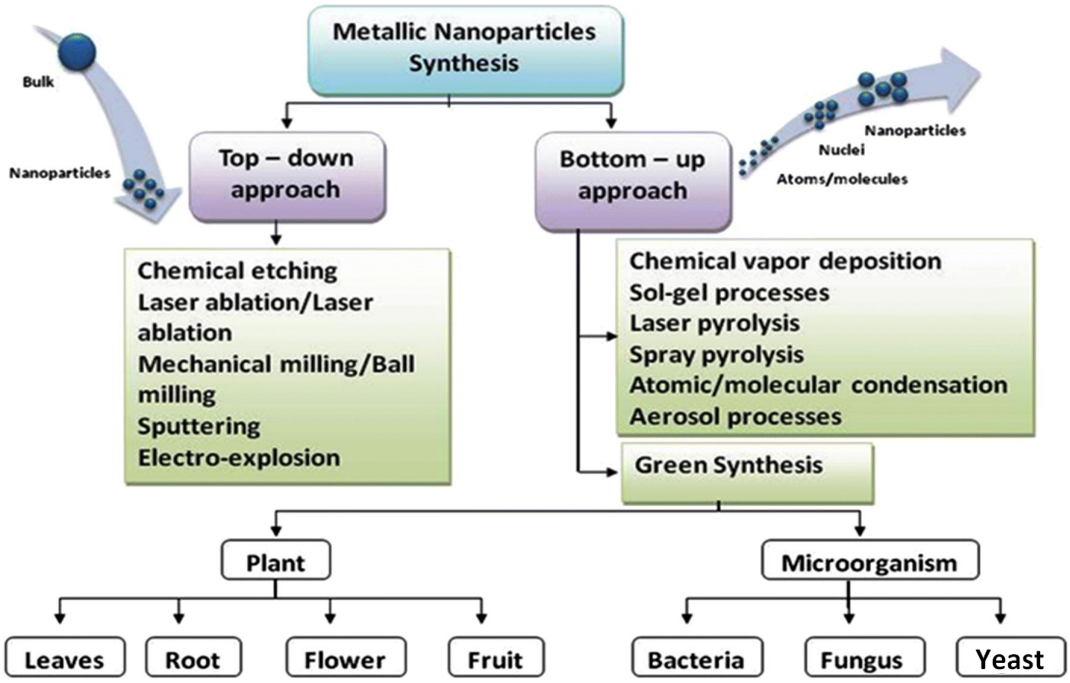

Figure I.2: *summarizes the methods for nanoparticles synthesis [6].*

For the production of nanoparticles of many metals that the most important of them are silver (Ag) and gold (Au) and oxides of some metals such as zinc oxide (ZnO), copper oxide (CuO), iron oxides, and so on. Among of those, aqueous extract of ginger root (Zingiber officinale L) was used to synthesize silver nanoparticles [48], these particles have been shown to be effective in the laboratory against cancer cells. Also the aqueous extract of pomegranate seeds (Punica granatumm L) was used to synthesize silver nanoparticles [49]. Indian Sidr leaf (Ziziphus mauritiana) extract was

used to synthesize nano-copper oxide; it has been shown to be effective as an anti-microbial and anti-cancer [50]. The extract of the leaves, stems and flowers of basil (Ocimum basilicum L) was used in the manufacture of zinc oxide particles [51]; these particles had an inhibitory effect on the growth of bacteria and of fungi. In another study, banana peels (Musa acuminate L) were used to synthesize zinc oxide particles [52]. Wolfberry Chinese fruit (Lycium Chinense Mill) extract was used to synthesize gold nanoparticles [53].

I.2.4. Nanoparticles applications:

Nanomaterials in general and nanoparticles in particular are used in different fields due to their specific properties. In the following some of these applications will be described.

I.2.4.1.Catalysis:

Nanoparticles have a large specific surface area which offers higher catalytic activity. Due to their extremely high surface area to volume ratio, nanoparticles behaves as an effective catalyst in the production of chemicals.

One of the important applications is the use of platinum nanoparticles in automotive catalytic converters, as they reduce the amount of platinum required due to the very large specific surface area of nanoparticles, thus significantly reducing cost and improving performance [54].

I.2.4.2. Environment:

Owing unique physical and chemical properties, nanoparticles were taken as an ideal choice for their use in today environmental treatment. The use of nanomaterials is envisaged for the reduction of pollutant emissions, the treatment of effluents, in particular by photo catalysis and gas purification, and the production of ultra-pure water from seawater.

Nan remediation is one of the effective solutions since it offers in situ treatment eliminating the need to pump groundwater for treatment and the need for excavation to reach the target destination. Nanoparticles are injected at the desired location and are transported along the groundwater flow and decontaminate the water by immobilizing contaminants [55].

I.2.4.3. Food:

Improved production, processing, protection and packaging of food is achieved through the integration of nanotechnology. For example, a nanocomposite coating in a food packaging process can directly introduce the antimicrobial substances onto the surface of the coated film. Its most important applications too, which include sensory enhancements (improvement in flavor and color and change in texture), increased absorption, delivery targeted nutrient bioactive compounds, stabilization of active ingredients like nutraceuticals in food sources, product enhancement to extend the shelf life of shells, sensors for food safety and antimicrobials to eliminate pathogenic microbes in food [56].

I.2.4.4. Medicine:

Nanomedicine helps in early detection and prevention, improved diagnosis and monitoring of disease. The invention of nanoparticles like gold nanoparticles has made gene sequencing less difficult. They are also used to detect genetic sequences when they adhere to short segments of DNA. Damaged tissue can be repaired or reproduced using nanotechnology. Magnetic nanoparticles have been shown to be effective in isolating and grouping stem cells. Quantum dots, on the other hand, have been used for molecular imaging and stem cell tracing [57].

I.2.5. Botanical description:

The date palm Phoenix Dactylifera L is a dioecious perennial fruit tree from arid, tropical or semi-tropical regions, the fruit of which or the date is eaten. Archaeologists show from pinnate fossils that the date palm dates back only to the early Tertiary. This palm is the only plant capable of providing such a high food production in arid regions.

I.2.5.1. Taxonomy:

The date palm was named Phoenix Dactylifera by Linnaeus in 1734.The term Phoenix derived from Phoinix, name of the date palm among the ancient Greeks who considered it to be the tree of the Phoenicians [58]; Dactylifera comes from the Latin dactylis, deriving from the Greek dactylus, meaning finger (due to the shape of the fruit), associated with the Latin word fero, carried, with reference to fruits [59].

From a botanical point of view, the date palm is an angiosperm, dioecious tree monocotyledon of the Arecaceae family [60]. This family is represented by 200

genera and 2700 species divided into six families [61]. The subfamily of Coryphoideae isitself subdivided into three tribes [62].

I.2.5.2. Systematic:

According to DJERBI [63], the classification of the date palm in the plant kingdom ispresented below:

Figure I.3: *Photo of Phoenix Dactylifera L.*

- Group: Spadiciflores;
- Order: Arecals;
- Family: Arecaceae;
- Subfamily: Coryphoideae;
- Tribe: Pheniceas;
- Genre: Phoenix;
- Species: Phoenix dactylifera L.

Fig.I.3 shown a photo of Phoenix Dactylifera L. from Nakhla (Date Palm tree).

Vernacular names:

Nakhla (Arabic), Date Palm (French), Phoenix (Greek), Date (English), Datter (Italian), Khajur and Pinda (Hinde) [59].

I.2.6. Morphology of the date palm:

The date palm occupies a strategic place in oasis development, thanks to its remarkable adaptation to climatic conditions, the high nutritional value of its fruits and also its invaluable ecological and socio-economic roles.

The date palm is a perennial species with a very long lifespan (around 100 years) with a juvenile phase of around 8 years [64].It is a large palm tree 20 to 30 m high, it is composed of a root system of the fasciculate type, the stipe, the palms and the floral organs which arise from the development of the axillary buds located in the armpit of the palms in the coronary region of the trunk (Fig.I.4) [58].

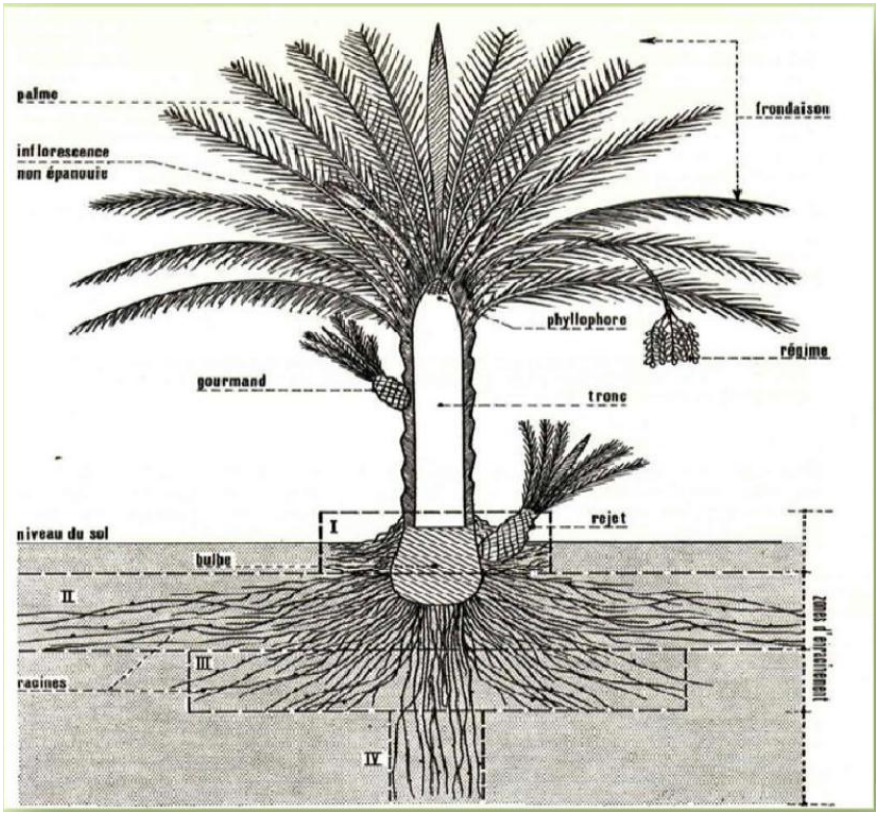

Figure I.4: *Morphology of the date palm.*

I.2.6.1. The root system:

The root system of the palm is dense fasciculate type, formed of several types of roots, the diameter of which does not exceed 1.5 cm and which emerge partially above ground level to a height of up to 50 cm from the base of the trunk[58].

It is divided into 04 root zones. The extension of these four rooting zones depends on the nature of the soil, the method of cultivation, the depth of the water table, the variety cultivated and the origin of the plant.

- **Zone 1 (Respiratory roots):** Located at the foot of the date palm, contains numerous aerial adventitious roots which can develop from the basal region of the trunk. These roots play a respiratory role thanks to the presence in their cortical part of numerous airy voids or lenticels which allow gas exchange with the air in the soil atmosphere [65]. They are located in the surface layer of the soil between 20 cm and 25 cm deep.
- **Zone 2 (Roots of nutrition):** It is very extensive, with the strongest proportion of system roots. These are provided with numerous rootlets. These roots grow from 20 cm to 1 m deep.
- **Zone 3 (Absorption roots):** Is more or less important depending on the method of cultivation and the depth of the groundwater level. They develop between 1 to 2 m deep.
- **Zone 4 (Deep roots):** The importance of this zone depends on the depth of the water table. If it is shallow, this area merges with the previous one. On the other hand, if the water table is deep, the roots of this zone can reach 3 to 6 m deep.

I.2.6.2. The vegetative system:

The vegetative system is made up of the parts described below:

I.2.6.2.1. The trunk:

The terms "stipe" or "trunk" refer to the main axis that supports a tree. The stipe is usually cylindrical, unbranched, lignified and brownish-brown in color.

The diameter can reach 100 cm and the height 35 m, an average adult date palm with a trunk 60 cm in diameter and 8 m in height [66]. These variations in diameter are evidence of the biological life of the palm tree [65].

I.2.6.2.2. Buds:

In the axil of each palm, there is an axillary bud which can develop to give rise to a rejection, at the base of the stipe or aerial attached to the trunk, commonly called “rkeb” in the basal part of the tree or an inflorescence in the upper part. Most vegetative axillary buds end up aborting during the juvenile phase of the palm. The apical or terminal bud is responsible for the height growth of the palm and the development of leaves and axillary buds [67].

I.2.6.2.3. Fins:

The palm or Djérid are compound leaves, pinnate, they come from a terminal bud, each year it appears 10 to 20, up to 30 [58]. They can reach 2 to 6 m in length and have a lifespan of 3 to 7 years. There are 50 to 200 fins premature tree approx.

There are four parts to an adult palm (Fig. I.5):

- The petiole part: very wide, terminated by a sheath which surrounds the trunk.
- The rachis: along which the leaflets, pinnae and thorns are positioned.
- The thorny part: which occupies the base of the palm. The stiff, tapering spines are isolated or in groups of two or three.
- The pinnate part: making up the major part of leaflets arranged regularly in an oblique position along the rachis.

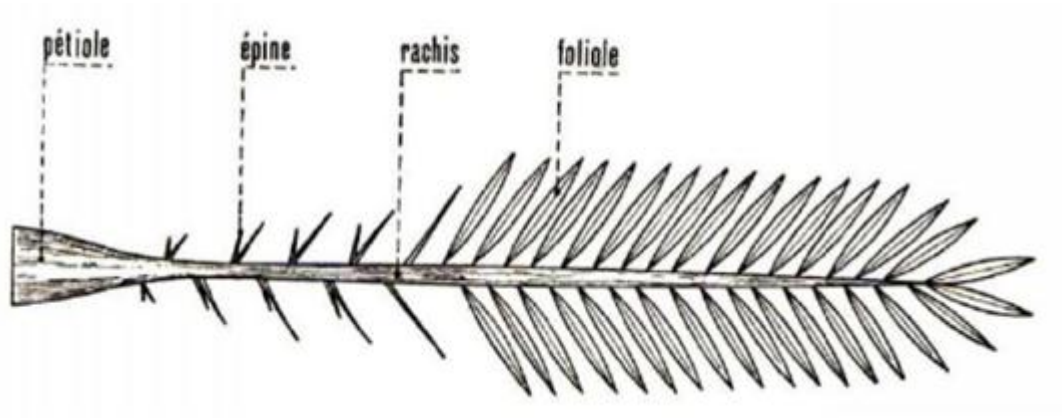

Figure I.5: *Diagram of an adult palm* [58].

I.2.6.3. Reproductive apparatus:

I.2.6.3.1. Flowers:

The flowers of the palm are grouped in inflorescence. They are unisexual with a very short peduncle, ivory-green, yellow-green depending on the sex and cultivar or variety [68].

The evil flower is of a slightly elongated shape, it consists of a calyx formed by three fused sepals, a corolla formed by three petals slightly elongated and ending in a point, of six stamens and it has a characteristic odor [58].

I.2.6.3.2. The fruit:

The fruit of the date palm, the date is a berry containing a single seed, commonly called a kernel. After fertilization, the ovum evolves to give a green fruit (the size of a pea then of a grape fruit up to the normal size of the date) [68].

The date consists of a fleshy mesocarp, protected by a thin pericarp, the stone is surrounded by one endocarp per chimney. The latter is elongated, more or less bulky with a ventral groove, the embryo is dorsal and its consistency is hard and Korean.

I.2.7. Interest and importance of date palms:

The date palm in arid regions of the world is the most important plant both economically and socially.

I.2.7.1. Economic importance:

Date palms are among the most useful plants in the agricultural economy of countries in tropical areas. All parts of these plants are used in a variety of ways.

– Dates can be used for the preparation of many food products including date paste, jam, syrup, sugar, honey, alcohol, vinegar, flour (dietetic products, animal feed) [69].

– The date kernel, which contains 23.2% fat and 5.8% protein, is crushed to be fed to animals [70].

– The trunk provides firewood and construction material. The sap that flows from the incised stipe is used in the preparation of a drink called palm wine or lagmi which can be drunk fresh or fermented [71].

– Dry fins used as fences, windbreaks, in the making of baskets, hats, etc., they can even be used in the paper industry [72].

World production of dates is approximately 7 million tonnes per year. This places the date in fourth place among tropical and subtropical fruit productions, after citrus fruits, bananas and pineapples.

The number of date palms in the world is estimated at more than 130 million trees distributed mainly in the Near East and North Africa [46].

The main producers of the most important dates are: Egypt, Iran, Saudi Arabia, the Arab Emirates, Iraq, Pakistan, Algeria and Sudan.

Algeria is one of the most important date-producing countries and ranked sixth in the world with an annual production between 6,302,810 and 710,000 tonnes, more than 48% of which is represented by the variety Déglet Nour [73].

Deglet-Nour is a commercial variety of good quality that is often exported, while the common varieties are of less economic importance and of which the most widespread are: Ghars, Degla-Beïda and Mech-Degla.

In Algeria, the area occupied by the cultivation of the date palm covers 160,000 ha which currently represents more than 18 million palm trees.

The phoenicultural regions are generally located south of the Saharan Atlas. The wilaya of Biskra is the first phoenicultural region and is followed by the wilaya of El Oued with respectively 27.4% and 25% of the total area [74].

I.2.7.2. Therapeutics:

In addition to its production of dates for human consumption, the date palm offers a wide range of treatments used by the Saharan population, namely:

- Rich in fiber, dates facilitate intestinal transit and play a preventive role in colorectal cancer, appendicitis, diverticulosis, varicose veins and hemorrhoids [69].
- High in energy value, the fruit helps fight anemia and demineralization.
- Pollen is used to treat infertility problems in men and women.
- The syrup (robb) is used for nervous diseases and in bronchopulmonary diseases [69].

I.3. Metal oxides:

An oxide is any chemical compound containing one or more oxygen atoms. Metals are materials that have unique properties such as excellent electrical and thermal conductivity, light reflectivity, flexibility and ductility. Metal oxides are crystalline solid compounds, containing a metal cation an oxide anion. The oxidation number of oxygen is -2, and it is basically an anion where the metal is the cation. The number of oxygen atoms that bond with the metal ion depends on the oxidation number of the metal ion [75]. Metal oxides are among the most common compounds found in nature.

These compounds have basic properties and important technological applications that have made them extremely important since their discovery in industrial life. They were used in the past in making ceramic pottery, but recently the demand for them

increased with the emergence and development of nanotechnology that developed many It has physical, chemical and biological properties, as it has been used in various industries such as installing electronic circuits, sensors, destroying cancer cells, pollution control, fuel cells, gas detectors, as well as in the field of solar energy [76–77].

Several methods have been developed to observe the nanometric structure of metallic oxides, after conducting many researches recently [78]. The most important of these oxides in nature are: titanium dioxide (TiO_2), zinc oxide (ZnO), bismuth oxide (Bi_2O_3), copper dioxide (Cu_2O_3) and iron(III) oxide (Fe_2O_3) [77–79].

I.3.1. Iron and Iron Oxides:

I.3.1.1. Iron:

Iron is the most abundant metal and common chemical element on Earth, this element has been known since ancient times, and played a crucial role in the development of our civilization as the basis of countless structural material components. It can be found simply in nature in the form of molecular complexes, colloids, oxides and hydroxides. Moreover, the iron atom is also present in the biological components such as haemoglobin. They are widely used in various fields such as metallurgy, collar dyes, magnetic materials, and catalysts... etc [75].

In pure form it is a dense magnetic metal, has a high melting point, good thermal conductivity, and a low coefficient of linear expansion. Iron is a transition element with an atomic number (Z = 26). Its [Ar]3d64s2 electronic structure is characterized by two stable states of oxidation (+II and +III). Natural iron contains four stable nuclides: 54 Fe (5.845%), 56 Fe (91.754%), 57 Fe (2.119%), and 58 Fe (0.282%) [76].

I.3.1.2. Iron Oxides:

Iron oxides are chemical compounds composed of iron and oxygen and are the most abundant elements on Earth. Iron oxides are very common compounds that are widely found in nature. It is found almost everywhere in the atmosphere, in the earth's crust (rocks, ore), in water (erosion by water, rivers ...), and in living organisms (human body, animals, plants) ...etc. There are a number of iron oxides, hydroxides, and indoxy-hydroxides, as summarized in Table. I.1, This group of iron hydroxides ("oxy") is often referred to as *iron oxides* [78].

Table. I.1: ist of iron oxides, hydroxides and oxyhydroxides [78].

Oxides	Hydroxides	Oxy-hydroxides
FeO, iron(II) oxide(wüstite)	**Iron(II) hydroxide ($Fe(OH)_2$)**	**Goethite (α-FeOOH)**
Fe_3O_4, iron(II,III) oxide (magnétite)	**Iron(III) hydroxide($Fe(OH)_3$) (bernalite)**	**Akaganéite (β-FeOOH)**
Fe_2O_3, iron(III) oxide		**Lepidocrocite (γ-FeOOH)**
α-Fe_2O_3, Hématite		**Feroxyhyte (δ-FeOOH)**
β-Fe_2O_3		**Ferrihydrite($Fe_5HO_8{\cdot}4H_2O$ approx)**
γ-Fe_2O_3, maghemite		
ε-Fe_2O_3		

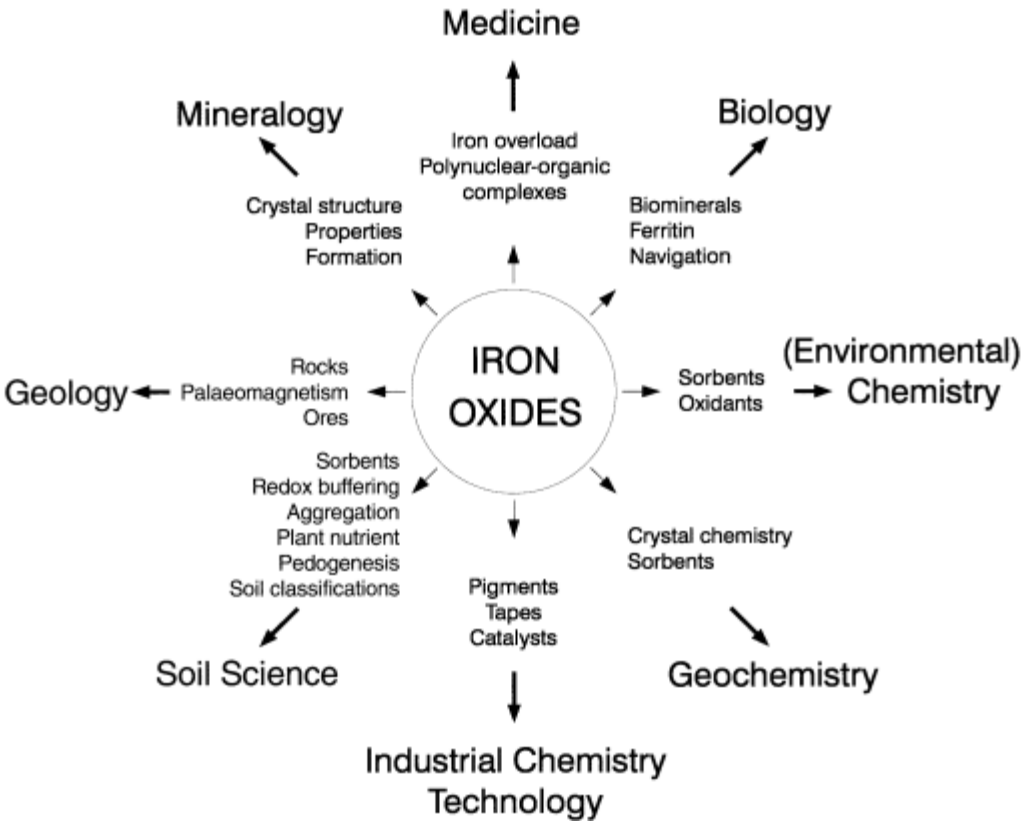

Figure I.6: *The multidisciplinary nature of iron oxide research* [89].

Iron oxides and hydroxides are among the most well-known metal oxides, and they are also naturally rich. There are sixteen known iron oxides and oxyhydroxides that can be easily synthesized in the laboratory, and their class of compounds contains a rich palette of oxygen-to-iron ratios, as well as many different phases for each formulation [78]. ron compounds are of interest in a variety of scientific uses, such as corrosion science, catalysts, soil remediation, pure chemistry, and industrial chemistry

[77, 80, 81]. And in the medical fields for antibacterial applications [82–84]. The stability and non-toxic nature of iron oxides makes them suitable for use as paints and pigments [85–86]. Previous studies have shown that sand covered with iron oxide has a high efficiency in removing a range of pollutants from water/wastewater [87–88]. As pigments, iron oxides have colors from yellow to brown and black; This color change has been proposed to change the electronic structure with the configuration [85]. Because of the wide range of iron oxide applications, it is necessary to prepare iron oxides in the laboratory in order to verify their special physical and chemical properties. Fig. I.6 Explains the applications of different scientific disciplines in which iron oxides are used [89].

I.3.3. The Phases of Iron Oxide:

Iron ions have two valences: ferrous ions (Fe^{2+}) and ferric ions (Fe^{3+}). These ions decompose as a function of pH and/or temperature to form, by means of oleon oxidation mechanisms, different phases depending on the reaction conditions (Fig. I.7). The stability domains of these phases, shown in this diagram (Fig. I.7), are valid for a solid at thermodynamic equilibrium. Therefore, this type of scheme should be considered with caution in the case of thin films and nano-materials [78].

Among the phases of the Fe-O binary system, the main forms of pure iron are α-Fe, γ-Fe, wüstite $Fe_{1-x}O_x$, and spinel iron including magnetite and hematite α-Fe2O3. Under standard conditions of pressure and temperature (p = 1.013 bar and T = 300 K), the α-Fe, Fe_3O_4 and α-Fe_2O_3 phases are stable. Among these, the formation of α-Fe_2O_3 is preferred by the partial pressure of atmospheric oxygen.

There are 6 iron oxides made up of Fe and O: hematite (α-Fe_2O_3), magnetite (Fe_3O_4), maghemite (γ-Fe_2O_3), (β-Fe_2O_3), (ε-Fe_2O_3), and Wüstite (FeO). In most of these compounds, iron is in a trivalent state, but FeO and Fe_3O_4 contain Fe^{2+} (II). Iron (III) oxide or ferric iron has four polymorphs, and only two of them are found in nature as the minerals hematite (α-Fe_2O_3) and maghemite (γ-Fe_2O_3), but the others two (β-Fe_2O_3, ε-Fe_2O_3) can only be found as synthetic nanoparticles. Each polymorph has unique magnetic properties that make it suitable for specific applications, for example at room temperature α, β, γ, and ε-Fe_2O_3 show weak ferromagnetism, paramagnetic, ferrimagnetism, and non-collinear ferrimagnetism or canted anti-ferromagnetism respectively [76, 90].

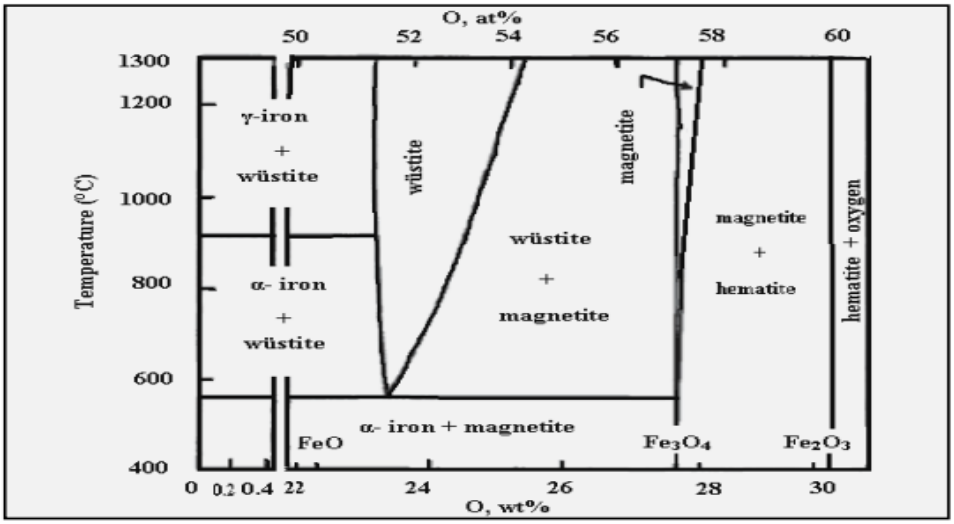

Figure I.7: *Phase diagram of iron and its oxides* [78].

I.3.3.1. α-Fe_2O_3 (Hematite):

The α-Fe2O3 is the oldest known iron oxide mineral and is widely found in rocks and soils. Finely divided α-Fe_2O_3 is blood red (Greek haima = blood) and shimmering black or gray if coarsely crystallized [91], It is very stable and is often the end product of the transformation of other iron oxides. The is also known by names such as iron (III) oxide, ferric oxide, iron sesquioxide, red ocher, spéculante, mirror iron ore, kidney ore, saffron-mart, and martite.

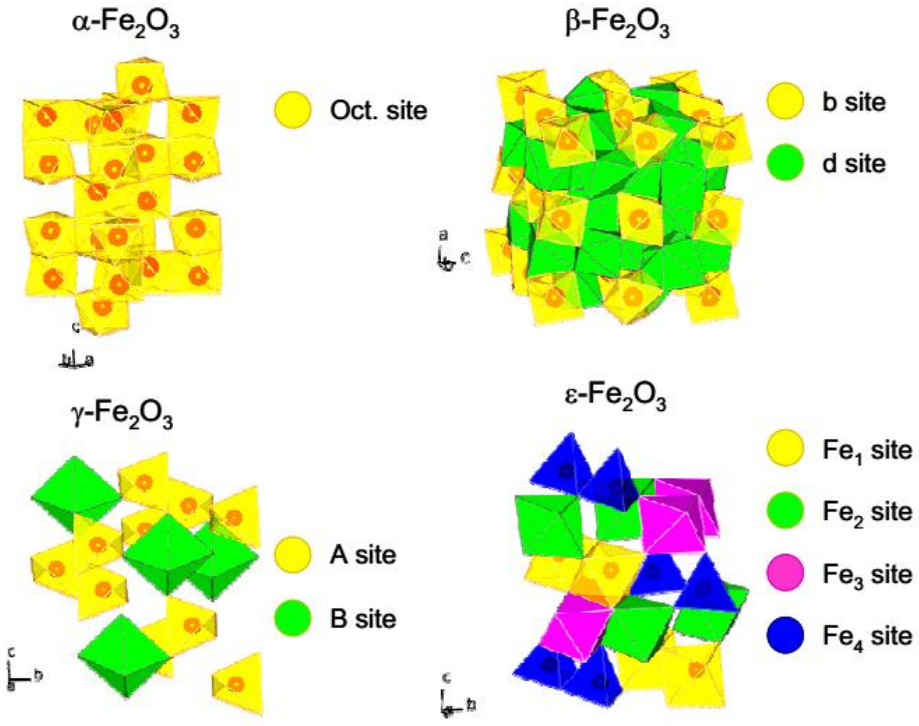

Figure I.8: *Polyhedral representation of the iron (III) oxide polymorph, showing the crystalline positions of the ferric ions for each polymorph* [90].

This polymorph is found in nature as the mineral hematite, is isomorphic with corundum (α-AI_2O_3) based on its anion packing, and has a central rhombic hexagonal structure (structure with corundum), in which Fe^{3+} two-thirds octahedral ions occupy the octahedral sites (Fig. I.8). The crystallization structure corresponds to the R3c space group, with lattice parameters a = 5.036 Å and c = 13.749 Å, and six formula units for each cell unit. The sharing of three edges and one face between the FeO_6 octahedral is responsible for distorting the cationic sub-lattice from the perfect packing.

The magnetic order of hematite changes with the change of temperature, and it has two magnetic transition temperatures: the Morin temperature (TM) and the Néel temperature (TN). The magnetic transition temperatures of bulk hematite have values of TM ~ 260 K and TN ~ 950 K [78, 91].

Morin temperature varies with particle size and decreases rapidly when particle size is less than 100nm [86–87]. Under the TM hematite behaves as an anti-ferromagnet (AF), in which the spins lie along the electric field gradient and the crystal c-axis. When the temperature is increased above the TM, the spins spin in their direction to ~90° with respect to the c-axis and the ferromagnetic subshells are aligned to the maximum parallel, with ~5° canting between the spins, giving weak ferromagnetism (WF) to hematite. Weak ferromagnetism remains up to 950 K (TN), and above this temperature hematite behaves as a paramagnet [78]. Fig.I.9 shows the crystal structure of hematite

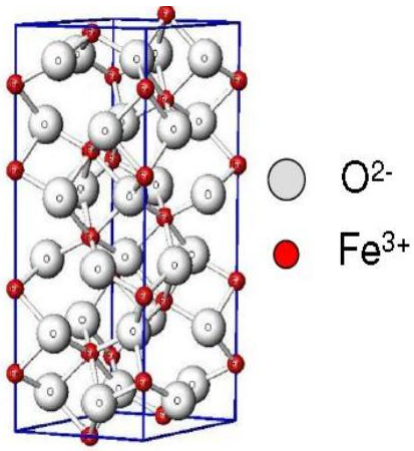

Figure I.9: *crystal structure of hematite* [91].

I.3.3.2. β-Fe_2O_3:

This is a stable polymorph of ferric oxide, never found naturally but synthetically prepared as powders [88–90] or thin films [2]. The β-Fe_2O_3 has a "bixbyite" structure, in which Fe3+ ions occupy two non-equivalent octahedral sites (Fig. I.8). In the unit cell, 32 iron ions are distributed in the b and d sites, which have a ratio of d/b = 3. It crystallizes in the space group *Ia*3, with a lattice constant *a* = 9.393 Å, and 16 formula units per unit cell. At room temperature, this polymorph is magnetic, but has a magnetic transition at lower temperature (T_N ~ 100-119 K). Below T_N, β-Fe_2O_3 has ant ferromagnetic behavior [77–78].

I.3.3.3. γ-Fe_2O_3 (Maghemite):

Like hematite, this polymorph is found in nature as a mineral maghemite. It has an inverse spinel structure (is structural with magnetite), where Fe^{3+}ions occupy tetrahedrally (A) and octahedral (B) sites as is shown in Fig.I.8. The crystalline structure of maghemite contains vacancies, in octahedral sites to compensate the excess of positive charge. the γ-Fe_2O_3 has a cubic unit cell *Fdm*3 for randomly distributed vacancies with a lattice constant value (*a* =8.339 Å).While the structure of the maghemite can be approximated as a cubic cell of composition $(Fe^{3+})_8[Fe^{3+}_{5/6}\square_{1/6}]_{16}O_{32}$ [92]. Each cell of γ-Fe_2O_3, contains 32 O^{2-} ions, (21+1/3) Fe^{3+} ions and (2 +2/3)vacancies.Where the parentheses () and [] designate tetrahedral and octahedral sites [93].

Maghemite, which has two magnetic sub lattices, shows a ferromagnetic behavior. It has a high magnetic response when is placed under an external magnetic field. From extrapolation is possible to estimate the value of T_C ~ 790 – 980 K, but it is not possible to do its experimental measurement because of its thermal instability. Thus, above a certaintemperature (300 – 900 °C) maghemite irreversibly transforms to the most stable polymorph, *i.e.* hematite.

The variation in transition temperature is affected by multiple factors such as particle shape, size, and crystallinity [92]. The size of the maghemite particles plays an important role in its magnetic properties when particles are smaller than 10 nm they show super paramagnetic relaxation and make them useful for several applications. Fig.I.10 presents of diagram illustrating the crystalline structure of γ-Fe_2O_3.

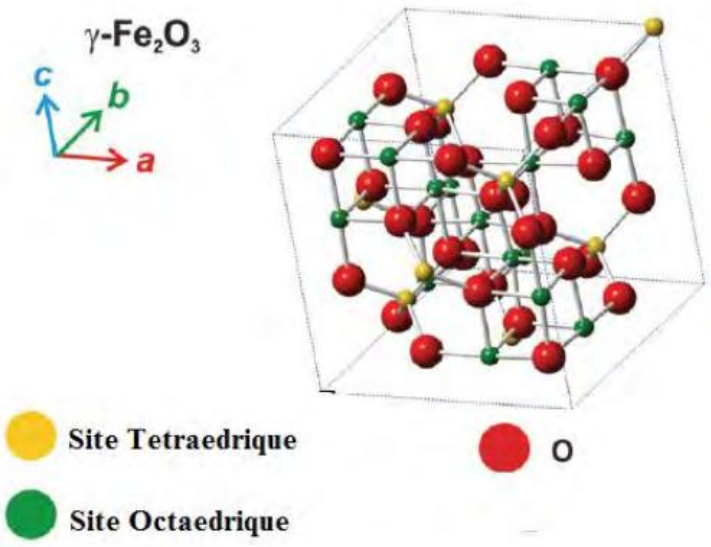

Figure I.10: *Diagram illustrating the crystalline structure of γ-Fe_2O_3*[78].

I.3.3.4. ε-Fe_2O_3:

This polymorph of ferric oxide has been found only at nano metric scale, and it is Possible to synthesize, usually inside a matrix, with different morphologies: nanoparticles, rods, and wires [76,94]. This polymorph, ε-Fe_2O_3, can be considered as an intermediate phase between maghemite and hematite. The crystalline structure of ε-Fe_2O_3 is orthorhombic, and it can be described with the space group *Pna*2_1,lattice parameters a = 5.095 Å, b = 8.789 Å, c = 9.437 Å, and eight formula units per unit cell. In the unit cell, the ferric ions occupy three octahedral non-equivalent sites (Fe_1, Fe_2,and Fe_3) and one tetrahedral site (Fe_4), without any vacancies in its structure, as depicted in Fig. I.8 [78, 95].

There are known two magnetic transitions for ε-Fe_2O_3, one at 495 K (T_C) and at110 K. When the temperature is less than 110 K, ε-Fe_2O_3 behaves as a met magnet, *i.e.* a material that increases considerably its magnetization with a small change of temperature[76]. At 110 K there are structural transformations and spin reorientation phenomena[95], but there is not an agreement about the kind of magnetism displayed, it is said to benon-collinear ferrimagnet or canted anti-ferromagnet [94]. Finally, above T_C ε-Fe_2O_3becomes paramagnetic. Another interesting characteristic of this polymorph is its giant coercive field (0.8 – 4.1 T) at room temperature, probably due to its disordered crystalline structure [95].

I.3.3.5. Fe_3O_4(Magnetite):

The (Fe_3O_4) contains both Fe^{2+} and Fe^{3+} ions is a black color ferromagnetic material having an inverse spinel structure. (Fe_3O_4) is an important iron ore and is responsible for the magnetic properties of rocks. (Fe_3O_4) is also known with other names for eg. black iron oxide, magnetic iron ore, iron (II, III) oxide, loadstone (when natural polarity is present), tri-iron oxide, ferrous ferrite, Hercules stone and magneteisenerz (German) [89].

The (Fe_3O_4) has an inverse spinel structure(space group *Fd3m*) with a face-centered cubic unit cell based on 32 O^{2-} ions which are regularly cubic closed-packed along the [111] directions. The lattice constant has value a=8.39 Å. There are eight formula units per unit cell in (Fe_3O_4) structure [96–97]. (Fe_3O_4) differs from the most of the other iron oxide as it contains both Fe^{2+} and Fe^{3+} ions. Its formula is written as $B[AB]O_4$ where A= Fe^{2+}, B=Fe^{3+}, and the brackets denote octahedral sites [89, 96]. Magnetite contains iron in both divalent and trivalent states. As a result, the compound exhibits unique electric and magnetic properties based on the transfer of electrons between Fe^{2+} and Fe^{3+}within the octahedral sites. Magnetite is metastable and will convert to maghemite under exposure to temperatures typically around 200°C. Further heating to above 400°C will produce α-Fe_2O_3.Hematitecan reduce back to magnetite by reacting with hydrogen gas elevated temperatures and pressures. It is interesting to note that magnetite is only thermodynamically stable in its bulk form [96].

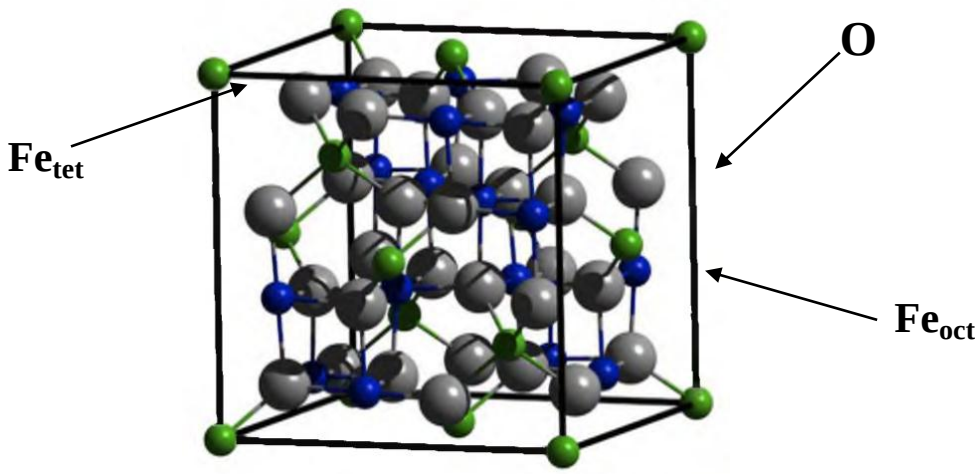

FigureI.11: *Crystallographic unit cell of (Fe_3O_4) with oxygen (grey), Fe_{oct} (blue) and Fe_{tet} ions (green)* [90].

Magnetite's Curie temperature is observed at 850 K.Below the Curie temperature, magnetic moments on tetrahedral sites, occupied by ferric species, are Ferro

magnetically aligned while magnetic moments on octahedral sites, As temperatures increase to the Curie temperature, thermal fluctuations destroy the ferromagnetic alignment of magnetic moments on tetrahedral sites; hence, ferrimagnetic strength is diminished [97]. Fig.I.11 presents of crystallographic unit cell of (Fe_3O_4).

I.3.3.6. FeO (Wüstite):

Wüstite, Fe_xO is a nonstoichiometric phase of iron divalent iron with a known stability range from x = 0.83 to 0.96 above 560°C [98]. Nearly stoichiometric samples of FeO were found to arrange the Fe and O atoms monoclinic lattice with space group *C2/m*. Atpressures of >75 GPa, a new monoclinic modification of FeO has been observed (spacegroup $P2_1/m$). The high pressure structure is closely related to that of cubic sodium chlorideas adistortion of the lattice [96].The mineralogical form of this compound is often along withdeposits of hematite, maghemite and hydrated iron oxides [98]. Natural wüstite has a brown togray appearance. Prior to structural investigations of iron oxides at the nanoscale, wüstite was typically prepared by heating iron and magnetite in sealed vessels and was known to bestable only above 560-570°C. Below this temperature, it decomposes via a two-step mechanism into α-Fe and magnetite, Fe_3O_4. Because wüstite is nonstoichiometric, Fe_xO is expected to have many defects with an ordered distribution of iron vacancies. Fe_xO can be oxidized to magnetite and finally to maghemite, γ-Fe_2O_3. All three compounds are based on an approximately face-centered cubic structure of oxygen. The transformation between the three different phases is thought to be determined by the diffusion of Fe^{2+} and Fe^{3+} ionswi thin the oxygen sub lattice and electron transfer between iron ions of different valence. The wealth of the system is enriched by the occurrence of nonstoichiometry in all three phases[96, 98].

I.3.4. Magnetic properties of iron oxides:

A magnetic material is characterized by the existence of local magnetic moments whose sum in a given direction provides what is called the magnetization of the material.

Saturation magnetization is a static magnetic characteristic. It is a parameter that depends in particular on the composition of the magnetic material and its structure. The study of the magnetism of iron oxides is fundamental, in view of the

many fields of application concerned such as magnetic recording, ferrofluidity, … [99,100].

I.3.4.1. Magnetic properties of magnetite:

Magnetite (Fe_3O_4) is the typical example of ferrimagnetic compound with very strong spontaneous magnetization. Having a cubic structure of the spinel type, its structure gives it directions of easy magnetization in the diagonals [111] with a Curie temperature of 575-585 °C and a saturation magnetization of 90-92 $A.m^2/kg$ at the ambient temperature.

I.3.4.2. Magnetic Properties of maghemite:

Due to its crystallographic resemblance to magnetite, maghemite is characterized in principle by a saturation magnetization of 70-80 $A.m^2/kg$ and a Curie temperature of 600°C. Below a temperature of about 120 K, Fe_3O_4 undergoes a first order phase transition which results in a modification of several properties among them the magnetic properties.

I.3.4.3. Magnetic properties of hematite:

Hematite is an antiferromagnetic material characterized by a Curie temperature of 675°C and by a saturation magnetization of 0.4Am2/kg, i.e. ~0.5% of the magnetization of magnetite. In addition to its Curie temperature, hematite has a transition at temperature ~ -13°C called the Morin transition from which the magnetization axis changes orientation. Below this temperature, the material gains its antiferromagnetic behavior while above the Morin temperature, the material exhibits low ferromagnetism behavior [101].

Table. I.2: Summary of the magnetic properties of Compounds of the iron-oxygen system [102].

Phase	Magnetism	Transition temperature	Magnetization at saturation at 298 K
$\alpha - Fe$	Ferromagnetic	T Curia =1041K	1710 u e m /cm³
$\gamma - Fe$	Ant ferromagnetic	T Neel = 67 K	-
FeO	Ant ferromagnetic	T Neel = 198 K	-
Fe_3O_4	Ferromagnetic	T Curia = 850 K	480 u e m /cm³
$\gamma - Fe_2O_3$	Ferromagnetic	T Curia = 875 K	440 u e m /cm³
$\alpha - Fe_2O_3$	Ant ferromagnetic Ferromagnetic	T Morin = 260 K T Neel = 955 K	3 u e m /cm³

Table.I.2 below summarizes the different magnetic properties of the phases of the iron-oxygen system in comparison with the phases of pure iron.

I.3.5. Electrical and optical properties of iron oxides:

Materials have two energy bands:

- The VB valence band, which corresponds to an energy band completely filled with valence electrons that are not involved in conducting electricity.
- The conduction band CB, which is an empty band and is defined as the first energy level above the valence band where the excited electrons arrive.

The average energy that separates VB and CB is called band gap energy.

Electrical conductivity is the ability of a material to transfer an electron from VB to CB, allowing the passage of electric current.

There are two types of materials depending on their load carrying capacity at 0 K: conductors and insulators. Conductors allow the passage of electric current. In their case, the two domains of energies overlap. Insulators do not allow the passage of electric current. Their band gap energy ranges from 3.5 to 6 V [103].

Another classification characterizes insulators which allow the passage of electric current once the temperature has risen and thus behave like conductors; They are semiconductors. The difference between semiconductor and insulator is due to the band gap width; It is lower for semiconductors than insulators [104].

The optical properties of semiconductors, in the visible, ultraviolet or infrared range, are closely related to the band gap energy. To optically excite the semiconductor, it is exposed to light radiation with a photon energy greater than the band gap energy, which leads to the occurrence of incident photon absorption phenomenon. Note that wavelength is inversely proportional to energy; Thus, the corresponding wavelength absorption limit is the inverse of the energy limit

Hematite, magnetite, magnetite and wüstite are semiconductors. They have band gap energy of 2.2, 2.03, 2.71 and 2.4eV, respectively. Hematite and magnetite are absorbed in the visible range [105–106].

I.4. The photo catalyzes:

I.4.1. Principe of photo catalysis:

Photo catalysis is a complex process that has been the subject of numerous research studies. Photo catalytic degradation is the result of a catalytic reaction, i.e. a

reaction between a gas and a solid (or a liquid and a solid) via adsorbed species. Whatever the catalyst used, there are always several stages which are [107] :

- Diffusion of reactants towards the catalytic surface through the boundary layer (external transport).
- Diffusion in the pores of the catalyst (internal transport).
- Adsorption of the reagent followed by the chemical reaction.
- Desorption of reaction products.

The semiconductor-based photo catalysis process, used for the purification of air and water, was mainly developed around titanium dioxide thanks to the considerable advantages of this compound [107].

- it is stable, inexpensive, non-toxic.
- it is the most effective photo catalyst.
- it promotes the photo degradation of a wide range of indoor pollutants at room temperature.
- the use of additives is not necessary.

As for any process including reactions in heterogeneous phase, the photo catalytic process can be divided into five stages:

- Transfer of molecules from the liquid (or gaseous) phase to the surface through the boundary layer.
- Adsorption of reactive molecules on the surface of the catalyst.
- Reaction of the adsorbed molecule.
- Desorption of products.
- Transfert des produits de la couche limite vers la solution.

Several parameters can affect photo catalytic processes such as solution pH, adsorbent concentration, dye concentration, ionic strength of solution, temperature, properties of dye structure, size of adsorbed particles , gap energy, electron recombination/hole pair life , adsorbents writes , light source and light show time.

The photo catalytic process is based on the excitation of the semiconductor (TiO2; Fe2O3, ZnO, etc.) by light radiation with a wavelength of less than 385 nm, corresponding to an energy greater than or equal to the width of the forbidden band. Its

principle consists in the promotion of an electron from the valence band (BV) to the conduction band (BC) after the irradiation of a semiconductor catalyst material (SC) with photons of higher energy. or equal to its energy gap. This results in the creation of photo-holes (h+) in the valence band (Fig.I.12). The formation of electron/hole pairs (e/h+) on the surface of the semiconductor is at the origin of its photo-catalytic activity. Indeed, as illustrated by the following reactions (a) to (d), the photoelectrons (e) and the photo holes (h+) can either recombine by generating heat (reaction b) or remain separated to get involved in electron transfer reactions with the species in solution, in other words the oxidation of an electron donor (D) (reducer) (reaction c) or reduction of an electron acceptor (A) (oxidant) (reaction d) [107].

Absorption of radiation	$SC + h\nu \rightarrow e^- + h^+$	(a)
Recombination	$e^- + h^+ \rightarrow$ heat	(b)
Oxidation	$D + h^+ \rightarrow D^*$	(c)
Reduction	$A + e^- \rightarrow A^{*-}$	(d)

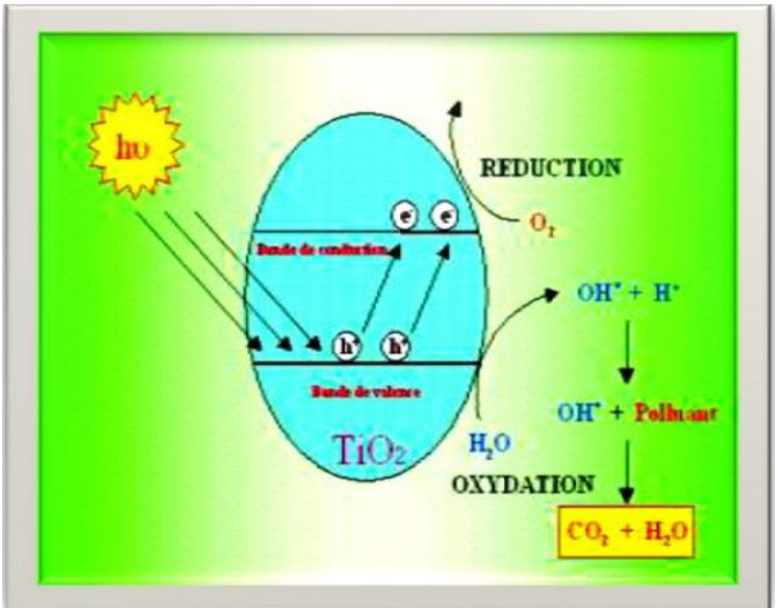

Figure I.12 Mechanism of the photo catalytic process [110]

I.4.2. Photocatalytic degradation of pollutants using iron oxide:

The use of a combination of different physico-chemical techniques is therefore essential to treat polluted water. Among these specific techniques, advanced PDO

oxidation processes have emerged over the past twenty years without their industrial application being very significant. Among the PDOs we find sonolysis, radiolysis , H2O2/ Fe2+, H2O2/ Fe2+/hν, photo catalysis appears to be one of the simplest PDO methods, capable of producing active species, to lead to the mineralization of organic compounds [110].

Among iron oxides, ferric oxide is very abundant in the earth's crust. Ferric oxide Fe_2O_3 has several phases: α-Fe_2O_3, β-Fe_2O_3, γ-$Fe2O_3$. The first structure is chemically stable in aqueous solution, it is preferred for photo-catalytic applications [111]. This oxide has semiconductor properties and many applications. Aroutiouniam et al [112]. reported only for applications.

Iron oxides have very likable qualities, they show a range of unique and attractive colors. And stable as red hematite to brown and black magnetite(29d). The adsorption capacity of iron oxide arises from the interference of hydroxyl groups during the dissolution of pollutants. Surface hydroxyl groups, with amphoteric properties, are the practical groups of iron oxide surfaces and are chemically reactive entities that act as active sites upon adsorption. The hydroxyl groups may be single, double and triple corresponding with iron atoms having a disordered interaction [110].

Several works have studied photo-catalytic adsorption of dyes on nano-materials, and reported highly efficient thermal and photo catalytic activities of nano-materials. The photo-catalysis of adsorption of methylene blue and methyl orange on iron oxide fixed in single-walled carbon nanotubes by UV irradiation was studied. They reported that the studied adsorbents showed effective photo-catalytic activity 68. The photo-catalysis of the adsorption of dye Basic Red 46 on ZnO NPs under solar irradiation was studied. They report that ZnO NPs exhibit high photo-catalytic activity. Furthermore, Kumar et al 70. He studied the photolysis of malachite green under sunlight in the presence of green magnetite synthesized using Calliandra haematocephala leaf extract. They reported that the presence of those magnetite NPs increased the photolysis of the dye [113].

The positive holes oxidize the adsorbed H_2O molecules and generate hydroxyl radicals (OH•). Whereas, the excited electrons reduce O_2 absorbed in CB and produce hydroxyl radicals (OH•). OH radicals attack these organic groups of pollutants and undergo various reactions to convert the organic pollutants into harmless forms or decay them completely decomposes them into CO_2 and H_2O [110].

I.4.3. Advantages of photo catalysis:

Photo catalysis has several advantages among which we can mention:

- ✓ It is a destructive and non-selective technology.
- ✓ Total mineralization possible: formation of H_2O and CO_2 and other species.
- ✓ It operates at ambient temperature and pressure.
- ✓ Catalyst used non-toxic, active in different physical forms, inexpensive.
- ✓ It is effective for low concentrations of pollutants.
- ✓ It requires low energy consumption.
- ✓

I.5. Conclusion:

In this chapter, various methods of green synthesis of nanoparticles are discussed , General information about iron oxides and their properties has been clarified in various aspects. Iron oxides consist of Fe, O and / or OH, and they differ in composition, in iron valence and in crystal structure . Principle of photo catalysis and photo-catalytic degradation of pollutants using iron oxide has been presented.

References

[1] Hulkoti, Nasreen I., and T. C. Taranath. "Biosynthesis of nanoparticles using microbes—a review." Colloids and surfaces B: Biointerfaces 121 (2014): 474-483.

[2] Al-saidi, Muthana H., and Wurood Hasan Hadi. "The green method of preparing nanoparticles and its applications in the field of biology."

[3] Ribeiro, Jomar José Knaip, et al. "Green Synthesis of Nanomaterials: most cited papers and research trends." Research, Society and Development 9.1 (2020): e54911593-e54911593.

[4] Dahoumane, Si Amar, et al. "Improvement of kinetics, yield, and colloidal stability of biogenic gold nanoparticles using living cells of Euglena gracilis microalga." Journal of Nanoparticle Research 18 (2016): 1-12.

[5] El-Rafie, H. M., MHl El-Rafie, and M. K. Zahran. "Green synthesis of silver nanoparticles using polysaccharides extracted from marine macro algae." Carbohydrate polymers 96.2 (2013): 403-410.

[6] Kumar, Paskalis Sahaya Murphin, Arul Prakash Francis, and Thiyagarajan Devasena. "Biosynthesized and chemically synthesized titania nanoparticles: comparative analysis of antibacterial activity." J. Environ. Nanotechnol 3.3 (2014): 73-81.

[7] Wang, Luyan, et al. "Synthesis of gold nano-and microplates in hexagonal liquid crystals." The Journal of Physical Chemistry B 109.8 (2005): 3189-3194.

[8] You, Hongjun, et al. "Synthesis of colloidal metal and metal alloy nanoparticles for electrochemical energy applications." Chemical Society Reviews 42.7 (2013): 2880-2904.

[9] Singh, Priyanka, et al. "Biological synthesis of nanoparticles from plants and microorganisms." Trends in biotechnology 34.7 (2016): 588-599.

[10] Das, Ratul Kumar, et al. "Biological synthesis of metallic nanoparticles: plants, animals and microbial aspects." Nanotechnology for Environmental Engineering 2 (2017): 1-21.

[11] Irshad, S., et al. "Biosynthesis of ZnO nanoparticles using Ocimum basilicum

and determination of its antimicrobial activity." J. Anim. Plant Sci 30.2020 (2020): 10-36899.

[12] Berra, D., et al. "Green synthesis of copper oxide nanoparticles by pheonixdactylifera l leaves extract." Digest Journal of Nanomaterials and Biostructures 13.4 (2018): 1231-1238.

[13] Stozhko, Natalia Yu, et al. "The effect of the antioxidant activity of plant extracts on the properties of gold nanoparticles." Nanomaterials 9.12 (2019): 1655.

[14] Ayed, Rihab Ben, Mejda Ajili, and Najoua Kamoun Turki. "Physical properties and Rietveld analysis of Fe2O3 thin films prepared by spray pyrolysis: effect of precursor concentration." Physica B: Condensed Matter 563 (2019): 30-35.

[15] Qin, Xiao, et al. "Flame synthesis of Y2O3: Eu nanophosphors using ethanol as precursor solvents." Journal of materials research 20.11 (2005): 2960-2968.

[16] Limaye, Amit U., and Joseph J. Helble. "Effect of precursor and solvent on morphology of zirconia nanoparticles produced by combustion aerosol synthesis." Journal of the American Ceramic Society 86.2 (2003): 273-278.

[17] Karade, V. C., et al. "Effect of reaction time on structural and magnetic properties of green-synthesized magnetic nanoparticles." Journal of Physics and Chemistry of Solids 120 (2018): 161-166.

[18] Samy, Ahmed, Amal E. El-Sherbiny, and A. A. Menazea. "Green synthesis of high impact zinc oxide nanoparticles."Egyptian Journal of Chemistry 62.The First International Conference on Molecular Modeling and Spectroscopy 19-22 February, 2019 (2019): 29-37.

[19] Zamri, Muhammad SyahinFirdaus Aziz, and NorzahirSapawe. "Effect of pH on phenol degradation using green synthesized titanium dioxide nanoparticles." Materials Today: Proceedings 19 (2019): 1321-1326.

[20] Jafari, A., et al. "Effect of annealing temperature on magnetic phase transition in Fe3O4 nanoparticles." Journal of Magnetism and Magnetic Materials 379 (2015): 305-312

[21] Laid, Tedjani Mohammed, et al. "Optimizing the biosynthesis parameters of iron oxide nanoparticles using central composite design." Journal of Molecular Structure 1229 (2021): 129497.

[22] Bisen, P., et al. "VAM colonization in tree species planted in Cu, Al, and coal mines of Madhya Pradesh with special reference to glomus mosseae." Mycorrhiza News 8.1 (1996): 9-11.

[23] Khare, Punam, and P. S. Bisen. "Mitigating Effect of physico-chemical factors ON Ni2+ Hg2+ and Cu2+ toxicity in cylindrospermum Iu 942." Environmental technology 12.4 (1991): 297-301.

[24] Sharma, S. K., et al. "Influence of sodium ion on heavy metal-induced inhibition of light-regulatd proton efflux and active carbon uptake in the cyanobacterium Anabaena flos-aquae." World Journal of Microbiology and Biotechnology 17 (2001): 707-711.

[25] Sharma, S. K., and P. S. Bisen. "Hg 2+ and Cd 2+ induced inhibition of light induced proton efflux in the cyanobacterium Anabaena flos-aquae." Biometals 5 (1992): 163-167.

[26] Singh, D. P., S. K. Sharma, and P. S. Bisen. "Differential action of Hg 2+ and Cd 2+ on the phycobilisomes and chlorophyll a fluorescence, and photosystem II dependent electron transport in the cyanobacterium Anabaena flos-aquae." Biometals 6 (1993): 125-132.

[27] Deplanche, Kevin, et al. "Involvement of hydrogenases in the formation of highly catalytic Pd (0) nanoparticles by bioreduction of Pd (II) using Escherichia coli mutant strains." Microbiology 156.9 (2010): 2630-2640.

[28] Yong, Ping, et al. "Biloaccumulation of palladium by Desulfovibrio desulfuricans." Journal of chemical technology and biotechnology 77.5 (2002): 593-601.

[29] Iravani, Siavash. "Bacteria in nanoparticle synthesis: current status and future prospects." International scholarly research notices 2014 (2014).

[30] Gericke, Mariekie, and Anthony Pinches. "Microbial production of gold nanoparticles." Gold bulletin 39.1 (2006): 22-28.

[31] Sunkar S, Nachiyar CV. Biogenesis of antibacterial silver nanoparticles using the endophytic bacterium Bacillus cereus isolated from Garciniaxanthochymus. AsianPac J Trop Biomed. 2012;2:953–9.

[32] Chen, Yen-Lin, et al. "Augmented biosynthesis of cadmium sulfide

nanoparticles by genetically engineered Escherichia coli." Biotechnology progress 25.5 (2009): 1260-1266.

[33] Mohanpuria, Prashant, Nisha K. Rana, and Sudesh Kumar Yadav. "Biosynthesis of nanoparticles: technological concepts and future applications." Journal of nanoparticle research 10 (2008): 507-517.

[34] Narayanan, Kannan Badri, and Natarajan Sakthivel. "Synthesis and characterization of nano-gold composite using Cylindrocladium floridanum and its heterogeneous catalysis in the degradation of 4-nitrophenol." Journal of hazardous materials 189.1-2 (2011): 519-525..

[35] Mukherjee, Priyabrata, et al. "Fungus-mediated synthesis of silver nanoparticles and their immobilization in the mycelial matrix: a novel biological approach to nanoparticle synthesis." Nano letters 1.10 (2001): 515-519.

[36] Senapati, Satyajyoti, et al. "Extracellular biosynthesis of bimetallic Au–Ag alloy nanoparticles." Small 1.5 (2005): 517-520.

[37] Raliya, Ramesh, and J. C. Tarafdar. "Biosynthesis and characterization of zinc, magnesium and titanium nanoparticles: an eco-friendly approach." International Nano Letters 4 (2014): 1-10.

[38] Raliya, Ramesh, Pratim Biswas, and J. C. Tarafdar. "TiO2 nanoparticle biosynthesis and its physiological effect on mung bean (Vigna radiata L.)." Biotechnology Reports 5 (2015): 22-26.

[39] Yurkov, Andrey M., Martin Kemler, and Dominik Begerow. "Species accumulation curves and incidence-based species richness estimators to appraise the diversity of cultivable yeasts from beech forest soils." PLoS One 6.8 (2011): e23671.

[40] Bhattacharya, Debaditya, and Rajinder K. Gupta. "Nanotechnology and potential of microorganisms." Critical reviews in biotechnology 25.4 (2005): 199-204.

[41] Mandal, Deendayal, et al. "The use of microorganisms for the formation of metal nanoparticles and their application." Applied microbiology and biotechnology 69 (2006): 485-492.

[42] Mourato, Ana, et al. "Biosynthesis of crystalline silver and gold nanoparticles by extremophilic yeasts." Bioinorganic chemistry and applications 2011 (2011).

[43] Attia, TM Salem, and N. I. Elsheery. "Nanomaterials: scope, applications, and

challenges in agriculture and soil reclamation." Sustainable Agriculture Reviews 41: Nanotechnology for Plant Growth and Development (2020): 1-39.

[44] Song, Jae Yong, and Beom Soo Kim. "Rapid biological synthesis of silver nanoparticles using plant leaf extracts." Bioprocess and biosystems engineering 32 (2009): 79-84.

[45] Keat, Cheah Liang, et al. "Biosynthesis of nanoparticles and silver nanoparticles." Bioresources and Bioprocessing 2.1 (2015): 1-11.

[46] Makarov, V. V., et al. "“Green” nanotechnologies: synthesis of metal nanoparticles using plants." Acta Naturae (англоязычная версия) 6.1 (20) (2014): 35-44.

[47] Rajasekhar.C, Gan.G.R, (2018) « Green Synthesis of Metal Nanoparticles and its Reaction Mechanisms » Scrivener Publishing LLC , p 114.

[48] Barman, Kailash, Devasish Chowdhury, and Pranjal K. Baruah. "Bio-synthesized silver nanoparticles using Zingiber officinale rhizome extract as efficient catalyst for the degradation of environmental pollutants." Inorganic and nano-metal chemistry 50.2 (2020): 57-65.

[49] Mohseni, Maedeh Sadat, et al. "Green synthesis of Ag nanoparticles from pomegranate seeds extract and synthesis of Ag-Starch nanocomposite and characterization of mechanical properties of the films." Biocatalysis and Agricultural Biotechnology 25 (2020): 101569.

[50] Pansambal, Shreyas, et al. "Green synthesis of CuO nanoparticles using Ziziphus mauritiana L. extract and its characterizations." Int. J. Sci. Res. in Sci. and Tech 3 (2017): 1388-1392.

[51] Irshad, S., et al. "Biosynthesis of ZnO nanoparticles using Ocimum basilicum and determination of its antimicrobial activity." J. Anim. Plant Sci 30.2020 (2020): 10-36899.

[52] Abdullah, F. H., NHH Abu Bakar, and M. Abu Bakar. "Low temperature biosynthesis of crystalline zinc oxide nanoparticles from Musa acuminata peel extract for visible-light degradation of methylene blue." Optik 206 (2020): 164279.

[53] Chokkalingam, Mohan, et al. "Facile synthesis of Au and Ag nanoparticles using fruit extract of Lycium chinense and their anticancer activity." Journal of Drug

Delivery Science and Technology 49 (2019): 308-315.

[54] Crooks, Richard M., et al. "Dendrimer-encapsulated metal nanoparticles: synthesis, characterization, and applications to catalysis." Accounts of chemical research 34.3 (2001): 181-190.

[55] Ealia, S. Anu Mary, and M. P. Saravanakumar. "A review on the classification, characterisation, synthesis of nanoparticles and their application." IOP conference series: materials science and engineering. Vol. 263. No. 3. IOP Publishing, 2017.

[56] Krishna, R. Nivesh, R. Gayathri, and Vishnu Priya. "Nanoparticles and their applications-a review." Journal of Pharmaceutical Sciences and Research 9.1 (2017): 24.

[57] Wang, Zheng, Jing Ruan, and Daxiang Cui. "Advances and prospect of nanotechnology in stem cells." Nanoscale research letters 4 (2009): 593-605.

[58] Munier, Pierre. Le palmier-dattier. Vol. 24. Maisonneuve & Larose, 1973.

[59] Freha, Gourchala. Caractérisation physicochimique, phytochimique et biochimique de cinq variétés de dattes d'Algérie, Phoenix dactylifera L.(Deglet noor, Ghars, H'mira, Tamesrit et Tinissine). Effets de leur ingestion sur certains paramètres biologiques. Diss. Université Badji Mokhtar, 2015.

[60] Mazoyer, M. "Larousse agricole, le monde agricole au XXIème siècle." Mathilde (2002).

[61] Uhl, Natalie W., and John Dransfield. "Genera Palmarum: a classification of palms based on the work of Harold E. Moore, Jr." (1987).

[62] Barrow, Sasha C. "A monograph of phoenix L.(palmae: Coryphoideae)." Kew bulletin (1998): 513-575.

[63] Djerbi, M. "Précis de phoeniciculture." Ed. FAO, Rome 24.4 (1994).

[64] Saaidi, Mohamed, et al. "La sélection du Palmier-dattier (Phoenix dactylifera L.) pour la résistance au Bayoud." Fruits 36.4 (1981): 241-249.

[65] Peyron, Gilles. "Cultiver le palmier-dattier." Cultiver le palmier-dattier (2000): 1-112.

[66] CIRAD et GRET, Ministère des affaires étrangères. Centre de coopération internationale en recherche agronomique pour le développement (CIRAD). Groupe de

recherche et d'étranges technologiques (GRET).Ed. Jouve, bd de Sébastopol. France (2002): 986- 990.

[67] Al-Bakr, A. "The date palm, a review of its past and present status and its culture, industry and trade." Iraq: Alaïn Press, 1405p.(en arabe) (1972).

[68] Guignard, J. "Botanique systématique moléculaire, 2ème édition Lavoisier." Paris, p122 (2001).

[69] Ben-Abbes, Farah. Etude de quelques propriétés chimiques et biologiques d'extraits de dattes phoenix dactylifera L. Diss. 2018.

[70] TourerN, G. "Le palmier dattier culture et production." Al awamia (1967).

[71] BENGAG, Amine. Caractérisation phytochimique et activité antioxydante de quelques cultivars de Phoenix dactylifera L. Diss. Université d'Oran1-Ahmed Ben Bella, 2009.

[72] Chehma, A., and H. F. Longo. "Valorisation des sous-produits du palmier dattier en vue de leur utilisation en alimentation du bétail." Rev. Energ. Ren.: Production et Valorisation–Biomasse (2001): 59-64.

[73] Daas Amiour, Saliha. Etude quantitative des composes phénoliques des extraits de trois variétés de dattes (Phoenix dactylifera L.) Et évaluation in vitro de leur activité biologique. Diss. Université de Batna 2, 2009.

[74] Bensaada, K. "Etude du développement et architecture racinaire de plantules de palmier dattier sous stress salin." Mémoire de magister, Université d 'Oran1 Ahmed Ben Bella (2015).

[75] Truffault, Laurianne. Synthèse et caractérisation de nanoparticules à base d'oxydes de cérium et de fer pour la filtration des UV dans les produits solaires. Diss. Université d'Orléans; University of Wollongong (Wollongong, Australie), 2010.

[76] M.J.A. López, Claudia Jeannette Sarita Aparicio Ordoñez, Doctoral thesis, Placky university, Olomouc ,2006.

[77] Pepperhoff, Werner, and Mehmet Acet. Constitution and Magnetism of Iron and its Alloys. Springer Science & Business Media, 2001..

[78] Rahman, Mohammed M., et al. "Iron oxide nanoparticles." Nanomaterials 3 (2011): 43-67.

[79] Wu, Wei, et al. "Recent progress on magnetic iron oxide nanoparticles:

synthesis, surface functional strategies and biomedical applications." Science and technology of advanced materials 16.2 (2015): 023501.

[80] He, Shiying, et al. "Different responses of soil microbial metabolic activity to silver and iron oxide nanoparticles." Chemosphere 147 (2016): 195-202.

[81] He, Shiying, et al. "The impact of iron oxide magnetic nanoparticles on the soil bacterial community." Journal of Soils and Sediments 11 (2011): 1408-1417.

[82] Ubale, A. U., and M. R. Belkhedkar. "Size dependent physical properties of nanostructured α-Fe2O3 thin films grown by successive ionic layer adsorption and reaction method for antibacterial application." Journal of Materials Science & Technology 31.1 (2015): 1-9.

[83] Cheng, Yicheng, et al. "Antibacterial activity and biological performance of a novel antibacterial coating containing a halogenated furanone compound loaded poly (L-lactic acid) nanoparticles on microarc-oxidized titanium." International journal of nanomedicine 10 (2015): 727.

[84] Popa, C. L., et al. "Inhibitory effect evaluation of glycerol-iron oxide thin films on methicillin-resistant Ataphylococcus aureus." Journal of Nanomaterials 2015 (2015): 5-5.

[85] Schwarz, Sebastian, et al. "Polyelectrolyte coating of iron oxide nanoparticles for MRI-based cell tracking." Nanomedicine: Nanotechnology, Biology and Medicine 8.5 (2012): 682-691.

[86] Kim, Do Kyung, et al. "Protective coating of superparamagnetic iron oxide nanoparticles." Chemistry of Materials 15.8 (2003): 1617-1627.

[87] Zelmanov, G., and R. Semiat. "Iron (Fe+ 3) oxide/hydroxide nanoparticles-based agglomerates suspension as adsorbent for chromium (Cr+ 6) removal from water and recovery." Separation and purification technology 80.2 (2011): 330-337.

[88] Al-Hobaib, A. S., Kh M. AL-Sheetan, and L. El Mir. "Effect of iron oxide nanoparticles on the performance of polyamide membrane for ground water purification." Materials Science in Semiconductor Processing 42 (2016): 107-110.

[89] Kumar ,P., Synthesis and Characterization of Nanostructured Iron Oxide Thin Films: structural, magnetic and optical properties, Doctoral thesis, Yaypee university, 2014.

[90] Lakhal, Rihab. Nouveau procédé d'élaboration de micro et nanoparticules d'oxyde de fer en voie sèche: Caractérisation, étude du procédé et proposition d'un mécanisme rationnel. Diss. 2016.

[91] Cornell, Rochelle M., and Udo Schwertmann. The iron oxides: structure, properties, reactions, occurrences, and uses. Vol. 664. Weinheim: Wiley-vch, 2003.

[92] Drbohlavova, Jana, et al. "Preparation and properties of various magnetic nanoparticles." Sensors 9.4 (2009): 2352-2362.

[93] Ayachi, A.A. Synthèse des nanoparticules d'oxydes métalliques pour des applications photocatalytiques solaires, Doctoral thesis, Constantine university, 2015 .

[94] Lee, Seungyeol, and Huifang Xu. "The role of ε-Fe2O3 nano-mineral and domains in enhancing magnetic coercivity: Implications for the natural remanent magnetization." Minerals 8.3 (2018): 97.

[95] Tucek, Jiri, et al. "ε-Fe2O3: An advanced nanomaterial exhibiting giant coercive field, millimeter-wave ferromagnetic resonance, and magnetoelectric coupling." Chemistry of Materials 22.24 (2010): 6483-6505.

[96] Gonzalez, Juan Pablo. SYNTHESIS AND CHARACTERIZATION OF IRON OXIDE THIN FILMS FOR USE IN ELECTRICAL DEVICES. Diss. San Diego State University, 2013.

[97] Blaney, Lee. "Magnetite (Fe3O4): Properties, synthesis, and applications." (2007).

[98] Hazen, Robert M., and Raymond Jeanloz. "Wüstite (Fe1-x O): A review of its defect structure and physical properties." Reviews of Geophysics 22.1 (1984): 37-46.

[99] Uddin, Md Azhar, et al. "Catalytic decomposition of biomass tars with iron oxide catalysts." Fuel 87.4-5 (2008): 451-459.

[100] Jurgons, R., et al. "Drug loaded magnetic nanoparticles for cancer therapy." Journal of Physics: Condensed Matter 18.38 (2006): S2893.

[101] Williamson, D. L., et al. "Morin transition of shock-modified hematite." Physical Review B 34.3 (1986): 1899.

[102] Goutayer, Mathieu. Nano-émulsions pour la vectorisation d'agents thérapeutiques ou diagnostiques: étude de la biodistribution par imagerie de fluorescence in vivo. Diss. Université Pierre et Marie Curie-Paris VI, 2008.

[103] Gerl, Maurice, and Jean-Paul Issi. Physique des matériaux. Vol. 8. PPUR presses polytechniques, 1997.

[104] Neamen, D. "Semiconductor physics and devices (pp. 474–483)." (2003).

[105] Cornell, Rochelle M., and Udo Schwertmann. The iron oxides: structure, properties, reactions, occurrences, and uses. Vol. 664. Weinheim: Wiley-vch, 2003.

[106] Ahmouda, Kaouthar, et al. "Plant extract FRAP effect on cation vacancies formation in greenly synthesized wüstite (FexO) nanoparticles: A new contribution." Sustainable Chemistry and Pharmacy 25 (2022): 100563.

[107] Christoffel, Erhard G., and Zoltán Paál. Laboratory studies of heterogeneous catalytic processes. Elsevier, 1989.

[108] Zhao, Juan, and Xudong Yang. "Photocatalytic oxidation for indoor air purification: a literature review." Building and environment 38.5 (2003): 645-654.

[109] Robertson, Peter KJ. "Semiconductor photocatalysis: an environmentally acceptable alternative production technique and effluent treatment process." Journal of cleaner production 4.3-4 (1996): 203-212.

[110] Bazine, Abdelmadjid, and Mohamed Salah Ferah. Elaboration par sol-gel et caracterisation d'oxyde metallique (type: α-fe2o3) aux propries photocatalytiques. Diss. Université Frères Mentouri-Constantine 1, 2017.

[111] Gondal, M. A., et al. "Production of hydrogen and oxygen by water splitting using laser induced photo-catalysis over Fe2O3." Applied Catalysis A: General 268.1-2 (2004): 159-167.

[112] Aroutiounian, V. M., et al. "Photoelectrochemistry of tin-doped iron oxide electrodes." Solar Energy 81.11 (2007): 1369-1376.

[113] Masudi, Ahmad, et al. "Magnetite-based catalysts for wastewater treatment." Environmental Science and Pollution Research 27 (2020): 4664-4682.

CHAPTER II

Synthesis and Characterization Techniques

II.1. Introduction

This chapter is devoted to experimental materials, methods and techniques (XRD, SEM, FTIR, UV-Visible) used to describe the structural and optical properties of iron oxide nanoparticles.

II.2. Materials and methods:

This work includes the study of green synthesis and characterization of metallic nanoparticles by Phoenix Dactylifera L leaf extract and their biological activities. This work work was carried out at the level of the Saharan Resources Development and Technology Laboratory (VTRS) of the Echahide Hamma Lakhdar University of El Oued.

II.2.1. Plant matter:

In the context of green chemistry for the synthesis of iron oxides nanoparticles, we have selected the leaves of Phoenix Dactylifera L as a reducing agent. This choice is based on the studies carried out on this plant within the VTRS laboratory. They confirmed the presence of several phytochemical compositions, including: alkaloids, polyphenols (flavonoids, tannins) and saponins.

II.2.2. Methodology:

II.2.2.1. Preparation of samples:

Leaves of phoenix Dactylifera L were collected from Ghars cultivar from El Oued, Algeria. The samples are cleaned and then dried at room temperature and protected from sunlight in order to preserve the integrity of their chemical composition as much as possible.

- **Extraction of phenolic compounds:**

For the separation of natural materials from the raw material with the use of solvents, if the material to be separated is solid in this case solid-liquid extraction is applied. The principle of this method is that the solvent must cross the solid-liquid interface barrier, dissolve the active component inside the solid and drive it outside.

In our study, for the extraction of phenolic compounds using the technique of extraction by maceration.

- **Procedure:**

50 g of leaf powder was added to 300 ml of ethanol. This preparation was stirred for 24 hours at room temperature. The extracts were filtered and stored at 4°C.

II.2.2.2. Synthesis of iron oxides nanoparticles:

Iron oxides nanoparticles were synthesized by reduction of iron chlorine by phenolic compounds from leaf extract.

40 ml of the extract were mixed with 80 ml of mineral aqueous solution. The reaction is carried out using reflux aggregation with continuous stirring for 1 hour at 70°C. The solid product obtained by centrifugation at room temperature was rinsed several times with distilled water, then dried at 90-100°C over night.

In this work, we focused on the study of the effect of the following parameters:

- Effect the concentration of iron chlorine (0.01, 0.02, 0.03 and 0.04M).
- Effect of annealing time (0, 1, 2 and 3 hours)

II.3. Characterization techniques:

Given the nanoscale nature of the materials synthesized in this study, we will present in this part, the various investigation techniques under which a precise description of the latter will be shown.

II.3.1. Structural and morphological properties:

II.3.1.1. X-ray diffraction (XRD):

X-rays are electromagnetic radiation with a wavelength between 0.01 and 10°A. This non-destructive technique is the most useful and widespread for identifying the nature and structure of crystallized products. In addition, X-ray diffraction provides access to physical information about crystals, including their size and orientation.

➢ **Principle:**

This technique is based on the interactions of the crystalline structure of a sample with short-wavelength monochromatic radiation.

When the X-rays reach the reticular planes of the crystal lattices, either they come into contact with the electronic clouds of the atoms constituting this plane, in this case the beams of the X-rays are partially reflected by the foreground, or they do not encounter any obstacle and can continue to the second plane to be partially reflected again. These planes are separated by characteristic distances which depend on the nature of the material analyzed (reticular distances).

The interferences of the rays will be alternately constructive or destructive. The directions in which the interferences are constructive, called diffraction peaks, can be determined by Bragg's law [1].

➢ **Bragg's law:**

When a crystalline species is irradiated by X-radiation of wavelength λ under an incidence θ the radiation is diffracted if Bragg's law is verified.

$$n\,\lambda = 2\,d_{hkl}\,\sin\theta \qquad \text{(II.1)}$$

Where :n is an integer representing the order of the reflection.

λ is the wavelength of the X-rays.

d is the interreticular distance.

θ is the angle of incidence of the X-rays.

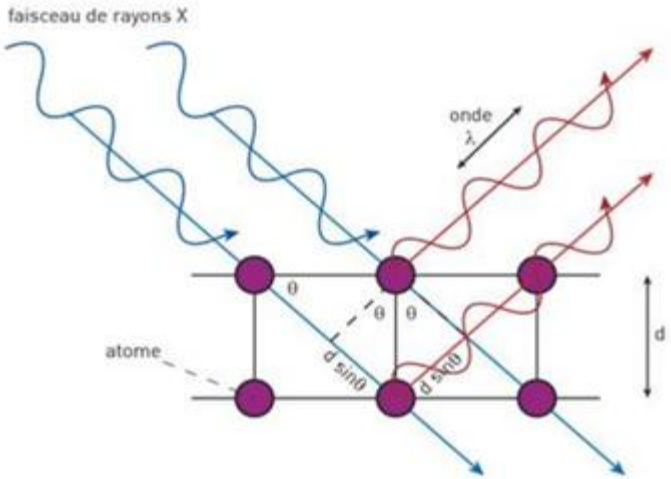

Figure II.1 : *Diagram illustrating Bragg's law* [2].

In general, the study of the diffractogram makes it possible to trace a large number of information such as the orientation of a single crystal, the structural properties and the size and shape of the samples.

- **Grain size determination:**

Although many approaches have been described for size determination using XRD, the Debye-Scherrer equation is the most commonly used for size determination [3].

$$D = 0.9\,\lambda/\beta\cos\theta \qquad \text{(II.2)}$$

Where: D is the grain size in nm.

λ is the wavelength of the X-ray beam in nm.

θ is the diffraction angle in radians.

β is the width at half height expressed in radians.

II.3.1.2. Scanning electron microscopy (SEM):

Is a technique that allows the observation of the surface morphology of a solid material. This technique therefore offers several advantages in morphological and dimensional analysis.

- **Principle:**

Scanning electron microscopy is a technique using electron-matter interactions. SEM provides images of the surface in relation to the mode of electron scattering by the sample. These images are formed mainly using surface electron emissions (secondary electrons and backscattered electrons).

The interaction between the beam of electrons with energy E_0 (primary electrons) and the sample generates low-energy electrons called "secondary electrons". The latter are then accelerated towards a detector which has the role of amplifying the electrical signal received (at each point, the intensity is converted into an electrical signal). The different particles are analyzed by different detectors which make it possible to reconstruct a three-dimensional image of the surface.

It uses, in addition, the other interactions of primary electrons with the sample: emergence of backscattered electrons, absorption of primary electrons, as well as the emission of X photons. Each of these interactions is often significant of the topography and/or the composition of the surface [4].

Also, these characteristic signals give information about the sample chemical identification and composition [5] (i.e EDX). The diagram of the scanning electron microscope is shown in Fig. II.2.

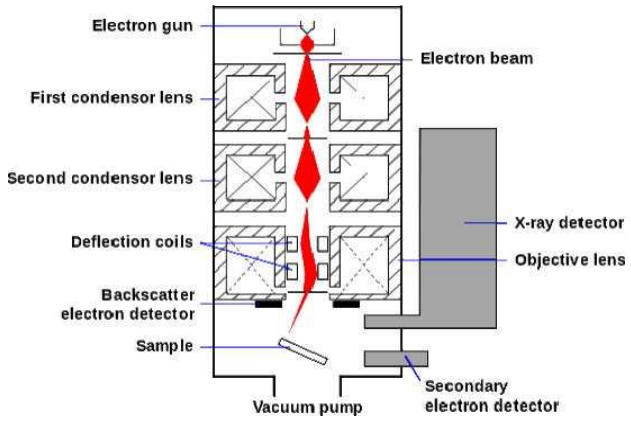

Fig. II. 2.a : *Diagram of scanning electron microscope* [6]. **Fig. II. 2.b :** *Photo of SEM apparatus.*

II.3.2. Optical properties:

II.3.2.1. UV-visible absorption spectrometer:

UV-visible absorption spectroscopy plays a very important role in studying the optical properties of nanoparticles. It is based on the study of the interaction of electromagnetic waves and matter.

- **Principle:**

UV-visible absorption spectrometry is based on the transition of valence electrons which pass from a ground state to an excited state after absorption of a photon in the UV-visible.

When the electrons encounter a light wave of a frequency corresponding to their vibrational frequencies, they absorb the energy of the light wave and acquire a vibrational movement. The vibrating electron interacts with nearby electrons and converts the vibration into heat energy. Absorption spectroscopy therefore refers to the measurement of the absorption of light by a material as a function of wavelength.

The greater the number of molecules that absorb light of a given wavelength, the greater the light absorption and the higher the peak intensity of the absorption spectrum [7].

This spectrophotometer works according to the Beer-Lambert principle which indicates that the fraction of incident radiation absorbed is proportional to the number of absorbing molecules on its path.

Mathematically, this law can be explained as:

$$\log (I_0/I) = \varepsilon c l \quad \text{(II.3)}$$

Where

I_0: Intensity of incident light.

I: Intensity of light transmitted by the sample solution.

c: sample concentration.

l: sample path length.

ε: molar absorption coefficient.

The I/I_0 ratio is known as the transmittance (T) and the logarithm of the inverse ratio

I_0/I is known as the absorbance (A).

As a result

$$-\log (I/I_0) = -\log T = \varepsilon c l$$

Where $\alpha = \varepsilon c l$

So

$$\alpha = \log (1/T) \quad \text{(II.4)}$$

The energy gap E_g can be found from the well known relation: Tauc's relation (see Fig. II.3) as follows:

$$(ahv)^2 = B(hv - Eg) \quad \text{(II.5)}$$

where

B is a constant.

(*hv*) is the photon energy.

E_g is the band gap energy of the sample.

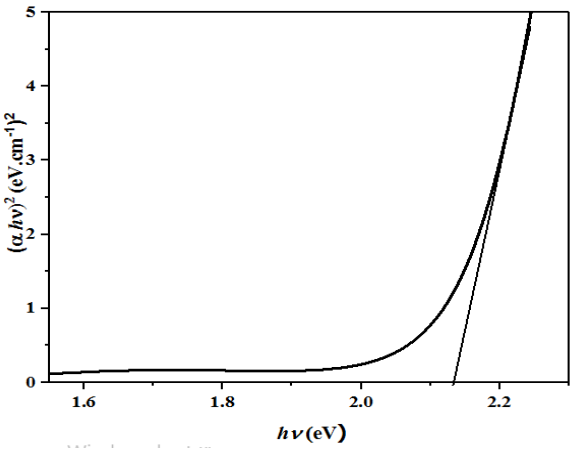

Figure II.3 : *Plot of $(\alpha hv)^2$ vs. (hv)*.

II.3.2.2. Fourier Transform Infrared Spectroscopy (FTIR):

FT-IR spectroscopy is a technique to obtain information about the different functional groups from the peak positions in the spectrum. Information on the identification and stabilization of nanoparticles can also be deduced from this analysis.

- **Principle:**

The principle of FTIR is based on the absorption of single or double beam infrared radiation by the sample to be analyzed. It allows via the detection of the characteristic vibration frequencies of the chemical bonds, to carry out the analysis of the chemical functions present in the material.

The infrared beam is directed towards the Michelson interferometer which will modulate each wavelength of the beam at a different frequency. In the latter, the incident light beam is split into two by a splitter. These two parts will be reflected on mirrors, one of which is fixed and the other mobile. When the two beams recombine, destructive or constructive interferences appear depending on the position of the mobile mirror. The modulated beam is then reflected from the two mirrors towards the sample, where absorptions occur. The beam then arrives at the detector to be transformed into an electrical signal [8].

II.4.Conclusion

Characterization is an important step in the improvement of different materials. The physical characterization of the iron oxide nanomaterial contains of structural, surface, and optical properties with employ XRD, SEM, FT-IR, and UV-vis spectrophotometry.

References

[1] Serna, Frédéric, Jean Lagneau, and Jean-Marc Carpentier. "La diffraction des rayons X: une technique puissante pour résoudre certains problèmes industriels et technologiques." Chim. Nouv (2014): 1-12..

[2] Ayachi, Ahmed Abdelhakim, and Smail Boudjadar. "Synthèse des nanoparticules d'oxydes métalliques pour des applications photocatalytiques solaires." (2017).

[3] Ghidan, Alaa Y., Tawfiq M. Al-Antary, and Akl M. Awwad. "Green synthesis of copper oxide nanoparticles using Punica granatum peels extract: Effect on green peach Aphid." Environmental Nanotechnology, Monitoring & Management 6 (2016): 95-98.

[4] PAQUETON, Henri, and Jacky RUSTE. "Microscopie électronique à balayage Principe et équipement." Techniques de l'ingénieur. Analyse et caractérisation P865v2 (2006).

[5] Goldstein, Joseph I., et al. Scanning electron microscopy and X-ray microanalysis. Springer, 2017.

[6] ABBAS, Soumaia. Détermination Spectroscopique des Grandeurs Optoélectroniques du SnO2 Dopé Elaboré par Spray Ultrasonique. Diss. Université Kasdi Merbah Ouargla, 2016.

[7] Singh, Ashok K. Engineered nanoparticles: structure, properties and mechanisms of toxicity. Academic Press, 2015:138 .

[8] Gueye, Magamou. "DOCTEUR DE L'UNIVERSITE DE LORRAINE." (2016).

CHAPTER III
Effect of Iron Chlorine Concentration on the Type of Product

III.1. Introduction:

The aim of this chapter is to study the structural and optical properties of iron oxides nanoparticles greenly synthesized by reacting the ethanolic extract of Phoenix dactylifera. L with different iron chloride ($FeCl_3$) salt concentration in aqueous solution. The effect of $FeCl_3$ salt concentration within the extract and the 500°C annealed products for one hours, will be analyzed using XRD, UV–VIS, SEM and FTIR. Also in this chapter, an EB Evans Blue preferential and adsorption enhancer on the surfaces of Fe2O3 NPs it was chosen as application.

III.2. Experimental details:

III.2.1. Preparing and extracting plant materials:

Palm leaves (Phoenix dactylifera. L) were collected from local farms in El-Oued province, Algeria. Firstly, they are washed several times with tap water and distilled water to remove dust, dirt and impurities suspended to them. The palm leaves are cut into medium pieces and dried at room temperature for 10 days, then grinded to get the palm leaves sheet powder. Extraction operation palm leaves was proceed to have leaves extract by placing 50 g of the previous powder with 300ml of ethanol in a 1000ml glass jar with continuous stirring for a full day at room temperature. Finally, this mixture is filtered and considered as liquid ethanolic leaves extract(L.E.L.E) mother sources for use.

III.2.2.Preparation of iron oxide nanoparticles:

Iron oxide NPs are synthesized by reacting 40ml of the (L.E.L.E) with four different concentrations (0.01– 0.02– 0.03– 0.04M) of $FeCl_3$ aqueous solution of 80ml for each experimentation. The mixture has obeying to continuous stirring, in a water bath system at 70°C, for one hour. Iron oxide particles formation starts when the change in the color of the mixture, from green to dark brown, appears. After that,

the blend was dried and the residual products was washed several times with distilled water and collected by centrifugation. The collected product was dried again at 90-100°C inside the drying oven. Finally, Iron oxide NPs were obtained after annealing treatment at 500°C, into a special oven, for an hour. Photos of the prepared powders for different concentrations are shown in Fig.III.1.

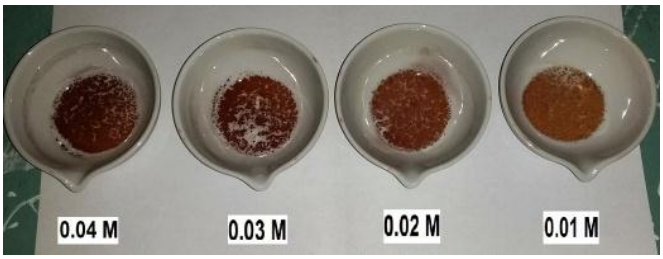

Figure III.1: *Photos of the prepared powders for different concentrations.*

III.2.3. Characterization of iron oxide nanoparticles:

The band gap energy has been estimated through the optical transmittance spectrum using (UV–VIS spectrophotometer Shimadzu, Model 1800) operating in the wavelength 200-900nm range. To find out iron oxides crystal structure XRD technique was employed using X-ray diffract meter (Rigaku Miniflex 600) apparatus with a Cu-Kα (λ = 1.5406 Å) operating in the 2θ angles of 10° to 90°range, and (30keV, 30mA) as conditions of X-ray generation. Iron oxide NPs chemical bonds were determined by their vibration in 400-4000cm^{-1}infrared spectrum which was scanned by a device (Nicolet iS5, Thermo Fisher Scientific). The surface investigation was done with scanning electron microscopic (SEM-TESCAN VEGA 3), all measurements are done at room temperature.

III.3. Results and discussion:

III.3.1. Structural properties:

Fig III.2 The XRD patterns of powders treated for 1h at 500°C are shown in Fig III.2. XRD peaks show the existence of three iron oxide essentials compounds:

- Gamma phase, maghemite (γ-Fe_2O_3) having a tetragonal crystalline structure according to JCPDS No: 00-025-1402 where peaks appear at 2θ: 30.214°, 35.683°, 57.307°, and 62.885° correspond to lattice plane of (*206*), (*119*), (*1115*) and (*4012*), respectively;
- Alpha phase, hematite (α-Fe_2O_3) having a rhombohedral crystalline structure JCPDS No: 01-089-0598 where peaks appear at 2θ: 33.130°,

35.683°, 40.951°, 49.405°and 64.003° correspond to lattice plane of (*104*), (*110*), (*113*), (*024*) and (*300*), respectively;

- Beta phase, β-Fe_2O_3 having a cubic crystalline structure according to JCPDS No: 00-039-0238 appears peaks at 2θ: 33.082°, 38.296°, 55.129°, and 65.945° correspond to lattice plane of (*222*), (*400*), (*440*) and (*622*), respectively. It is worth noting that for XRD reflection at 38.871° which is related to gamma phase is excluded because of its considerable shift.

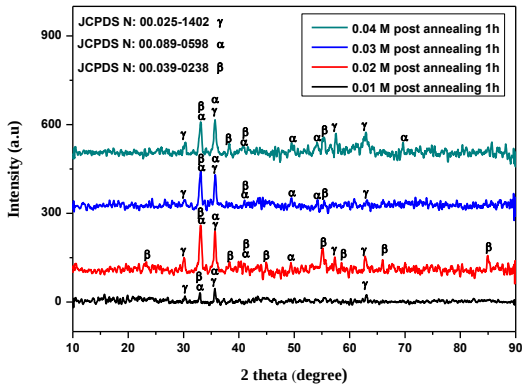

Figure III.2 : *X-ray diffraction patterns of sample 0.01M, 0.02M, 0.03M and 0.04M.(γ: γ-Fe_2O_3, α: α-Fe_2O_3, β: β-Fe_2O_3).*

The lattices constant(*a* and *c*), for the tetragonal phase structure, are determined by the relations [1] :

$$\boldsymbol{2d_{hkl}\sin(\theta) = n\lambda} \qquad \text{(III.1)}$$

And

$$\frac{1}{d_{hkl}^2} = \frac{h^2+k^2}{a^2} + \frac{l^2}{c^2} \qquad \text{(III.2)}$$

Where 'd_{hkl}' and (*hkl*) are the inter-planer distance and Miller indices, respectively. The values of lattice parameter '*a*' and 'c' are listed in Table 1. Values of *a* and *c* are (*a*=*b*= 8.3383Å, *c*= 25.0151Å) for instance in the case of 0.04M sample; they are the most close to the values of standard JCPDS data card, (a_0 =b_0 = 8.3400Å, c_0= 25.0200Å).

The lattice constants (*a* and *c*), for the rhombohedral phase structure, are determined by the relations [2]:

$$\frac{1}{d_{hkl}^2} = \frac{4}{3a^2}(h^2 + k^2 + hk) + \frac{l^2}{c^2} \qquad \text{(III.3)}$$

The values of lattice parameter '*a*' and 'c' are illustrated in Table 1. Values of *a* and *c* are (*a* = *b* = 5.0339Å and *c* = 13.7892Å) in the case of 0.03M sample; they are the most close to the values of standard JCPDS (a_0 =b_0= 5.0380 Å and c_0 = 13.7760Å).

For the beta phase structure, the lattice constant *a* is determined by the following relations of cubic unit [3]:

$$\frac{1}{d_{hkl}{}^2} = \frac{1}{a^2}\left(h^2 + k^2 + l^2\right) \qquad \text{(III.4)}$$

Values of *a*, are illustrated in Table 1. In the case of 0.01M sample, *a* is about 9.4022Å which is closely equal to 9.4040 Å of the JCPDS No: 00-039-0238 one.

The crystalline sizes of the powders, with different concentrations, are given in Table 1, They are calculated using Scherrer's formula [4]:

$$D = \frac{0.9\,\lambda}{\beta cos\theta} \qquad \text{(III.5)}$$

Where D, β, λ, and θ are the crystallite size, the full width at half-maximum (FWHM) of diffraction peaks, the X-ray wavelength (1.5406 Å) and Bragg angle, respectively. For more focus on the effect of concentration on the gain size of the products, it was remarked that the later has the same effect on all phases gain size variation as exhibited in Fig III.3.

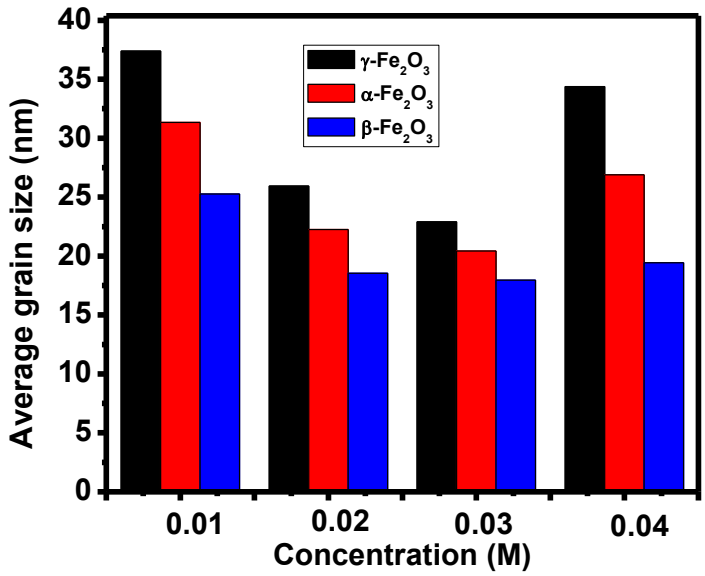

Figure III.3 : *Variation of average grain size with the concentration of the precursor $FeCl_3$*

Table III.1 : Crystallographic data obtained from XRD

Sample	Phases present	Av grain size (nm)	Calculated *d* (Å)	Standard *d* (Å)	Lattice parameters *a* (Å), *b* (Å), *c* (Å)
0.01 M	γ-Fe_2O_3	37.39043	2.51576	2.51400	*a* = *b* = 8.3438, *c* = 25.0314
	α-Fe_2O_3	31.32887	2.71418	2.70329	*a* = *b* =5.0315, *c* = 13.8775
	β-Fe_2O_3	25.25763	2.71418	2.71400	*a* = 9.4022
0.02 M	γ-Fe_2O_3	25.94565	2.51383	2.51400	*a*= *b* = 8.3374, *c* = 25.0123
	α-Fe_2O_3	22.24205	2.70650	2.70329	*a* = *b* =5.0361, *c* = 13.8101
	Fe_2O_3	18.54299	2.70650	2.71400	*a* = 9.3756
0.03 M	γ-Fe_2O_3	22.91024	2.51698	2.51400	*a*= *b* = 8.3374, *c* =24.9904
	α-Fe_2O_3	20.43640	2.70409	2.70329	*a* = *b* =5.0339, *c* = 13.7892
	Fe_2O_3	17.96256	2.70409	2.71400	*a* = 9.3671
0.04 M	γ-Fe_2O_3	34.36907	2.51679	2.51400	*a*= *b* =8.3383, *c* = 25.0151
	α-Fe_2O_3	26.89509	2.70397	2.70329	*a* = *b* =5.0336,c = 13.7892
	Fe_2O_3	19.42119	2.70397	2.71400	*a* = 9.3668

III.3.2. Surface morphology:

The surface morphology of iron oxide powders are studied using SEM images, for different magnification 5µm for the first concentration and 1µm for the rest, Fig III.4a-d shows the results with different concentration of $FeCl_3$: 0.01, 0.02, 0.03 and 0.04M, respectively. It is clear that iron oxide NPs are mainly present as granules with spherical shaped particles. The agglomeration of particles behave as in the case of XRD. They begin with spherical shaped particles of about 1.2 µm then decreases to 0.8- 0.5 µm for concentration of 0.02, 0.03 and increases to attain 1 µm for the concentration of 0.04M. To have idea about the composition of NPs, EDAX for one sample is reported in this study; it reveals that the samples are composed of iron and oxygen in rate of 2, as shown in the EDAX table below (Fig III.4e), which means a non stichiometric composition of the elaborated iron oxides NPs.

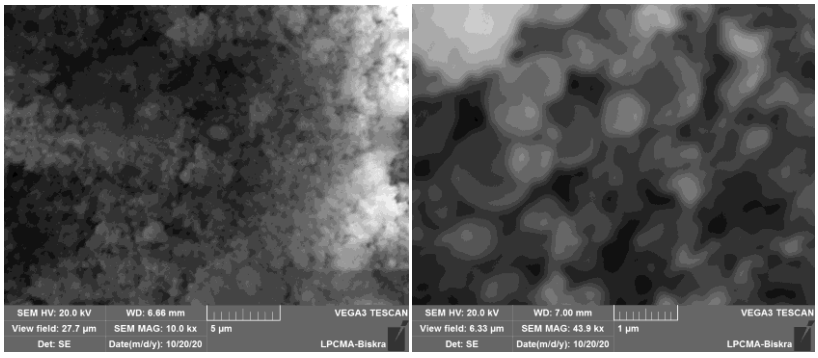

(a) (b)

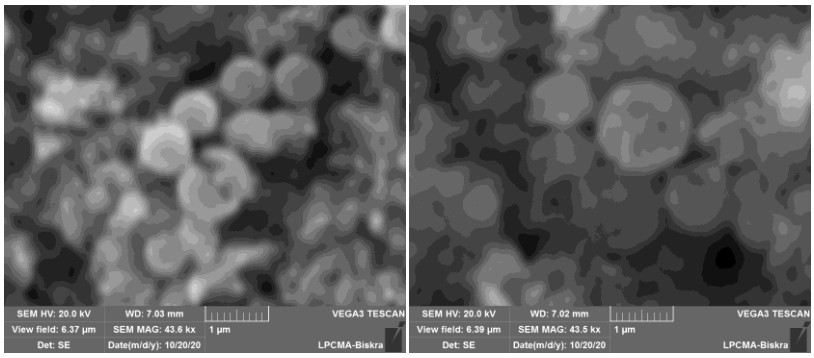

(c) (d)

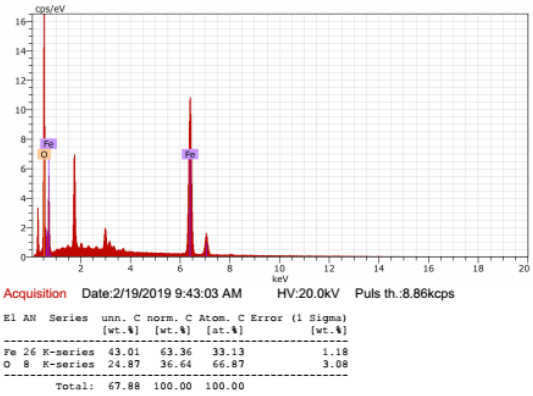

(e)

Figure III.4: *Scanning electron microscopic images of Iron oxide NPs powders:(a) 0.01M, (b) 0.02M, (c) 0.03M and (d) 0.04M., (e) EDAX*

III.3.3. Optical properties:

In order to investigate the band gap of the iron oxide NPs powders, Tauc's relation is used [5]:

$$\boldsymbol{\alpha h\nu = A(h\nu - Eg)^n} \quad \text{(III.6)}$$

Where α, *h*, *v,* and $E_g$are the absorption parameter, Planck constant, the photon frequency and gap energy, respectively; ***A*** is a constant and *n* is taken 1/2 based on consideration that γ-Fe_2O_3 and α-Fe_2O_3 have direct gap [38,39]. The optical absorption data was used to generate plots of $(\alpha h\nu)^2$ vs $(h\nu)$, as shown in Fig III.5. leading to band gap energy which was estimated by extrapolating the straight line of $(\alpha h\nu)^2$ to $h\nu$ axis.

Visual results were obtained using two techniques: The first technique is that we used the KBr salt by making tablets of KBr salt with a mass of 0.198g KBr and . 0.002g of NPs powder the considered sample composted under disc shape (1cm

x1mm). Whereas for the second technique, acetone acid was used by taking a volume10ml of it with the addition of 0.002g from NPs powder of the considered sample and then placing it in the ultrason apparatus for agitation

Optical values of the elaborated samples are given in Table III.2. As shown leading to band gap energy for first technique of 2.153 , 2.307, 2.326, and 2.234ev for concentrations 0.01, 0.02, 0.03 and 0.04M, respectively

For the second technique the band gaps were about 2.162 , 2.295, 2.358, and 2.218ev for concentrations 0.01, 0.02, 0.03 and 0.04M, respectively.

The results were very similar for both techniques. And those values are in agreement with several previous works [6–9].

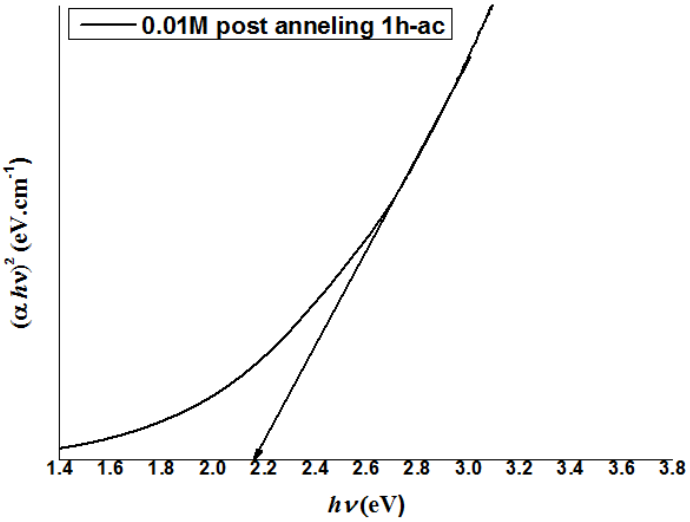

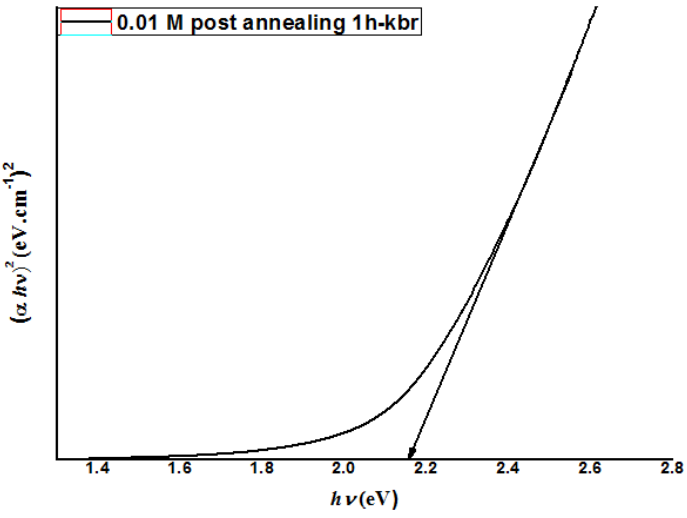

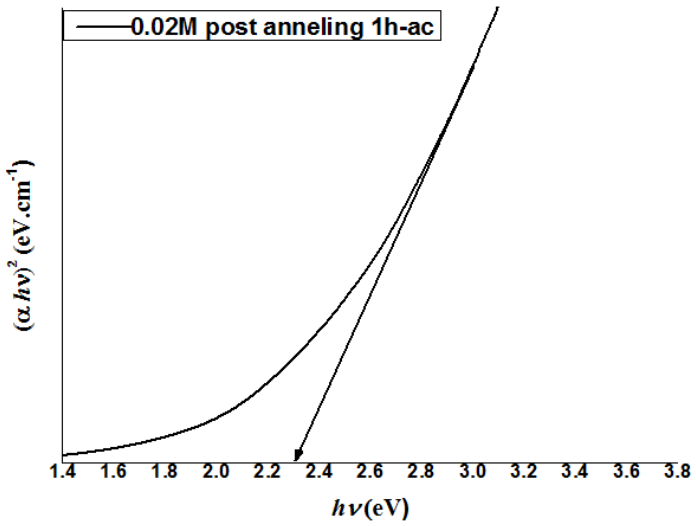
0.02M post anneling 1h-ac
$(\alpha h\nu)^2$ (eV.cm^{-1})
1.4 1.6 1.8 2.0 2.2 2.4 2.6 2.8 3.0 3.2 3.4 3.6 3.8
$h\nu$(eV)

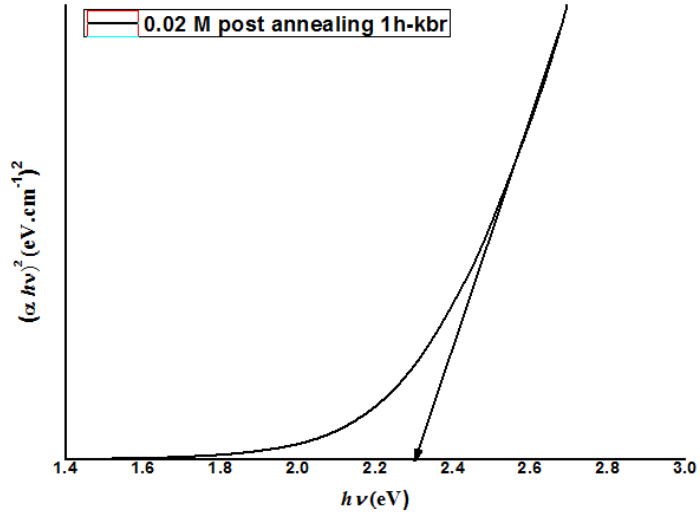
0.02 M post annealing 1h-kbr
$(\alpha h\nu)^2$ (eV.cm^{-1})^2
1.4 1.6 1.8 2.0 2.2 2.4 2.6 2.8 3.0
$h\nu$(eV)

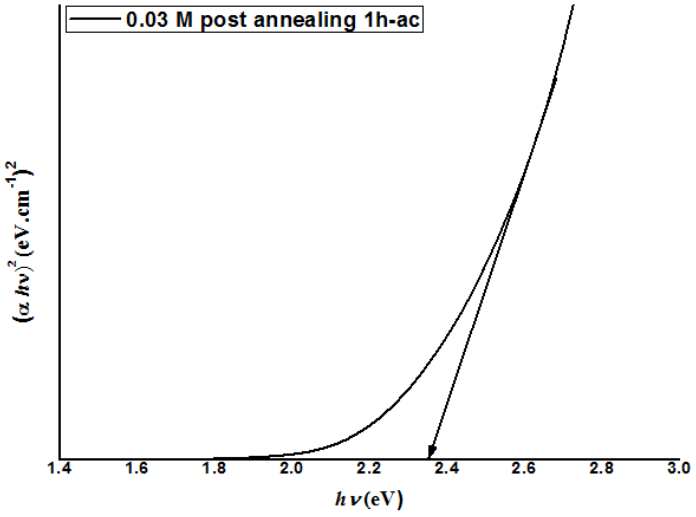
0.03 M post annealing 1h-ac
$(\alpha h\nu)^2$ (eV.cm^{-1})^2
1.4 1.6 1.8 2.0 2.2 2.4 2.6 2.8 3.0
$h\nu$(eV)

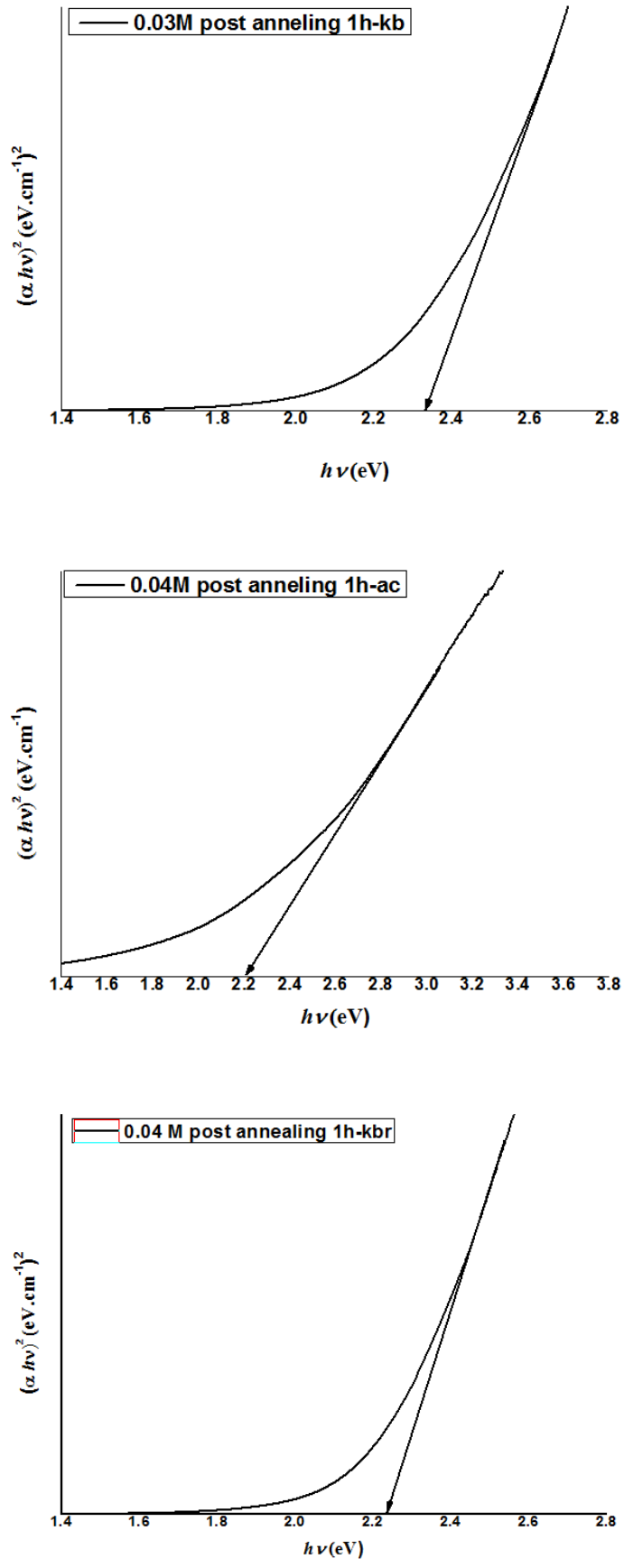

Figure III.5: *Band gap (E_g) estimation from Tauc's relation for iron oxide NPs Powders.*

Table III.2 : Optical gap of green synthesized iron oxide NPs.

Concentration (M)	*Eg(eV)*- kbr	E_g(eV)- ac
0.01	2.153	2.162
0.02	2.307	2.295
0.03	2.326	2.358
0.04	2.234	2.218

III.3.4. FTIR:

Fig III.6 shows FTIR spectrum of the synthesized samples with different precursor concentrations. The bands in the range of 400-900 cm^{-1} are related to Fe-O lattice vibration. As exhibits in the figure bands at 562, 633 and 692 cm^{-1} are related at maghemite phase formation whereas bands at 542, 573cm^{-1} describes the formation of hematite phase [10] and band 528cm^{-1} is related at beta phase[11] . The peak 800 cm−1 is related to O–H out of plane bond[10].

Absorption peaks at 1106 and 3420 cm^{-1} also appeared, may be they assigned to C–O vibration mode [12], and to O–H stretching vibration [13].

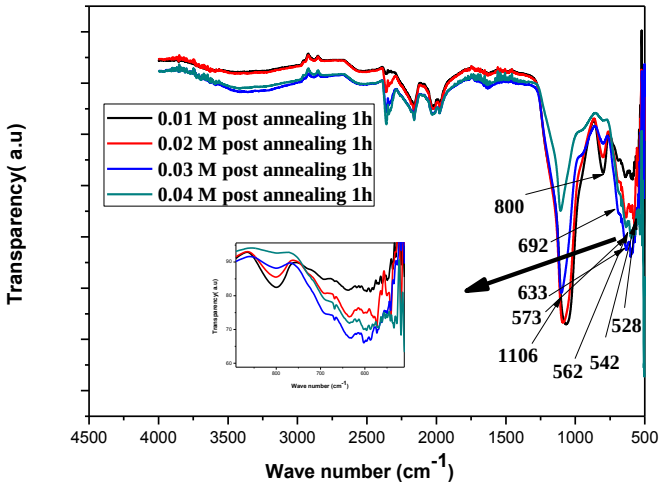

Figure III.6: *FTIR spectrum of iron oxide NPs powders for (0.01–0.04M) post annealing at 500°C.*

III.4. Evans Blue Preferential and Adsorption Enhancer on the Surfaces of Fe_2O_3 NPs:

In the same study, it was chosen as application adsorption of EB on the surfaces of the green-synthesized Fe_2O_3 NPs. the preferential and enhanced

adsorption of EB on the surfaces of four green-synthesized Fe_2O_3 NPs under two different conditions (dark as first process and under UV irradiation (365 nm) as photocatalysis) will be investigated.

The preferential adsorption process of EB on the surfaces of the four samples under ambient dark conditions will be taken in consideration first, then the residual EB/Fe_2O_3 solutions will be used for second study under an enhancement of the adsorption by photocatalysis under UV irradiation (365 nm).

To be more clear, a molecular structure of Evans Blue used in this application will be showed in the following figure:

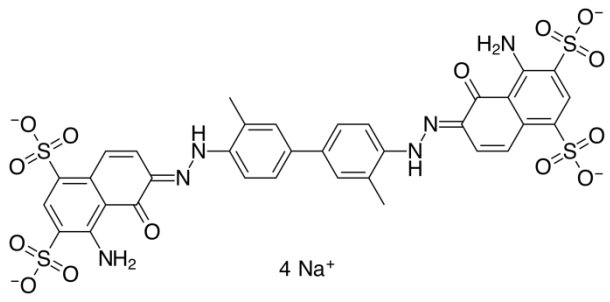

Figure III.7 : *Molecular structure of Evans Blue*.

III.4.1. Materials and methods:

This section focuses on inventorying the required materials and used equipment. It also provides the methods used to perform adsorption experiments.

III.4.1.1. Materials:

Evans blue dye, sodium chloride salt, synthesized green Fe_2O_3 prepared previously with concentrations 0.01,0.02,0.03, and 0.04M.

III.4.1.2. Methods:

To deal with the prepared solutions only UV-visible apparatus is used to determine the residual EB adsorption**.**

III.4.2. Adsorption experiments of EB on Fe2O3 NPs in dark ambient conditions:

First, the prepared aqueous solutions of EB dye were diluted as many times as needed. Second, 0.0015 g of Fe_2O_3 NPs of the four manufactured powders was added

to a volume of 4 ml of dye aqueous solutions. The concentration of the dye solutions was 0.0111 mg/ml.

The ionic strength for all adsorption experiments was maintained at 0.1 M by adding an appropriate amount of NaCl (0.023 g). All adsorption studies were conducted at room temperature and at given pH. All experimental adsorption were sonicated in an ultrasonic bath for 15 minute and then its where continuously stirred for 60 minutes until a steady state was reached A control experiment (without NPs) was also performed as standard sample. All adsorption experiments were performed in dark ambient conditions.

Concentrations of residual dye aqueous solutions were quantified using a UV-visible spectrophotometer at maximum EB absorption λ_{max} = 602 nm which was determined experimentally. Moreover, the adsorbed amounts of EB particles are calculated from the calibration curve for all adsorptions. In order to obtain the adsorption capacity q_e(mg/g) at the equilibrium. The amount of EB cations at (t) adsorbed per unit mass (q_t in (mg/g)) in the solution containng the Fe_2O_3 NPs at the contact time under dark conditions of EB adsorption, the following equations were used [14]:

$$q_e = \frac{(C_0 - C_e)V}{m} \quad \text{(III-7);}$$

$$q_t = \frac{(C_0 - C_t)V}{m} \quad \text{(III-8);}$$

And the adsorption yield η is calculated according to the following equation [15]:

$$\eta\ \% = \frac{(C_0 - C_e)}{C_0}.100 \quad \text{(III-9)}$$

Where C_0, C_e, C_t,V and m are: initial dye concentration without any treatment ($mg.ml^{-1}$), dye concentration remaining at equilibrium, dye concentration at time t under dark conditions ($mg.ml^{-1}$), dye solution volume (ml) a respectively, and the amount of the Fe_2O_3 NPs (g).

III.4.2.1. Kinetic models of adsorption:

III.4.2.1.1. Pseudo-First-order and Pseudo-Second-Order Kinetics:

The pseudo-first-order (PFO) kinetic models of Lagergren [16] and pseudo-second-order models of Ho and McKay [17] in kinetic equation are widely used for adsorbing a dense substance from an aqueous solution. The Lagergren model (eq.III-

10) is only suitable for the first 20-30 min of the adsorption procedure and not for the full range of contact times [17]. In general, it is represented by the following equations:

$$\frac{dq_t}{dt} = K_1(q_e - q_t) \quad \text{(III-9)}$$

After merging by applying the terms, $q_t = 0$ at $t = 0$ and $q_t = q_t$ at $t = t$ then (eq.III-9) becomes after integration as follows:

$$ln(q_e - q_t) = lnq_e - K_1 t \quad \text{(III-10)}$$

Where, K_1, q_t and q_e are respectively: pseudo-first-order kinetic constant (mn^{-1}), the amount of dye absorbed after a moment t ($mg.g^{-1}$) and amount of dye adsorbed at thermodynamic equilibrium under considered conditions ($mg.g^{-1}$). (in our study dark ambient conditions)

If the active surface area of the adsorbent is considered to be invariant, the reaction could be treated as pseudo-first-order kinetics. However, when the active sites are saturated, the transfer at the pollutant/adsorbent particle interface can be limited by mass transfer.

The pseudo-second order (PSO) model (eq.III-11) is proposed by Ho and McKay [17]. It is based on adsorption capacity articulated as follows:

$$\frac{t}{q_t} = \frac{1}{K_2 q_e^2} + \frac{t}{q_e} \quad \text{(III-11)}$$

Where, K_2, q_t and q_e are respectively: the pseudo-second-order kinetic constant ($mg.g^{-1}.\ mn^{-1}$), the amount of dye adsorbed at time t ($mg.g^{-1}$) and the amount of dye adsorbed at thermodynamic equilibrium condition ($mg.g^{-1}$).

Such equations are used depending on the behavior of adsorbent/pollutant.

III.4.2.1.2. Intra-particle diffusion kinetics:

To understand the mechanisms of adsorption more widely, a homogeneous particle diffusion model (HPDM) as shown in Eq. III-12, originally proposed by Boyd et al. [18], is used to describe the process of diffusive adsorption. In this model, the rate-limiting step is usually described either by intra-particle diffusion or by a film diffusion mechanism.

$$X(t) = 1 - \frac{6}{\pi^2}\sum_{Z=1}^{\infty}\frac{1}{Z^2}\exp\left(\frac{-Z^2\pi^2 D_p t}{r_0^2}\right) \quad \text{(III-12)}$$

Where X(t) is the fraction reached at time t, i.e. $X(t) = q_t/q_e$, Dp (m2/s) is the effective diffusion coefficient, r_0 is the particle radius of Fe_2O_3 assumed to be spherical, and Z is an integer. For $0 < X(t) < 1$, a simplified equation can be obtained for adsorption on spherical particles using Vermeulen's approximation [19].

$$X^2(t) = 1 - \exp\left(2\,\frac{\pi^2 D_p}{r_0^2}t\right) \quad \text{(III-13)}$$

This equation can be further simplified to cover most of the data points to calculate effective particle diffusion using next expression:

$$-\ln(1 - X^2(t)) = \frac{2D_p\pi^2 t}{r_0^2} = 2k_p t \quad \text{(III-14)}$$

Where k_p is the diffusion rate constant (1/s) and $k_p = D_p\pi^2/r_0^2$. Eq III-14 was used to calculate the *effective intra-particle diffusivity* (D_p(m^2/s)) from the experimental data. In the first step, a graph of $-\ln(1 - X^2(t))$ vs *t* was developed. The k_p values of the adsorption processes EB –Fe_2O_3 are obtained from the slopes of the fitted lines (plots of $-\ln(1 - X^2)$as a function of time), and the values of the effective diffusion coefficients, D_p(m^2/s), can then be obtained from $D_p = k_p r_0^2/\ \pi^2$.

If the *diffusion of the liquid film* controls the rate of absorption, the following related expression can be used, Eq. III-15 [20]

$$X(t) = 1 - \exp\left(-\frac{3D_f C_e}{r_0\tau C_r}t\right) \quad \text{(III-15)}$$

Where D_f is the diffusion coefficient of the film (m^2/s) in the liquid phase whereas C_e (mol/l) and C_r (mol/l) are the equilibrium concentrations of the EB dye in solution and in solid phase, respectively. τ is the liquid film thickness which was assumed to be 10^{-5} m according to Yu and Luo [21].

Another deformation formula from Eq. III-15 gives the following equation:

$$-\ln(1 - X) = K_f t \quad \text{(III-16)}$$

Where k_f is the diffusion rate constant ($1.s^{-1}$).

The values of $k_f = 3D_f C_e/r_0\tau C_r$ of EB adsorption on the Fe_2O_3 NPs surfaces are obtained from the slopes of the fitted lines (plots of $-\ln(1 - X)$ vs *t*), and the values of the effective diffusion coefficient, D_f (m^2/s), can then be obtained from $D_f = k_f r_0\tau C_r/3C_e$.

The linearity test of Boyd plots ($-\ln(1-X)$ and $-ln(1-X^2)$) vs *t* is used to distinguish adsorption mechanisms controlled by film diffusion or particle diffusion.

If the plot of $-\ln(1-X)$ vs *t* is a straight line passing through the origin, then the adsorption rate is governed by the particle diffusion mechanism otherwise if $-ln(1-X^2)$ vs *t* is a straight line passing through the origin then the adsorption is governed by the diffusion of the film.

III.4.3. Batch Photocatalysis Experiments of Fe_2O_3 NPs Samples in Ambient Conditions

In the second EB absorption process, the study of photocatalysis of Fe_2O_3 NPs under UV irradiation to degrade EB are conducted on all sets of experiment containing remaining solutions after the first process of EB adsorption in dark conditions. All experiment sets are sonicated in an ultrasonic bath for 15 min and then they are stirred constantly and exposed to direct UV irradiation (365 nm) in ambient conditions at different times ranging from 60 to 240 minutes. The concentrations of residual dye aqueous were quantified using UV-Vis spectrophotometer at absorbance maxima of EB $\lambda_{max} = 602\ nm$. In addition, the absorbed amounts of EB molecules are calculated from the calibration curve for all absorption experiments . In order to obtain the absorption capacity q_e^* (mg/g) by photocatalysis in ambient conditions under UV irradiation of Fe_2O_3 NPs the following equations are used :

$$q_e^* = \frac{(C_0 - C_e^*)V}{m} \quad \text{(III-17)}$$

The adsorption yield was calculated using the following equation:

$$\eta^*\% = \frac{(C_0 - C_e^*)}{C_0}.100 \quad \text{(III-18)}$$

Where, C_0, C_e^*,V and m are respectively: Initial dye concentration without any treatment (mg/ml), Residual dye concentration in the liquid phase after photocatalysis in the second process of EB adsorption at ambient conditions (mg/ml) under UV irradiation, the volume of dye solution (ml) and the mass of Fe_2O_3 NPs (g).

The degradation kinetics EB using Fe_2O_3 NPs can be expressed as pseudo-second-order (PSO) reaction as follows [22]:

$$\frac{1}{C_t^*} - \frac{1}{C_0} = k_{pd}t \quad \text{(III-19)}$$

Where, C_0 , C_t^* , and k_{pd} are respectively the initial concentration of EB without any treatment ($mg.g^{-1}$), the concentration of the residual dye ($mg.g^{-1}$)in

the liquid phase at time t after photocatalysis under UV irradiation, and the PSO photocatalytic rate constant (min^{-1}) which can be calculated from the slope of $(\frac{1}{C_t^*} - \frac{1}{C_0})$ against the t plot.

III.4.4. Adsorption kinetics analysis:

III.4.4.1. Adsorption equilibrium in preferential EB adsorption:

In all adsorption experiments, the steady state is reached within 30 min, as shown in Fig III.8. This indicates the very fast adsorption kinetics of EB on all NPs surfaces

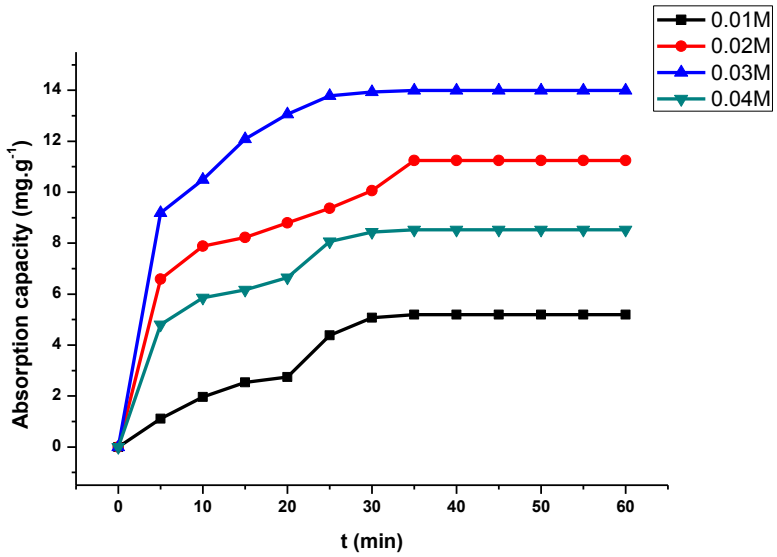

Figure III.8 : *The adsorption capacity of EB to the four samples in the first process of EB adsorption in the dark surrounding conditions*

III.4.4.2. Pseudo-first-order and pseudo-second-order kinetics of preferential EB adsorption:

The results of the analysis of pseudo- second -order kinetics for adsorption of EB particles on the four NPs surfaces (Table III.3 and Fig III.9(a))indicate good linearity and good fit of the experimental data for this model compared to the pseudo-first -order model which indicated poor linearity and poor fit of the experimental data (Table III.3 and FigIII.9(b)). The q_e (equilibrium absorption amplitude) calculated from the pseudo- second -order kinetic plots is also in very close agreement with the empirical qe in contrast to the q_e calculated from the pseudo- first -order plots (see Table III.3). This indicates the best compliance of EB adsorption on all surfaces of the iron oxide NPs with pseudo-second-order kinetics.

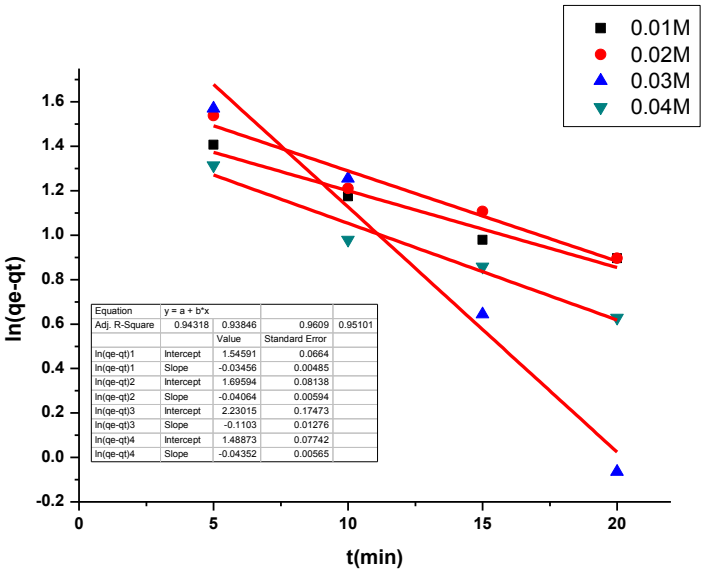

(a)

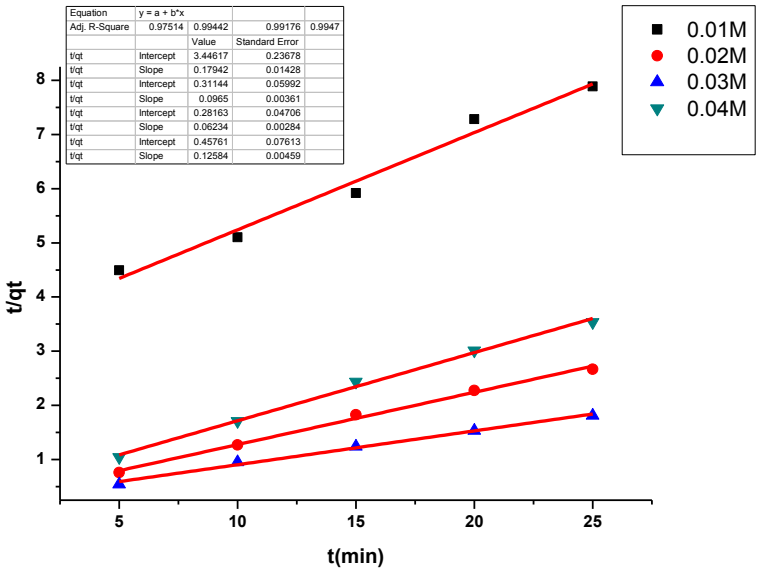

(b)

Figure III.9: (*a) Plots of* $ln(q_e - q_t)$ *versus time and (b) plots of* $\frac{t}{q_t}$ *versus time of EB adsorption on the iron oxide NPs samples in the first process of adsorption*

Table III.3: Adsorption kinetic parameters of EB adsorption on the iron oxide NPs samples in dark ambient conditions

Sample	$q_{e,exp}$ $(mg.g^{-1})$	$q_{e,cal}$ $(mg.g^{-1})$	$k_1.10^{-3}$ (mn^{-1})	R^2	$q_{e,cal}$ $(mg.g^{-1})$	$k_2.10^{-1}$ $(mg.g^{-1}.mn^{-1})$	R^2
0.01M	5.19	4.68	1.36	0.9431	5.58	0.09	0.9751
0.02M	11.24	5.44	1.6	0.9384	10.41	3.08	0.9944
0.03M	13.99	9.29	4.4	0.9609	16.12	2.21	0.9917
0.04M	8.52	3.45	1.1	0.9510	7.63	0.51	0.9947

III.4.5. Intramolecular diffusion kinetics of preferential EB adsorption:

Linearity tests of Boyd's plots ($-\ln(1-X)$ and $-ln(1-X^2)$) versus time are shown in the two Fig III.10(a) and III.10(b). They show that the kinetic data correlate well with the homogeneous particle diffusion model as confirmed by the high R^2 values. The results of the linear regression analysis of the equations (9) and (11) are existing in Table III.4. The film diffusion coefficients D_f and intra-particle diffusion coefficients D_p were found in the order of 10^{-17} $m^2.s^{-1}$. As is notorious, the adsorption mechanism is controlled by the diffusion of the film at D_f in the range (10^{-10}-10^{-12}) $m^2.s^{-1}$, Whereas intra-particle diffusion is a rate-limiting step at D_p in the range (10^{-15}-10^{-17}) $m^2.s^{-1}$[23]. The obtained results are in agreement with the previous results, which confirm that intra-particle diffusion is this step.

Table III.4. Diffusion parameters of homogeneous particles calculated in the first process of EB adsorption on the four samples

Sample	$r_0.10^{-9}$ (m^{-1})	k_p s^{-1}	R^2	$D_p.10^{-17}$ $m.s^{-2}$	$k_f.10^{-3}$ s^{-1}	R^2	C_r ($\boldsymbol{mg.g^{-1}}$)	C_a ($\boldsymbol{mg.g^{-1}}$)	$D_f.10^{-17}$ $m.s^{-2}$
0.01M	31.32	0.60	0.9848	5.97	0.55	0.9717	0.009152	0.001948	1.22
0.02M	22.24	1.08	0.9717	5.42	0.70	0.9625	0.006884	0.004216	3.17
0.03M	20.43	0.61	0.9817	2.58	0.24	0.9552	0.005852	0.005248	1.46
0.04M	26.89	0.38	0.9656	2.82	0.56	0.9384	0.007904	0.003196	2.05

It controls the mechanism of EB adsorption on the iron oxide NPs surfaces, which is consistent with the pseudo-second-order kinetic model.

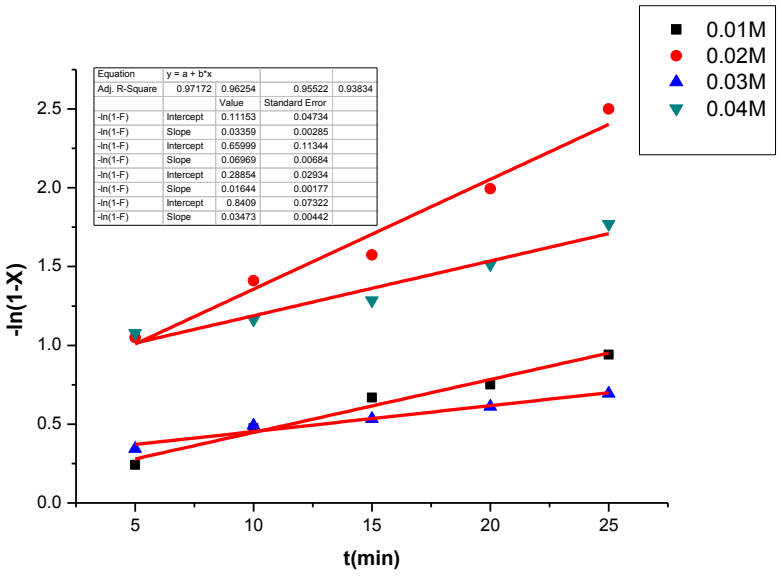

(a)

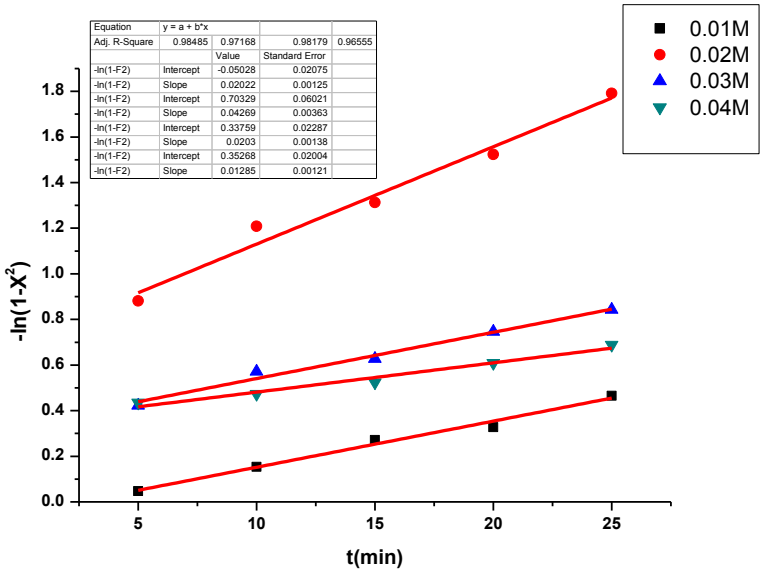

(b)

Figure III.10: (a) body plots of $-\ln(1-X)$ versus time and (b) body plots of $-ln(1-X^2)$ versus time of EB adsorption on the iron oxide NPs samples in the first process of adsorption

III.4.6. Pseudo-second-Order Kinetic Analysis of EB Adsorption Under Photocatalysis Process:

Results of pseudo-second-order kinetic analysis of EB adsorption on the iron oxide NPs surfaces (Fig III.11) Indicates the good sin of plots $(\frac{1}{C_t^*}-\frac{1}{C_0})$ versus time of UV radiation as judged by its high correlation coefficient

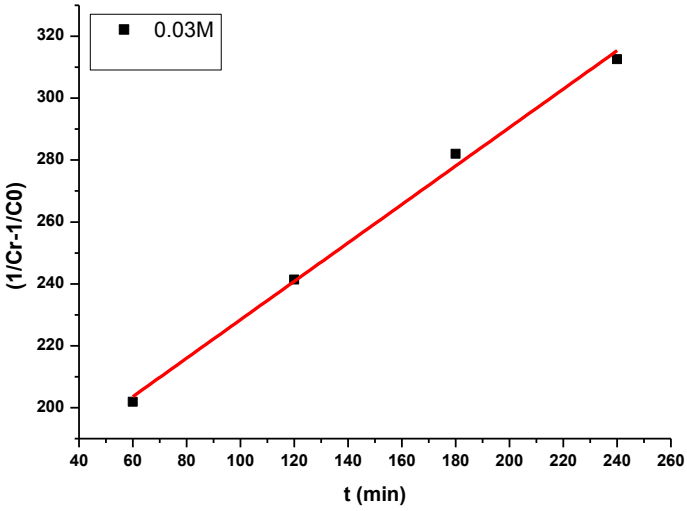

Figure III.11: *Kinetic plot of $(\frac{1}{C_t^*}-\frac{1}{C_0})$ versus time of EB degradation catalyzed by the iron oxide NPs for the sample with concentration 0.03M*

(R^2 = 0.994), Which indicates that the rate of EB degradation catalyzed by the iron oxide NPs samples is assumed to be fitted by a pseudo-second- order model. Corresponding photolysis rate. Corresponding photolysis rate (k_{pd}) of EB 0.03M on the iron oxide NPs is 0.621 min^{-1}.

III.4.7. Preferential and enhanced EB adsorption on the Fe_2O_3 NPs surfaces:

III.4.7.1. Preferential Adsorption of EB Adsorption:

TableIII.5 shows that in the first process of EB adsorption in ambient dark conditions, the adsorption capacity and EB yield vary depending on the Fe_2O_3 NPs samples. EB adsorption capacity (indicated adsorption capacity q_e) and yield (indicated R%) achieved 13.99 $mg.g^{-1}$ and 47.28% When the sample has a concentration of 0.03M.

Table III.5: *Reached EB adsorption capacity and yield of 0.01,0.02,0.03 and 0.04M OF the Fe_2O_3 NPs samples in the first process of EB adsorption in ambient dark conditions*

Absorbent	$q_e(mg.g^{-1})$	EB η %
0.01M	5.19	17.55
0.02M	11.24	37.98
0.03M	13.99	47.28
0.04M	8.52	28.79

Through the results shown in the table III.5, we note that the adsorption yield is inversely proportional to the size of the prepared nanoparticles, as it was greatest 47.27% at sample 0.03M with crystal size 20.43 nm, then 37.98% at sample 0.02M with crystal size 22.24 nm, then 28.79% at sample 0.04M with crystal size 26.89 nm, and finally 17.55% at sample 0.01Mwith crystal size 31.32 nm

III.4.7.2. Enhancement of EB adsorption through photo catalysis :

To evaluate the improvement of EB Adsorption by photo catalysis, the photo catalytic On the remaining solution of EB/Fe_2O_3 on sample 0.03M after EB adsorption in the first process of EB adsorption in ambient dark conditions, to give yields and total adsorption capacities after enhancement by photo catalysis and to allow comparison between the yields and adsorption capacities before and after application of photo catalysis. The effect of photo catalysis on EB adsorption on

sample 0.03M is evaluated by evaluating the photolysis efficiency of EB under UV irradiation (365 nm) in the time range from 60 to 240 min at ambient conditions.

The table III.6 shows the variation in the EB adsorption yield, as well as the adsorption capacity by photo catalysis.

Table III.6: Enhancement of adsorption yield and EB capacity on Fe_2O_3 NPs surfaces by photo catalysis at ambient conditions.

Sample	**0 min**		**60 min**		**120 min**		**180 min**		**240 min**	
	q_e (mg.g^{-1})	η%	q_e^* (mg.g^{-1})	η*%	q_e^* (mg.g^{-1})	η*%	q_e^* (mg.g^{-1})	η*%	q_e^* (mg.g^{-1})	η*%
0.03M	13.99	47.28	20.47	69.15	21.56	72.82	22.43	75.79	22.96	77.62

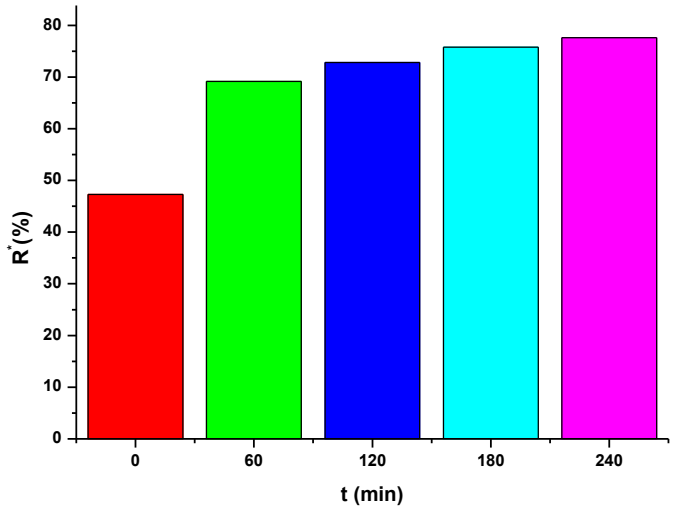

Figure III.12: *The enhanced EB adsorption yield on Fe_2O_3 NPs sample 0.03M by photo catalysis in ambient conditions*

III.5. Conclusion:

As conclusion to this characterizations of iron oxide NPs powders:

In this context, Iron oxide NPs powders were synthesized by green synthesis method using the extract of PHEONIXDACTYLIFERA L with a triple iron chlorine solution. The effect of salt concentration in the extract: 0.01M, 0.02M, 0.03M and 0.04M concentrations and post heat treatment at 500°C on their structural and optical

properties have been studied. XRD analyses three iron oxide were formed of NPs as essentials compounds: maghemite phase, hematite phase and beta phase whereas the grain size varies upon concentration iron chlorine. It was arranged in 22.91–37.40nm, 20.41–31.32nm and 17.96–25.25nm respectively. SEM images showed that all samples having spherical shaped particles. With direct band gap in the range of 2.162–2.358eV. In addition to that FTIR spectra affirm the abundance of Fe-O bond.

We note that the yield is inversely proportional to the size of the prepared nanoparticles, as it was greatest 47.27% at sample 0.03M with crystal size 20.43 nm, then 37.98% at sample 0.02M with crystal size 22.24 nm, then 28.79% at sample 0.04M with crystal size 26.89 nm, and finally 17.55% at sample 0.01Mwith crystal size 31.32 nm.

References

[1] Kittel, Charles. Introduction to solid state physics. John Wiley & sons, inc, 2005.

[2] Dghoughi, L., et al. "Physico-chemical, optical and electrochemical properties of iron oxide thin films prepared by spray pyrolysis." Applied Surface Science 253.4 (2006): 1823-1829.

[3] Sadanandan, A. K., and M. Jacob Mathew. "A novel route for the synthesis of gamma phased Fe2O3 nano particles through polymer assisted spray pyrolysis." AIP Conference Proceedings. Vol. 2162. No. 1. AIP Publishing LLC, 2019.

[4] Abdullah, Mikrajuddin, and Khairurrijal Khairurrijal. "Derivation of Scherrer relation using an approach in basic physics course." Jurnal Nanosains & Nanoteknologi 1.1 (2009): 28-32.

[5] Tauc, J., Radu Grigorovici, and Anina Vancu. "Optical properties and electronic structure of amorphous germanium." physica status solidi (b) 15.2 (1966): 627-637.

[6] Mallick, P., and B. N. Dash. "X-ray diffraction and UV-visible characterizations of α-Fe2O3 nanoparticles annealed at different temperature." Nanosci. Nanotechnol 3.5 (2013): 130-134.

[7] Goyal, Rajendra N., Davinder Kaur, and Ashish K. Pandey. "Growth and characterization of iron oxide nanocrystalline thin films via low-cost ultrasonic spray pyrolysis." Materials Chemistry and Physics 116.2-3 (2009): 638-644.

[8] Liu, Jianxing, He Yang, and Xiangxin Xue. "A new and simple route to prepare γ-Fe2O3 with iron oxide scale." Materials Letters 229 (2018): 156-159.

[9] Wei, Zhiwei, et al. "Preparation and visible-light photocatalytic activity of α-Fe2O3/γ-Fe2O3 magnetic heterophase photocatalyst." Materials Letters 118 (2014): 107-110.

[10] Ates, Mehmet, et al. "Assessment of impact of α-Fe2O3 and γ-Fe2O3 nanoparticles on phytoplankton species Selenastrum capricornutum and Nannochloropsis oculata." Environmental toxicology 35.3 (2020): 385-394.

[11] Aziz, Wisam J., et al. "Synthesis of iron oxide (β-fe2o3) nanoparticles from Iraqi grapes extract and its biomedical application." IOP Conference Series: Materials Science and Engineering. Vol. 881. No. 1. IOP Publishing, 2020.

[12] Khalil, Ali Talha, et al. "Biosynthesis of iron oxide (Fe2O3) nanoparticles via aqueous extracts of Sageretia thea (Osbeck.) and their pharmacognostic properties." Green Chemistry Letters and Reviews 10.4 (2017): 186-201.

[13] Ding, Jie, Qin Zhong, and Shule Zhang. "Catalytic efficiency of iron oxides in decomposition of H2O2 for simultaneous NOX and SO2 removal: Effect of calcination temperature." Journal of Molecular Catalysis A: Chemical 393 (2014): 222-231.

[14] Ezzati, Rohollah. "Derivation of pseudo-first-order, pseudo-second-order and modified pseudo-first-order rate equations from Langmuir and Freundlich isotherms for adsorption." Chemical Engineering Journal 392 (2020): 123705

[15] Rauf, Muhammad A., et al. "Photocatalytic degradation of methylene blue using a mixed catalyst and product analysis by LC/MS." Chemical Engineering Journal 157.2-3 (2010): 373-378.

[16] Lagergren, S. Kung. "About the theory of so-called adsorption of soluble substances." Sven. Vetenskapsakad. Handingarl 24 (1898): 1-39

[17] Ho, Yuh-Shan, and Gordon McKay. "Pseudo-second order model for sorption processes." Process biochemistry 34.5 (1999): 451-465.

[18] Boyd, G. E., Ac W. Adamson, and L. S. Myers Jr. "The exchange adsorption of ions from aqueous solutions by organic zeolites. II. Kinetics1." Journal of the American Chemical Society 69.11 (1947): 2836-2848.

[19] Valderrama, C., et al. "Kinetic study of acid red “dye” removal by activated carbon and hyper-cross-linked polymeric sorbents Macronet Hypersol MN200 and MN300." Reactive and Functional Polymers 68.3 (2008): 718-731.

[20] Valderrama, C., et al. "Sorption kinetics of polycyclic aromatic hydrocarbons removal using granular activated carbon: intraparticle diffusion coefficients." Journal of hazardous materials 157.2-3 (2008): 386-396.

[22] Rauf, Muhammad A., et al. "Photocatalytic degradation of methylene blue using a mixed catalyst and product analysis by LC/MS." Chemical Engineering Journal 157.2-3 (2010): 373-378.

[23] Yu, Lei, and Yong-Ming Luo. "The adsorption mechanism of anionic and cationic dyes by Jerusalem artichoke stalk-based mesoporous activated carbon." Journal of Environmental Chemical Engineering 2.1 (2014): 220-229.

CHAPTER VI
Effect of annealing time on the type of product

IV.1.Introduction:

The aim of this chapter is to study the structural and optical properties of iron oxides nanoparticles greenly synthesized by reacting the ethanolic extract of *Phoenix dactylifera. L* with concentration iron chloride (FeCl3) of salt at 0.03M in aqueous solution. With the change of annealing time at 500°C annealed products for (0–3) hours, will be analyzed using XRD, UV–VIS, SEM and FTIR.

IV.2. Experimental details:

IV.2.1.Preparing and extracting plant materials:

The preparation is carried out in the same manner as mentioned in Chapter (III)

IV.2.2.Preparation of iron oxide nanoparticles:

Iron oxide NPs are synthesized by reacting 40ml of the (L.E.L.E) with concentration 0.03M of FeCl3 aqueous solution of 80ml for each experimentation. The mixture has obeying to continuous stirring, in a water bath system at 70°C, for one hour. Iron oxide particles formation starts when the change in the color of the mixture, from green to dark brown, appears. After that, the blend was dried and the residual products was washed several times with distilled water and collected by centrifugation. The collected product was dried again at 90-100°C inside a drying oven. Finally, Iron oxide NPs were obtained after annealing treatment at 500°C, into a special oven, for 1, 2 and 3hours. Photos of the prepared powders are shown in Fig. IV.1.

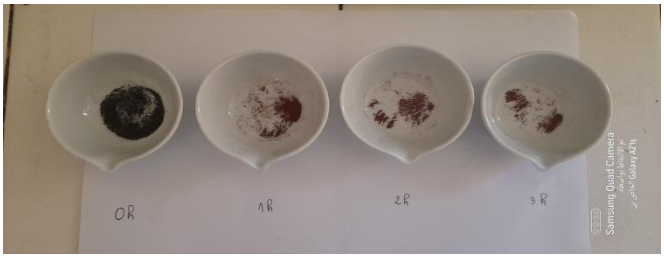

Fig. IV.1*:Photos of the prepared powders for 0-3 hours post heat treatment as mentioned in the figure.*

IV.2.3. Characterization of iron oxide nanoparticles:

The band gap energy has been estimated through the optical transmittance spectrum using (UV–VIS spectrophotometer Shimadzu, Model 1800) operating in the wavelength 200-900nm range. To find out iron oxides crystal structure XRD technique was employed using X ray diffract meter (Rigaku Miniflex 600) apparatus with a Cu-Kα (λ = 1.5406 Å) operating in the 2θ angles from 10° to 90°range, and (30keV, 30mA) as conditions of X-ray generation. Iron oxide NPs chemical bonds were determined by their vibration in 400-4000cm^{-1} infrared spectrum which was scanned by a device (Shimadzu IR-Infinity 1). The surface investigation was done with scanning electron microscopy (SEM-TESCAN VEGA 3), all measurements are done at room temperature.

IV.3. Results and discussion:

IV.3.1. Structural properties:

Fig. IV.2 shows the XRD patterns of powders annealed for (0–3hours) at 500°C. XRD peaks show the existence of tow irons oxides before annealing treatment, which are namely magnetite and wüstite. Also, after annealing treatment it was shown that the existence of three iron oxides: maghemite, hematite and β-Fe_2O_3 having the structural as follow:

- Magnetite (Fe_3O_4) having a orthorhombic crystalline structure according to JCPDS No:0.1-076-0958 where peaks appear at 2θ: 16.127°, 20.924°, 31.1794, 32.564°, 33.885°, 37.664°, 38.823°, 42.425°, 43.448° and 54.423° correspond to lattice plane of *(021), (220), (304), (314), (420), (423), (334), (522), (440)* and *(363)*, respectively*;*
- Wüstite ($Fe_{0.872}O$) having a cubic crystalline structure according to JCPDS No: 01-071-161 where peaks appear at 2θ: 16.127°, 20.924°, 31.1794, 32.564°, 33.885°, 37.664°, 38.823°, 42.425° and 43.448° correspond to lattice plane of *(040), (431), (462), (364), (311), (744), (291), (0010)* and *(493)*, respectively*;*
- Gamma phase, maghemite *(γ*-Fe_2O_3) having a tetragonal crystalline structure according to JCPDS No: 00-025-1402 where peaks appear at 2θ: 30.313°, 35.715°, 43.421°, 53.934°, 57.423°, 63.065°and 74.634° correspond to lattice plane of *(206*), *(119*), *(0012*), *(2212*), *(1115*), *(4012*), and *(3315*), respectively;

- Alpha phase, hematite (α-Fe_2O_3) having a rhombohedra crystalline structure JCPDS No: 01-089-0598 where peaks appear at 2θ: 33.065°, 35.715°, 40.765°, 49.578°and 64.121° correspond to lattice plane of (*104*), (*110*), (*113*), (*024*) and (*300*), respectively;
- Beta phase, (β-Fe_2O_3) having a cubic crystalline structure according to JCPDS No: 00-039-0238 appears peaks at 2θ: 33.065°, 38.304° and 55.307° correspond to lattice plane of (*222*), (*400*), and (*440*), respectively.

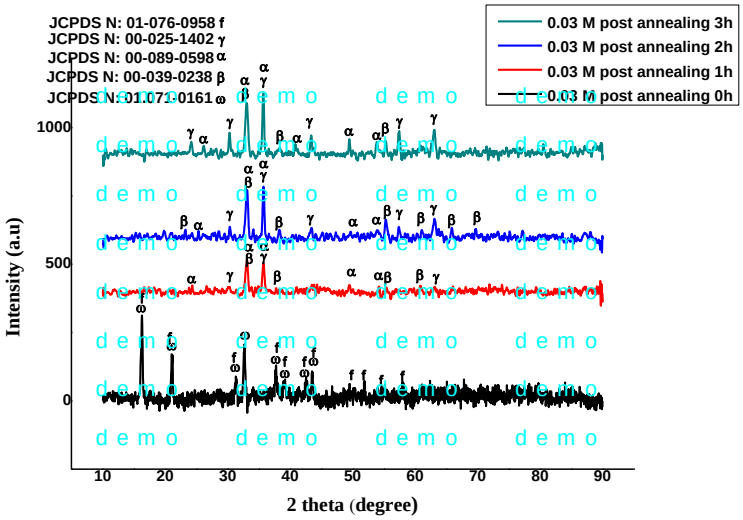

Fig. IV. 2*: *X-ray diffraction patterns of samples prepared with 0.03M as function of heat annealing.(γ: γ-Fe_2O_3, α: α-Fe_2O_3, β: β-Fe_2O_3 w:FeOand f:Fe_3O_4).

The lattice constants (*a*, *b* and *c*), for the orthorhombic phase structure, are determined by the following relations[1]:

$$2d_{hkl}\,sin(\theta) = n\lambda \qquad \text{(IV.1)}$$

and

$$\frac{1}{d_{hkl}^2} = \frac{h^2}{a^2} + \frac{l^2}{b^2} + \frac{k^2}{c^2} \qquad \text{(IV.2)}$$

Where d_{hkl} and (*hkl*) are the inter-planer distance and Miller indices, respectively.

The values of lattice parameter '*a*','*b*' and '*c*' are listed in Table IV.1. Values of *a*, *b* and *c* are (*a* =11.7762 Å, *b* =11.8431 Å, *c* = 16.5842 Å) for instance in the case of sample treated 0h; they are the most close to the values of standard JCPDS data card, (a_0 =11.8680 Å, b_0 =11.8510 Å, c_0 = 16.7520 Å).

The lattices constant (*a* and *c*), for the tetragonal phase structure, are determined by the given relations [2]:

$$\frac{1}{d_{hkl}{}^2} = \frac{h^2+k^2}{a^2} + \frac{l^2}{c^2} \qquad \text{(IV.3)}$$

The values of lattice parameter '*a*' and 'c' are listed in Table IV.1. Values of *a* and *c* are ($a = b$ = 8.3383Å, c = 25.0151Å) for instance in the case of sample treated 1h; they are the most close to the values of standard JCPDS data card, ($a_0 = b_0$ = 8.3400Å, c_0= 25.0200Å).

The lattice constants (*a* and *c*), for the rhombohedral phase structure, are determined by the following relations [3]:

$$\frac{1}{d_{hkl}{}^2} = \frac{4}{3a^2}\left(h^2 + k^2 + hk\right) + \frac{l^2}{c^2} \qquad \text{(IV.4)}$$

The values of lattice parameter '*a*' and 'c' are illustrated in Table IV.1. Values of *a* and *c* are ($a = b$ = 5.0238Å and c = 13.8311Å) in the case of 2*h* sample; they are the most close to the values of standard JCPDS ($a_0 = b_0$= 5.0380 Å and c_0 = 13.7760Å).

For the beta phase structure, the lattice constant *a* is determined by the following relations of cubic unit [4]:

$$\frac{1}{d_{hkl}{}^2} = \frac{1}{a^2}(h^2 + k^2 + l^2) \qquad \text{(IV.5)}$$

Values of *a*, are illustrated in Table IV.1. In the case of 2*h* annealed sample, *a* is about 9.3776Å which is closely equal to 9.4040 Å of the JCPDS No: 00-039-0238 one.

The crystalline sizes of the powders, with different concentrations, are given in Table IV.1, They are calculated using Scherrer's formula [5]:

$$D = \frac{0.9\,\lambda}{\beta cos\theta} \qquad \text{(IV–6)}$$

where D, β, λ, and θ are the crystallite size, the full width at half-maximum (FWHM) of diffraction peaks, the X-ray wavelength (Cu k_α = 1.5406 Å) and Bragg angle, respectively.

Before annealing, it was noticed that the formation of nano iron oxides Fe_3O_4 and wüstite. But after annealing, a change in the iron oxide phase, (ie Fe_2O_3) is formed in its three phases: alpha, gamma, and beta as revealed in the XRD spectra.

Also, it was noticed that the maghemite and hematite peaks increase in length with the increase in the annealing period of time while the beta peaks decrease with the increase in the annealing period, this is explained by the transformation of beta phase to gamma and alpha phase. In comparison between gamma and alpha phase one can see that the growth of gamma is more enhanced (see grain size in table IV.1).

Table IV.1 : Crystallographic data obtained from XRD.

Hours	Phases present	Grain size (nm)	Calculated d (Å)	Standard d (Å)	Lattice parameter *a* (Å), *b* (Å), *c* (Å)
0 *h*	FeO	35.06793	2.73825	2.74895	*a* = *b* = c = 21.38641
	Fe_3O_4	41.39835	1.68051	1.68479	*a* =11.7762, *b* =11.8431, c = 16.5842
1 *h*	γ-Fe_2O_3	22.91024	2.51698	2.51400	*a*= *b* = 8.3374, *c* =24.9904
	α-Fe_2O_3	20.43640	2.70409	2.70329	*a* = *b* =5.0339, *c* = 13.7892
	β-Fe_2O_3	17.96256	2.70409	2.71400	*a* = 9.3671
2 *h*	γ-Fe_2O_3	25. 70405	2.51190	2.51400	*a*= *b* = 8.3310, *c* =24.9931
	α-Fe_2O_3	24.55748	2.70699	2.70329	*a* = *b* = 5.0238, *c* = 13.8311
	β-Fe_2O_3	23.41092	2.70699	2.71400	*a* = 9.3773
3 *h*	γ-Fe_2O_3	35.35561	2.51852	2.51400	*a* = *b* = 8.3266, *c* = 24.9799
	α-Fe_2O_3	28.16851	2.70396	2.70329	*a* = *b* = 5.0212, *c* = 13.8483
	β-Fe_2O_3	20.98141	2.70396	2.71400	*a* = 9.3668

IV.3.2. Surface morphology:

The surface morphology of iron oxide powders are studied using SEM images, at same magnification of 5µm for the concentration of FeCl3, 0.03M and different period of post annealing :(a) 0h, (b) 1h, (c) 2h, and (d) 3h. Fig. 3a-d shows the results with concentration of $FeCl_3$, 0.03 and different period of treatment, respectively. It is clear that iron oxides NPs are mainly present as granules with spherical shaped particles having diameter of about 2.5µm and less. The agglomeration of particles may be due to the association of FeO and Fe2O3 as it was confirmed by XRD for the non-treated sample. After the treatment, they still appear with spherical shaped particles of 0.2µm and some wool. It continued its smallness until having the dimensions of 0.5µm for the treatment of two hours with of course the presence of wool. After three hours of treatment the spherical shaped particles still getting small with complete disappearance of the wool. This smallness may be due to subdivision the big agglomeration of FeO and Fe_2O_3 into others smallest agglomeration of Fe2O3 under different phases. To have idea about the composition of NPs, EDAXs of three samples are reported in this study; they reveal that the samples are composed of iron and oxygen. Atomic rate of oxygen per iron are for the non-treated sample was 35/4 with the presence of C, whereas the treated one and two hours were 2/1 and has 3/1 as

shown in the EDAX tables below (Fig. 3e,f and g), which means a non-stoichiometric composition of the elaborated iron oxides NPs. As it was shown from the XRD study that the co-existence of three types of iron oxides NPs which are *γ, α and β-*Fe_2O_3.

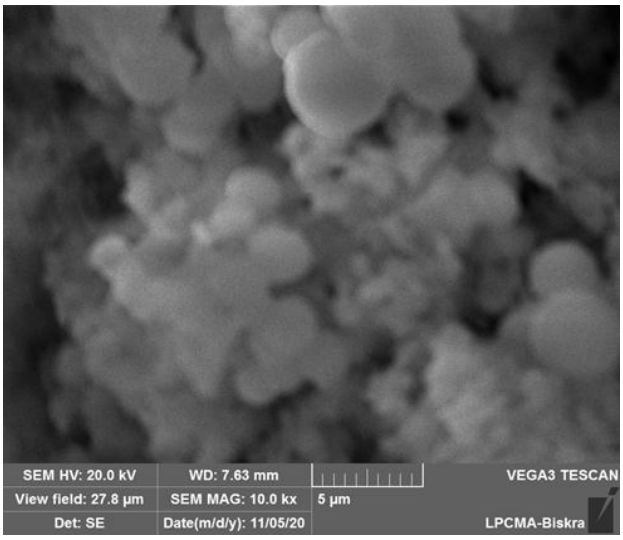
SEM HV: 20.0 kV
WD: 7.63 mm
VEGA3 TESCAN
View field: 27.8 µm
SEM MAG: 10.0 kx
5 µm
Det: SE
Date(m/d/y): 11/05/20
LPCMA-Biskra

(a)

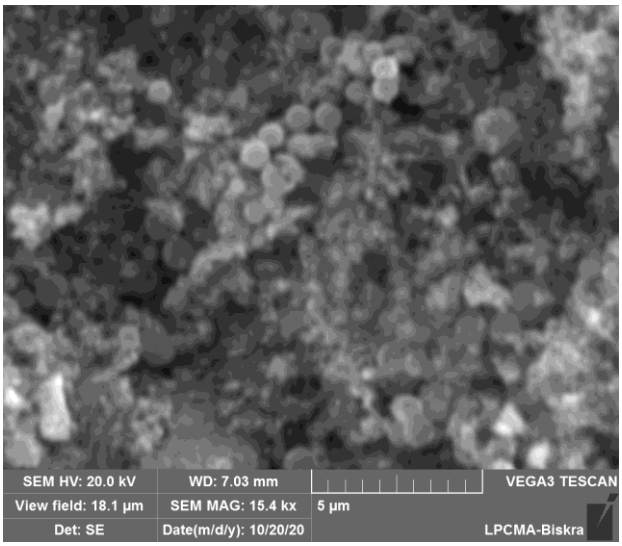
SEM HV: 20.0 kV
WD: 7.03 mm
VEGA3 TESCAN
View field: 18.1 µm
SEM MAG: 15.4 kx
5 µm
Det: SE
Date(m/d/y): 10/20/20
LPCMA-Biskra

(b)

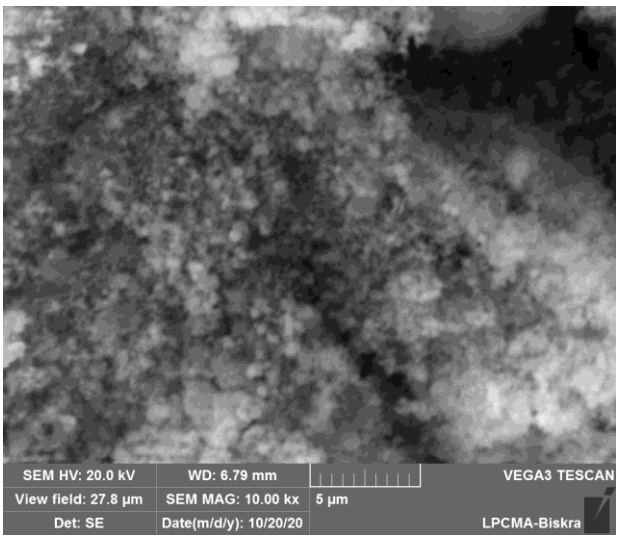
SEM HV: 20.0 kV
WD: 6.79 mm
VEGA3 TESCAN
View field: 27.8 µm
SEM MAG: 10.00 kx
5 µm
Det: SE
Date(m/d/y): 10/20/20
LPCMA-Biskra

(c)

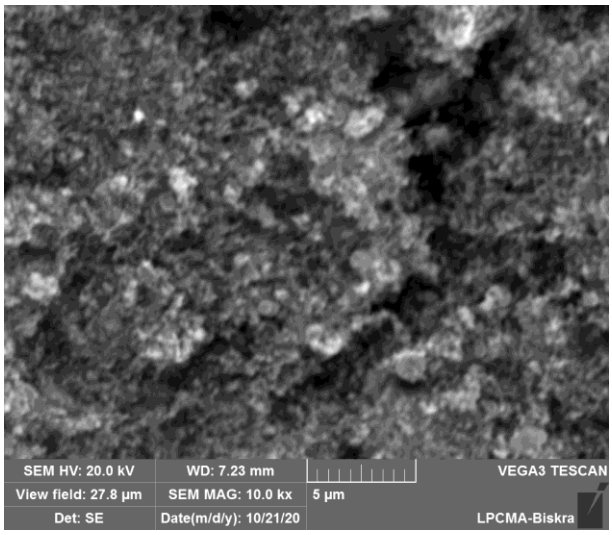

(d)

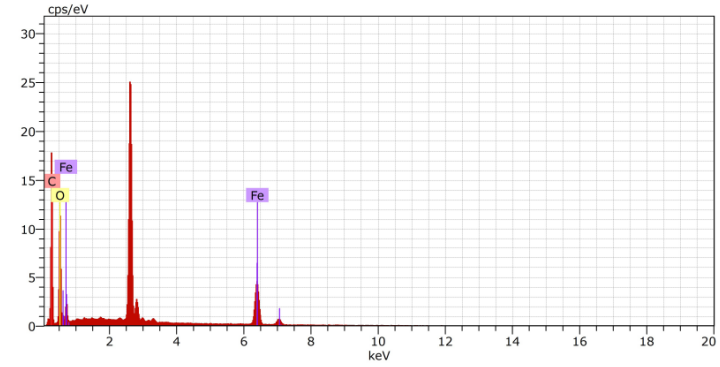

Acquisition Date:11/5/2020 12:33:52 PM HV:20.0kV Puls th.:10.07kcps

El	AN	Series	unn. C [wt.%]	norm. C [wt.%]	Atom. C [at.%]	Error (1 Sigma) [wt.%]
C	6	K-series	34.31	47.44	60.37	4.33
O	8	K-series	26.78	37.03	35.38	3.49
Fe	26	K-series	11.24	15.54	4.25	0.34
		Total:	72.33	100.00	100.00	

(e)

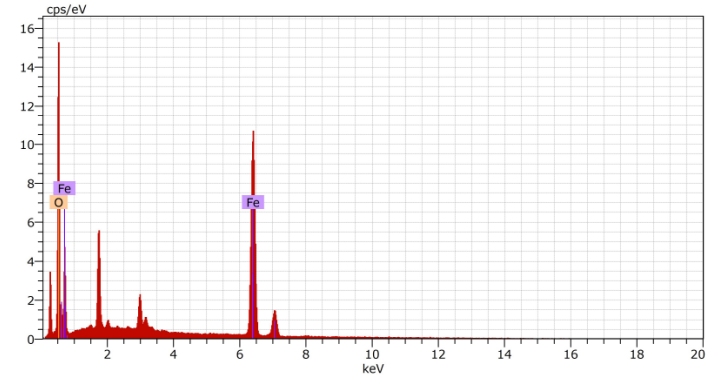

Acquisition Date:2/19/2019 9:45:27 AM HV:20.0kV Puls th.:8.28kcps

El	AN	Series	unn. C [wt.%]	norm. C [wt.%]	Atom. C [at.%]	Error (1 Sigma) [wt.%]
Fe	26	K-series	43.15	65.50	35.23	1.18
O	8	K-series	22.73	34.50	64.77	2.83
		Total:	65.87	100.00	100.00	

(f)

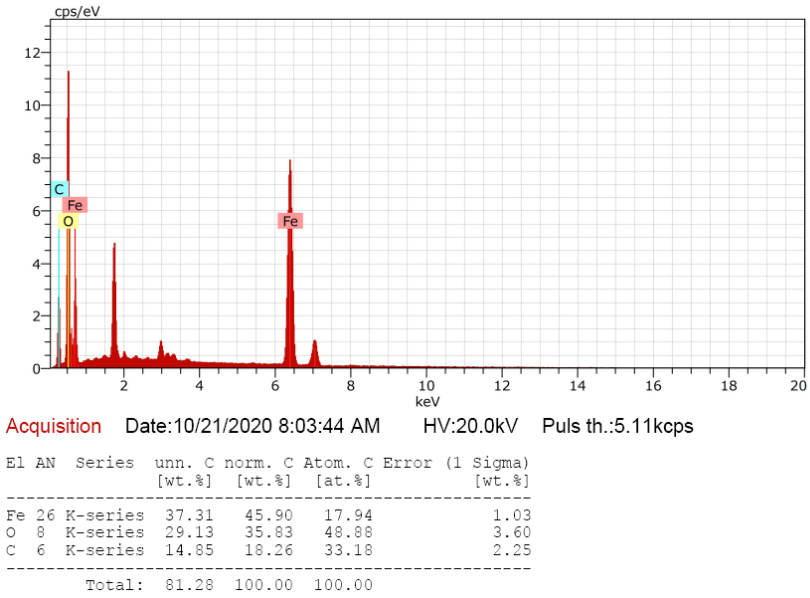

El	AN	Series	unn. C [wt.%]	norm. C [wt.%]	Atom. C [at.%]	Error (1 Sigma) [wt.%]
Fe	26	K-series	37.31	45.90	17.94	1.03
O	8	K-series	29.13	35.83	48.88	3.60
C	6	K-series	14.85	18.26	33.18	2.25
		Total:	81.28	100.00	100.00	

(g)

Figure IV.3: *SEM images of post annealing oxides NPs for 0.03M samples powders: (a) 0h, (b) 1h, (c) 2h and (d) 3h and EDAX of (0-2h) treated samples (e) 0h, (f) 1h, and (g) 2h.*

IV.3.3. Optical properties:

In order to investigate the band gap of the iron oxide NPs powders after the treatment, As in the Chaptre III, Tauc's relation is used [6]:

$$\boldsymbol{\alpha h\nu = A(h\nu - Eg)^{n}} \qquad \text{(IV.7)}$$

where α, *h*, *v,* and E_g are the absorption parameter, Planck constant, the photon frequency and gap energy, respectively, whereas ***A*** is a constant and ***n*** is taken 1/2 based on the consideration that γ-Fe_2O_3 and α-Fe_2O_3 have direct gap [6–7]. The optical absorption data was used to generate plots of $(\alpha h\nu)^2$ vs ($h\nu$), as shown in Fig. IV.4 leading to band gap energy which was estimated by extrapolating the straight line of $(\alpha h\nu)^2$ to $h\nu$ axis $(\alpha h\nu)^2=0$.

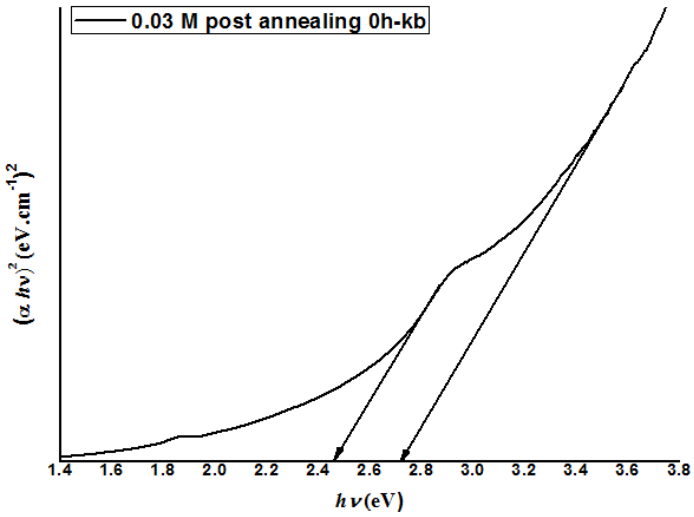
0.03 M post annealing 0h-kb
$(\alpha h\nu)^2$ (eV.cm^{-1})^2
1.4 1.6 1.8 2.0 2.2 2.4 2.6 2.8 3.0 3.2 3.4 3.6 3.8
$h\nu$(eV)

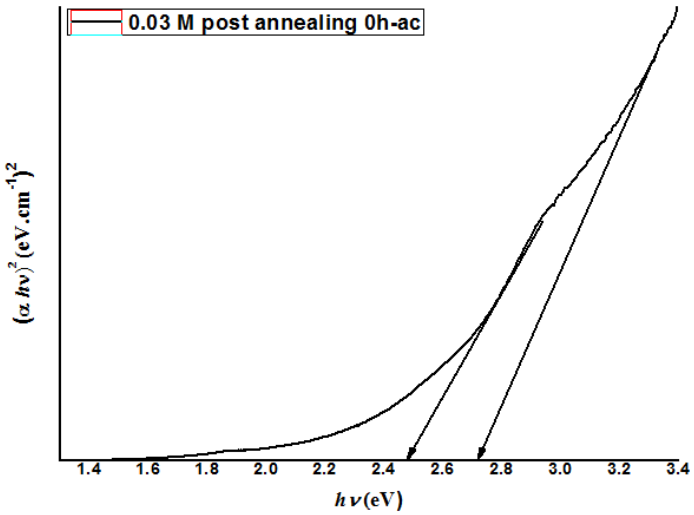
0.03 M post annealing 0h-ac
$(\alpha h\nu)^2$ (eV.cm^{-1})^2
1.4 1.6 1.8 2.0 2.2 2.4 2.6 2.8 3.0 3.2 3.4
$h\nu$(eV)

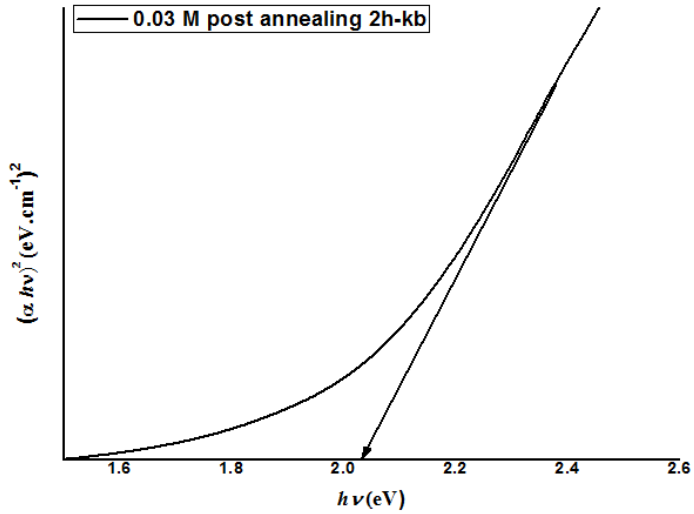
0.03 M post annealing 2h-kb
$(\alpha h\nu)^2$ (eV.cm^{-1})^2
1.6 1.8 2.0 2.2 2.4 2.6
$h\nu$(eV)

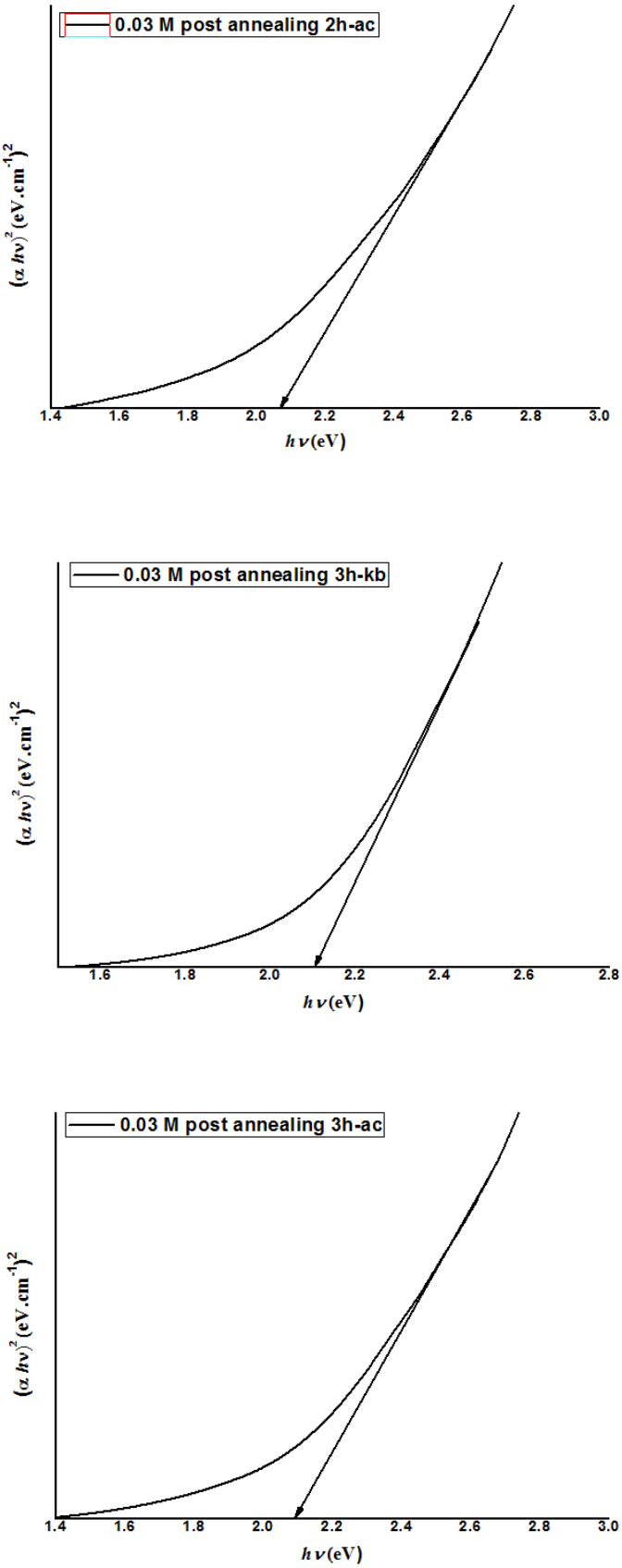

Fig. IV.4: *Band gaps estimation from Tauc's relation for iron oxide NPs powders for samples with the time of annealing.*

Visual results were obtained using two techniques: The first technique is that we used the KBr salt by making tablets of KBr salt with a mass of 0.198g KBr and . 0.002g of NPs powder the considered sample composted under disc shape (1cm x1mm). Whereas for the second technique, acetone acid was used by taking a volume10ml of it with the addition of 0.002g from NPs powder of the considered sample and then placing it in the ultrason apparatus for agitation.

Optical values of the elaborated samples are given in Table IV.2. As shown in Fig. IV.4, leading to band gap energy for first technique of 2.454eV and 2.723eV for the as-deposited sample wüstite and magnetite respectively and 2.326, 2.031, and 2.103eV for the annealed samples during 1, 2, and 3hours, respectively for NPs F_2O_3.

For the second technique the band gaps were about of 2.475eV and 2.711eV for the as-deposited sample wüstite and magnetite, respectively and 2.358, 2.065, and 2.090eV for the annealed samples during 1, 2, and 3hours, respectively for NPs F_2O_3. The results were very similar for both techniques. And their values are in agreement with several previous works [7-12] .

Table IV.2 : Optical gap of green synthesized iron oxide NPs.

E_g(ev)	0*h*	1*h*	2*h*	3*h*
E_g(ev)/KBr	2.454 for *w*-2.723 for *f*	2.326 for F_2O_3	2.031 for F_2O_3	2.103 for F_2O_3
E_g(ev)/Ac	2.475 for *w* -2.711 for f	2.358 for F_2O_3	2.065 for F_2O_3	2.090 for F_2O_3

IV.3.4. FTIR:

Fig. IV.5 shows FTIR spectra of the synthesized samples with different post annealing. Characteristics bands of metal oxides are in general lied in 400-1200 cm^{-1} . The bands related to Fe-O lattice vibration are the range of 400-900 cm^{-1}. Spectrum before annealing shows tow bonds at 423 and 459cm^{-1} are related wüstite and at 442 and 572cm^{-1} related magnetite[13].

As it was exhibited in the figure after annealing bonds appearance at 562, 634 and 694cm^{-1} which are related to maghemite phase formation, bonds at 410, 442,480 and 572cm^{-1} describe the formation of hematite phase [11,14] and bonds at 528cm^{-1} is related at beta phase [15], such results are consistent with those of XRD ones. The bond at 1107 cm^{-1} is related to C-O out of plane bond [16] which may be attributed a residual carbon from manipulation.

The absorption bands due to atmospheric water absorption are detected with a maximum at 3431 cm-1, due to the expansion vibration of O-H and at 1631 cm^{-1} corresponding to the bending vibration O-H of the atmospheric absorbed water [11].

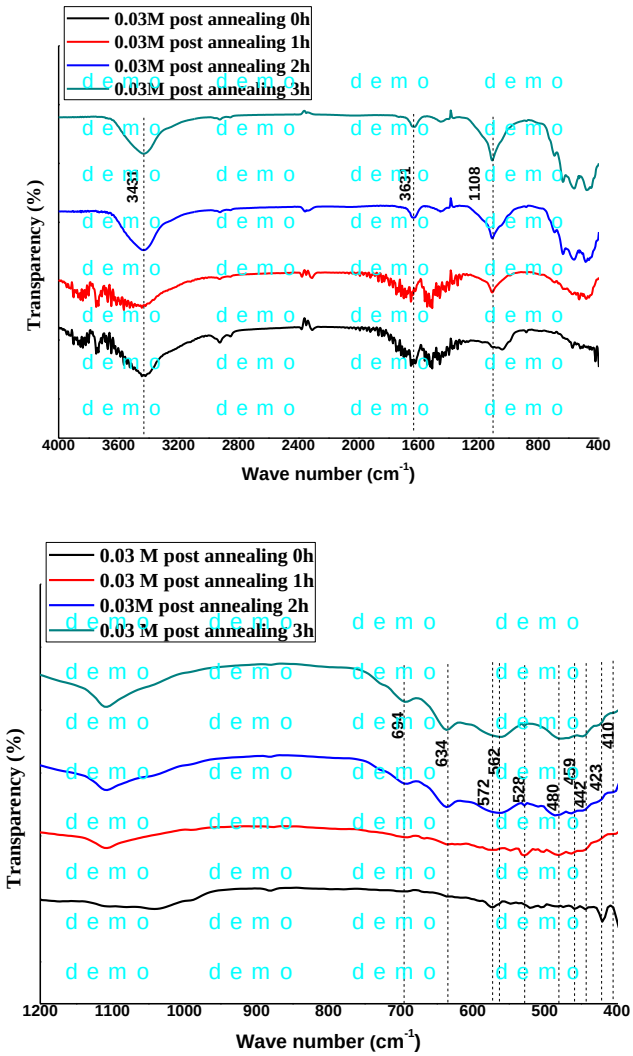

Figure IV.5: *FTIR spectrum of iron oxide NPs powders for (0–3 hours) post annealing at 500°C.*

IV.4. Conclusion:

In this work, Iron oxide NPs powders were synthesized by green synthesis method using the extract of PHEONIXDACTYLIFERA L with a triple iron chlorine solution. The effect of annealing time within the extract and the 500°C annealed products for (0–3) hours for concentration 0.03M on their structural and optical properties have been studied. XRD analyses avowed the formation tow of irons oxides before annealing treatment, namely magnetite and wüstite. Also show the

existence of three iron oxide essentials compounds after annealing treatment, namely maghemite, hematite and β-Fe_2O_3 for concentrations 0.03M. SEM images showed that all samples having spheric shaped particles. With direct band gap in the range of 2.031-2.732eV. FTIR spectrum affirms the abundance of Fe-O bond.

References

[1] Mondal, A., and S. Ram. "Reconstructive phase formation of ZrO2 nanoparticles in a new orthorhombic crystal structure from an energized porous ZrO (OH) 2• xH2O precursor." Ceramics International 30.2 (2004): 239-249.

[2] Kittel, Charles. Introduction to solid state physics. John Wiley & sons, inc, 2005.

[3] Dghoughi, L., et al. "Physico-chemical, optical and electrochemical properties of iron oxide thin films prepared by spray pyrolysis." Applied Surface Science 253.4 (2006): 1823-1829.

[4] Sadanandan, A. K., and M. Jacob Mathew. "A novel route for the synthesis of gamma phased Fe2O3nano particles through polymer assisted spray pyrolysis." AIP Conference Proceedings. Vol. 2162. No. 1. AIP Publishing LLC, 2019.

[5] Abdullah, Mikrajuddin, and Khairurrijal Khairurrijal. "Derivation of Scherrer relation using an approach in basic physics course." Jurnal Nanosains & Nanoteknologi 1.1 (2009): 28-32.

[6] Tauc, J., Radu Grigorovici, and Anina Vancu. "Optical properties and electronic structure of amorphous germanium." physica status solidi (b) 15.2 (1966): 627-637.

[7] Mallick, P., and B. N. Dash. "X-ray diffraction and UV-visible characterizations of α-Fe2O3 nanoparticles annealed at different temperature." Nanosci. Nanotechnol 3.5 (2013): 130-134.

[8] Goyal, Rajendra N., Davinder Kaur, and Ashish K. Pandey. "Growth and characterization of iron oxide nano crystalline thin films via low-cost ultrasonic spray pyrolysis." Materials Chemistry and Physics 116.2-3 (2009): 638-644.

[9] Liu, Jianxing, He Yang, and Xiangxin Xue. "A new and simple route to prepare γ-Fe2O3 with iron oxide scale." Materials Letters 229 (2018): 156-159.

[10] Wei, Zhiwei, et al. "Preparation and visible-light photo catalytic activity of α-Fe2O3/γ-Fe2O3 magnetic hetero phase photo catalyst." Materials Letters 118 (2014): 107-110.

[11] Ates, Mehmet, et al. "Assessment of impact of α-Fe2O3 and γ-Fe2O3 nanoparticles on phytoplankton species Selenastrumcapricornutum and Nannochloropsisoculata." Environmental toxicology 35.3 (2020): 385-394.

[12] Ahmouda, Kaouthar, et al. "Plant extract FRAP effect on cation vacancies formation in greenly synthesized wüstite (FexO) nanoparticles: A new contribution." Sustainable Chemistry and Pharmacy 25 (2022): 100563.

[13] Radpour, M., S. M. Masoudpanah, and S. Alamolhoda. "Microwave-assisted solution combustion synthesis of Fe3O4 powders." Ceramics International 43.17 (2017): 14756-14762.

[14] Demir, Veysel, et al. "Influence of alpha and gamma-iron oxide nanoparticles on marine microalgae species." Bulletin of environmental contamination and toxicology 95.6 (2015): 752-757.

[15] Aziz, Wisam J., et al. "Synthesis of iron oxide (β-fe2o3) nanoparticles from Iraqi grapes extract and its biomedical application." IOP Conference Series: Materials Science and Engineering. Vol. 881. No. 1. IOP Publishing, 2020.

[16] Khalil, Ali Talha, et al. "Biosynthesis of iron oxide (Fe2O3) nanoparticles via aqueous extracts of Sageretiathea (Osbeck.) and their pharmacognostic properties." Green Chemistry Letters and Reviews 10.4 (2017): 186-201.

General Conclusion

In this work, the synthesis of iron oxide nanoparticles (Fe2O3 NPs) was achieved through a green synthesis method utilizing the extract of Phoenix dactylifera L leaves and a triple iron chloride solution. The impact of salt concentration in the extract on the structural and optical properties of the synthesized nanoparticles was investigated following heat treatment at 500 °C for varying concentrations: 0.01 M, 0.02 M, 0.03 M, and 0.04 M. The XRD analyses revealed the formation of three essential compounds of iron oxide NPs, namely maghemite phase, hematite phase, and β-Fe2O3, with the grain size ranging from 17.96 to 37.40 nm, depending on the iron chloride concentration. The nanoparticles exhibited a spherical shape, as observed in the SEM images, with a direct band gap ranging from 2.162 to 2.358 eV. The presence of Fe-O bonds was confirmed through FTIR spectroscopy.

We note that the yield is inversely proportional to the size of the prepared nanoparticles. The highest yield of 47.27% was obtained for the sample with a concentration of 0.03 M and a crystal size of 20.43 nm. This was followed by a yield of 37.98% for the sample with a concentration of 0.02 M and a crystal size of 22.24 nm. The sample with a concentration of 0.04 M and a crystal size of 26.89 nm exhibited a yield of 28.79%. Finally, the sample with a concentration of 0.01 M and a crystal size of 31.32 nm had a yield of 17.55%.

Furthermore, the effect of annealing time within the extract and subsequent annealing at 500 °C for 0-3 hours, specifically for a concentration of 0.03 M, was investigated. Prior to annealing, the XRD analysis indicated the presence of two iron oxide compounds, magnetite and wüstite. However, after annealing treatment, three iron oxide compounds, maghemite, hematite, and β-Fe2O3, were detected for the 0.03 M concentration. Similar to the previous samples, the SEM images revealed spherical-shaped particles. The direct band gap for these nanoparticles ranged from 2.031 to 2.732 eV, and the FTIR spectrum affirmed the abundance of Fe-O bonds.

In conclusion, the findings of this work research demonstrate the viability of green synthesis using Phoenix dactylifera L leaf extract for the production of Fe2O3 nanoparticles, offering promising prospects for their application in diverse fields. The

yield of the nanoparticles was found to be inversely proportional to their size, with the highest yield obtained for the sample with the smallest crystal size. These results contribute to the understanding of the synthesis and properties of iron oxide nanoparticles and provide insights for further research in this field.

Appendices

Appendix A: code reference 00-025-1402 of Maghemite

Name and formula

Reference code:	1402-025-00
Mineral name:	Maghemite-*Q* ‹syn
Compound name:	Iron Oxide
PDF index name:	Iron Oxide
Empirical formula:	Fe_2O_3
Chemical formula:	Fe_2O_3

Crystallographic parameters

Crystal system:	Tetragonal
Space group:	P43212
Space group number:	96
a:(Ŝ)	8.3400
b (?):	8.3400
c (?):	25.0200
Alpha (°):	90.0000
Beta (°):	90.0000
Gamma (°):	90.0000
Volume of cell (10^6 pm^3):	1740.28
Z:	32.00
RIR:	-

Subfiles and quality

Subfiles:	Alloy, metal or intermetalic Common Phase Corrosion Forensic Inorganic Mineral Pharmaceutical
Quality:	Indexed (I(

Comments

Creation Date:	1970-01-01
Modification Date:	1970-01-01

References

Primary reference: Brown., *X-Ray Identification and Crystal Structures of Clay*, (1961)

Other: *Dana's System of Mineralogy, 7th Ed.*, **I**, 708

Peak list

No.	h	k	l	d [A]	2Theta[deg]	I [%]
1	1	0	1	7.91000	11.177	1.0
2	1	0	2	6.94000	12.745	2.0
3	1	0	3	5.90000	15.004	6.0
4	1	1	2	5.33000	16.619	1.0
5	1	1	3	4.82000	18.392	6.0
6	1	0	5	4.29000	20.688	2.0
7	2	0	3	3.73000	23.836	6.0
8	1	1	6	3.40000	26.189	7.0
9	2	0	5	3.20000	27.858	3.0
10	2	0	6	2.95000	30.273	30.0
11	2	1	6	2.78000	32.173	3.0
12	1	0	9	2.63800	33.956	4.0
13	1	1	9	2.51400	35.685	100.0
14	2	2	6	2.40800	37.313	2.0
15	2	0	9	2.31500	38.871	2.0
16	3	1	6	2.23000	40.416	2.0
17	0	0	12	2.08600	43.341	15.0
18	4	0	6	1.86500	48.791	1.0
19	2	1	12	1.82000	50.079	3.0
20	2	2	12	1.70100	53.854	9.0
21	3	0	12	1.67000	54.937	2.0
22	1	1	15	1.60400	57.402	20.0
23	2	0	15	1.55000	59.599	2.0
24	2	1	15	1.52500	60.678	3.0
25	4	0	12	1.47400	63.013	40.0
26	2	0	18	1.31800	71.528	6.0
27	3	3	15	1.27200	74.541	8.0
28	6	2	6	1.25800	75.515	3.0
29	4	4	12	1.20400	79.551	5.0
30	6	2	12	1.11500	87.395	6.0
31	3	1	21	1.08600	90.356	10.0
32	0	0	24	1.04300	95.215	7.0
33	2	2	24	0.98300	103.187	5.0
34	5	1	21	0.96300	106.240	8.0
35	8	4	1	0.93200	111.482	4.0

Stick Pattern

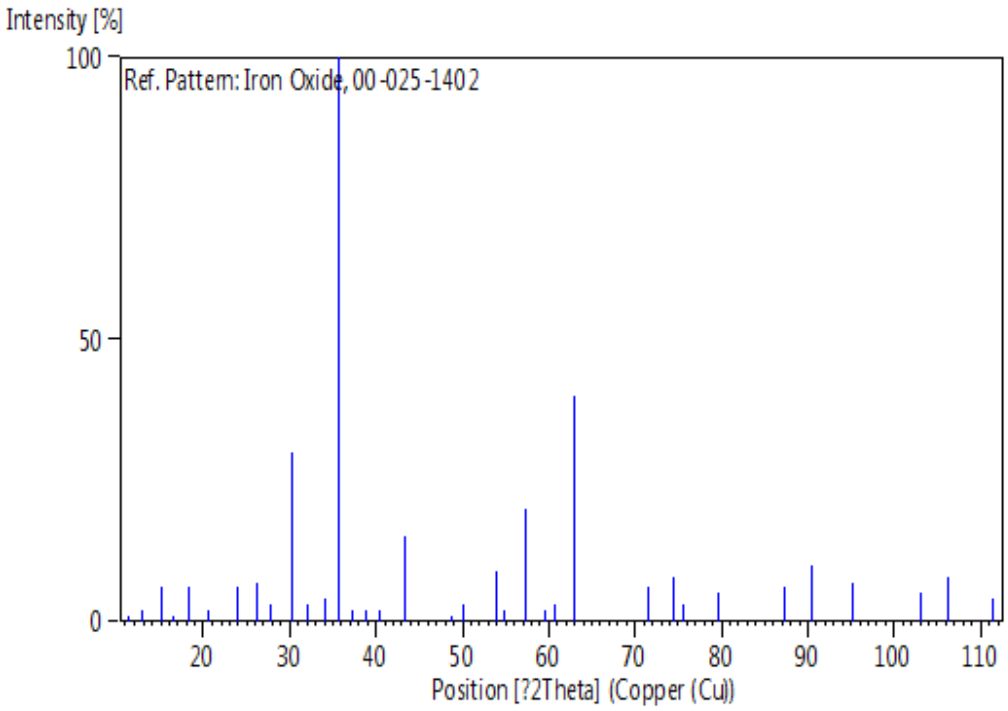

Appendix B: code reference 00-039-0238 of Iron Oxide

Name and formula

Reference code:	0238-039-00
Compound name:	Iron Oxide
PDF index name:	Iron Oxide
Empirical formula:	Fe_2O_3
Chemical formula:	Fe_2O_3

Crystallographic parameters

Crystal system:	Cubic
Space group:	Ia-3
Space group number:	206
a:(Ϙ)	9.4040
b (?):	9.4040
c (?):	9.4040
Alpha (°):	90.0000
Beta (°):	90.0000
Gamma (°):	90.0000
Volume of cell (10^6 pm^3):	831.64
Z:	16.00
RIR:	-

Subfiles and quality

Subfiles:	Alloy, metal or intermetalic Corrosion Inorganic Pharmaceutical
Quality:	Indexed (I(

Comments

Creation Date:	1970-01-01
Modification Date:	1970-01-01
Sample Preparation:	3NaFe (SO = $_2$($_4$$Na_3$Fe (SO + $_3$($_4$β-Fe_2O3 + $_3$SO . $_3$Cell parameter generated by least squares refinement
Unit Cell:	Reference reports: a=9.398(1). Additional Patterns: To replace 00-032-0469 .

References

Primary reference: Ikeda, Y., Takana, M., Bando, Y ،.*Bull. Inst. Chem. Res., Kyoto Univ*(1986) ،249 ،**64** ،.

Peak list

No.	h	k	l	d [A]	2Theta[deg]	I [%]
1.0		18.866		4.70000	0	0	2	1
15.0		23.156		3.83800	1	1	2	2
100.0		32.977		2.71400	2	2	2	3
1.0		35.700		2.51300	1	2	3	4
16.0		38.269		2.35000	0	0	4	5
5.0		40.682		2.21600	1	1	4	6
1.0		42.995		2.10200	0	2	4	7
10.0		45.187		2.00500	2	3	3	8
1.0		47.332		1.91900	2	2	4	9
9.0		49.383		1.84400	1	3	4	10
4.0		53.312		1.71700	1	2	5	11
40.0		55.223		1.66200	0	4	4	12
2.0		57.091		1.61200	3	3	4	13
1.0		58.888		1.56700	0	0	6	14
5.0		60.678		1.52500	1	1	6	15
1.0		62.399		1.48700	0	2	6	16
4.0		64.129		1.45100	1	4	5	17
19.0		65.860		1.41700	2	2	6	18
5.0		67.473		1.38700	1	3	6	19
3.0		69.173		1.35700	4	4	4	20
1.0		70.785		1.33000	3	4	5	21
1.0		72.416		1.30400	0	4	6	22
3.0		73.997		1.28000	1	2	7	23
1.0		75.586		1.25700	2	4	6	24
1.0		80.353		1.19400	1	5	6	25
3.0		81.842		1.17600	0	0	8	26
2.0		83.395		1.15800	1	1	8	27
1.0		84.925		1.14100	0	2	8	28
1.0		86.522		1.12400	3	5	6	29
1.0		88.089		1.10800	0	6	6	30
2.0		89.620		1.09300	1	3	8	31
4.0		91.107		1.07900	2	6	6	32
2.0		94.264		1.05100	0	4	8	33
1.0		95.821		1.03800	3	3	8	34
1.0		97.316		1.02600	2	4	8	35
1.0		98.869		1.01400	1	2	9	36
1.0		100.486		1.00200	4	6	6	37
1.0		102.027		0.99100	1	5	8	38
1.0		105.145		0.97000	2	3	9	39
3.0		106.880		0.95900	4	4	8	40
1.0		108.357		0.95000	1	4	9	41
1.0		110.063		0.94000	0	6	8	42
1.0		111.663		0.93100	2	7	7	43
2.0		113.329		0.92200	2	6	8	44
1.0		115.066		0.91300	3	4	9	45
2.0		116.676		0.90500	6	6	6	46
2.0		118.568		0.89600	2	5	9	47

Stick Pattern

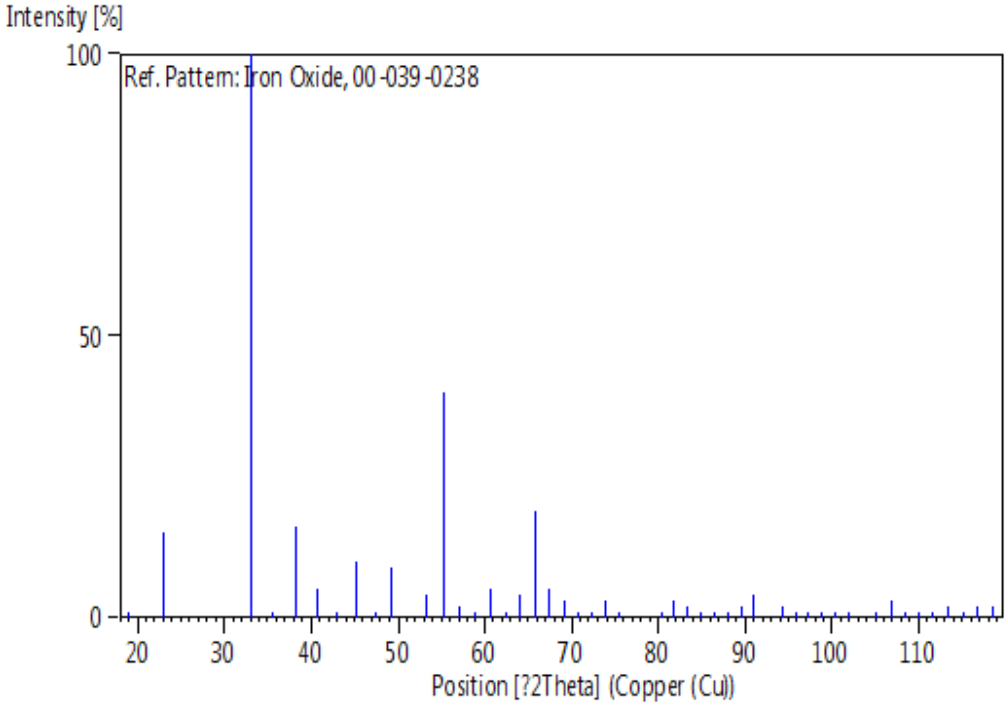

Appendix C: code reference 01-089-0598 of Hematite

Name and formula

Reference code:	0598-089-01
Mineral name:	Hematite, syn
Compound name:	Iron Oxide
Common name:	Iron(III) oxide - alpha
ICSD name:	Iron Oxide
Empirical formula:	Fe_2O_3
Chemical formula:	Fe_2O_3

Crystallographic parameters

Crystal system:	Rhombohedral
Space group:	R-3c
Space group number:	167
a:(Ŝ)	5.0380
b (?):	5.0380
c (?):	13.7760
Alpha (°):	90.0000
Beta (°):	90.0000
Gamma (°):	120.0000
Calculated density (g/cm^3):	5.25
Volume of cell (10^6 pm^3):	302.81
Z:	6.00
RIR:	3.20

Subfiles and quality

Subfiles:	Alloy, metal or intermetalic Corrosion ICSD Pattern Inorganic Mineral Pharmaceutical
Quality:	Calculated (C(

Comments

ICSD collection code:	082136
Creation Date:	1970-01-01
Modification Date:	1970-01-01

ICSD Collection Code: 082136
Calculated Pattern Original Remarks: X-ray diffraction (powder (
Calculated Pattern Original Remarks: REM K Sample mechanically activated in a ball mill under
Calculated Pattern Original Remarks: REM Aratmosphere for 15 min and than annealed in air at 673 K
Temperature Factor: ITF
Additional Patterns: See PDF 01-089-2810. Effect of mechanical activation on the real structure and reactivity of iron(III) oxide with corundum-type structure. e c (R3-CH). A2X3 .

References

Primary reference: *Calculated from ICSD using POWD-12 ++*
Structure: Sadykov, V.A., Isupova, L.A., Tsybulya, S.V., Cherepanova, S.V., Litvak, G.S., Burgina, E.B., Kustova, G.N., Kolomiichuk, V.N., Ivanov, V.P., Paukshtis, E.A., Golovin, A.V., Avvakumov, E.G ،.*J. Solid State Chem*(1996) ،191 ،**123** ،.

Peak list

No.	h	k	l	d [A]	2Theta[deg]	I [%]
29.7		24.126		3.68582	2	1	0	1
100.0		33.112		2.70329	4	0	1	2
69.0		35.612		2.51900	0	1	1	3
2.2		39.205		2.29600	6	0	0	4
19.1		40.826		2.20853	3	1	1	5
2.5		43.479		2.07971	2	0	2	6
29.8		49.414		1.84291	4	2	0	7
40.3		53.995		1.69689	6	1	1	8
0.2		56.127		1.63738	1	1	2	9
6.4		57.490		1.60176	2	2	1	10
22.5		62.383		1.48736	4	1	2	11
23.5		63.964		1.45435	0	0	3	12
0.1		65.966		1.41498	5	2	1	13
2.0		69.487		1.35164	8	0	2	14
7.8		71.800		1.31367	10	0	1	15
1.8		72.154		1.30810	9	1	1	16
4.6		75.409		1.25950	0	2	2	17
1.7		77.654		1.22861	6	3	0	18
0.9		78.718		1.21464	3	2	2	19
0.1		79.437		1.20545	1	3	1	20
2.8		80.595		1.19102	2	1	3	21
3.9		82.801		1.16479	10	2	0	22
0.2		84.288		1.14800	12	0	0	23
5.6		84.864		1.14167	4	3	1	24
5.2		88.465		1.10426	6	2	2	25

Stick Pattern

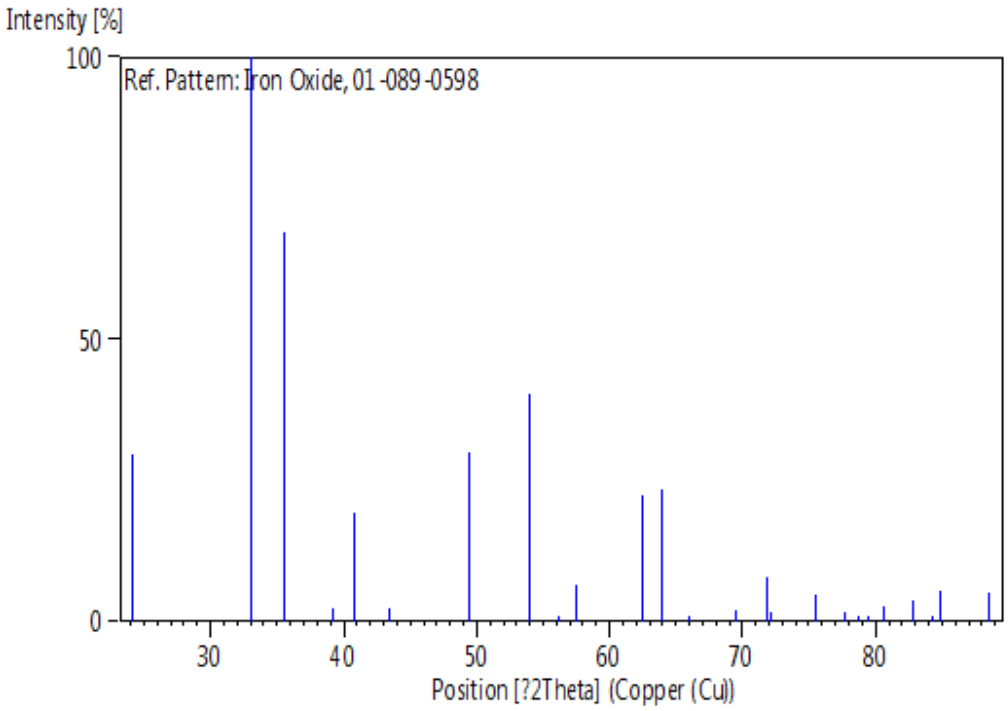

Appendix D: code reference 01-076-0958 of Magnetite

Name and formula

Reference code:	0958-076-01
Mineral name:	Magnetite
Compound name:	Iron Oxide
Common name:	Iron diiron(III) oxide
ICSD name:	Iron Oxide
Empirical formula:	Fe_3O_4
Chemical formula:	Fe_3O_4

Crystallographic parameters

Crystal system:	Orthorhombic
Space group:	Pmc21
Space group number:	26
a:(Ŝ)	11.8680
b (?):	11.8510
c (?):	16.7520
Alpha (°):	90.0000
Beta (°):	90.0000
Gamma (°):	90.0000
Calculated density (g/cm^3):	1.30
Volume of cell (10^6 pm^3):	2356.13
Z:	8.00
RIR:	2.03

Status, subfiles and quality

Status:	Diffraction data collected at non ambient temperature
Subfiles:	Alloy, metal or intermetalic Corrosion ICSD Pattern Inorganic Mineral
Quality:	Calculated (C(

Comments

ICSD collection code:	035003
Creation Date:	1970-01-01
Modification Date:	1970-01-01

ICSD Collection Code: 035003
Temperature of Data Collection: REM TEM -263 C
Test from ICSD: At least one TF implausible
Temperature Factor: ITF
Additional Patterns: See PDF 01-076-0957. Structure of magnetite Fe3 O4 below the verwey transition temperature. c6 b8 a8 (PMC21). AB2X4 .

References

Primary reference: *Calculated from ICSD using POWD-12*(1997) ،++
Structure: Iizumi, M., Koetzle, T.F., Shirane, G., Chikazumi, S., Matsui, M., Todo, S ،.*Acta Crystallogr., Sec. B*(1982) ،2121 ،**38** ،

Peak list

No.	h	k	l	d [A]	2Theta[deg]	I [%]
0.1	7.454	11.85100	0	0	1	1
0.1	9.133	9.67479	1	1	0	2
0.3	10.541	8.38593	0	1	1	3
0.1	11.792	7.49882	1	1	1	4
6.8	12.932	6.84004	2	0	1	5
18.5	14.939	5.92550	2	1	1	6
0.1	15.852	5.58632	1	2	0	7
0.1	16.695	5.30601	0	1	2	8
0.4	17.532	5.05438	1	2	1	9
0.1	18.325	4.83740	2	0	2	10
100.0	19.791	4.48232	2	1	2	11
37.3	21.172	4.19296	0	2	2	12
0.5	21.833	4.06749	1	2	2	13
0.1	22.489	3.95033	0	3	0	14
0.3	23.115	3.84470	1	3	0	15
11.2	23.728	3.74675	0	3	1	16
0.4	24.871	3.57710	2	0	3	17
5.2	26.020	3.42165	4	0	2	18
0.1	26.563	3.35294	3	2	2	19
0.1	27.095	3.28832	0	3	2	20
0.3	27.622	3.22675	1	3	2	21
39.0	29.151	3.06089	2	2	3	22
38.7	30.095	2.96700	0	0	4	23
1.1	30.619	2.91747	1	4	0	24
0.2	31.097	2.87366	4	0	3	25
0.4	31.549	2.83352	3	2	3	26
8.6	31.999	2.79473	4	1	3	27
12.4	32.930	2.71780	6	0	1	28
3.3	33.758	2.65300	0	2	4	29
0.1	34.221	2.61815	1	4	2	30
0.1	34.655	2.58634	4	2	3	31
0.1	35.083	2.55577	3	4	1	32
0.1	35.505	2.52633	6	0	2	33
0.1	35.898	2.49961	3	3	3	34
0.3	36.331	2.47081	6	1	2	35
0.1	37.105	2.42101	4	0	4	36

0.1	37.529	2.39462	3	2	4	37
0.1	37.930	2.37020	4	1	4	38
0.1	38.312	2.34749	5	2	3	39
2.5	38.697	2.32499	4	3	3	40
0.1	39.112	2.30127	1	5	1	41
6.1	39.472	2.28110	6	0	3	42
3.3	40.206	2.24116	4	2	4	43
0.1	40.970	2.20111	0	5	2	44
0.4	41.338	2.18235	1	5	2	45
7.5	42.384	2.13090	2	2	5	46
14.7	43.114	2.09648	0	4	4	47
0.9	43.467	2.08025	1	4	4	48
0.2	43.823	2.06419	4	3	4	49
0.2	44.193	2.04776	3	5	2	50
2.7	44.500	2.03435	4	1	5	51
7.4	45.210	2.00401	6	1	4	52
2.0	45.921	1.97466	8	0	2	53
0.1	46.596	1.94758	4	5	2	54
0.4	46.909	1.93532	1	6	1	55
0.1	47.245	1.92235	2	6	0	56
4.4	47.831	1.90015	2	1	6	57
4.5	47.897	1.89770	2	6	1	58
21.7	48.558	1.87337	0	6	2	59
0.3	49.509	1.83960	3	6	1	60
2.1	49.785	1.83005	4	3	5	61
7.8	50.438	1.80787	6	3	4	62
0.7	51.022	1.78855	4	0	6	63
0.7	51.086	1.78645	4	6	0	64
0.1	51.704	1.76656	8	2	3	65
0.2	51.993	1.75740	1	6	3	66
4.2	52.863	1.73051	2	3	6	67
3.0	53.519	1.71083	8	0	4	68
0.1	54.045	1.69543	0	0	7	69
0.1	54.106	1.69366	4	5	4	70
0.3	54.414	1.68479	3	6	3	71
0.1	54.681	1.67719	0	5	5	72
2.5	55.342	1.65871	10	0	1	73
1.9	55.912	1.64315	8	2	4	74
0.1	56.477	1.62804	4	3	6	75
0.2	56.754	1.62075	5	5	4	76
0.1	57.083	1.61219	10	0	2	77
3.0	57.559	1.60000	2	2	7	78
3.0	57.632	1.59813	2	7	2	79
0.1	58.481	1.57695	7	4	4	80
0.1	58.781	1.56960	4	7	0	81
0.3	59.056	1.56296	3	7	2	82
1.4	59.306	1.55697	4	5	5	83
4.2	59.872	1.54358	6	4	5	84
1.1	60.407	1.53118	4	4	6	85
0.1	61.014	1.51741	8	2	5	86
0.1	61.253	1.51206	1	6	5	87
2.3	62.061	1.49429	2	5	6	88
2.3	62.563	1.48350	0	0	8	89
3.5	62.654	1.48156	8	4	4	90
1.9	62.892	1.47654	5	4	6	91

0.4	63.107	1.47201	0	1	8	92
0.3	63.441	1.46507	3	6	5	93
0.7	63.676	1.46023	4	3	7	94
3.2	64.287	1.44782	10	1	4	95
0.5	64.783	1.43792	8	0	6	96
0.3	64.992	1.43380	1	2	8	97
0.1	65.306	1.42768	4	5	6	98
0.1	65.580	1.42237	7	3	6	99

Stick Pattern

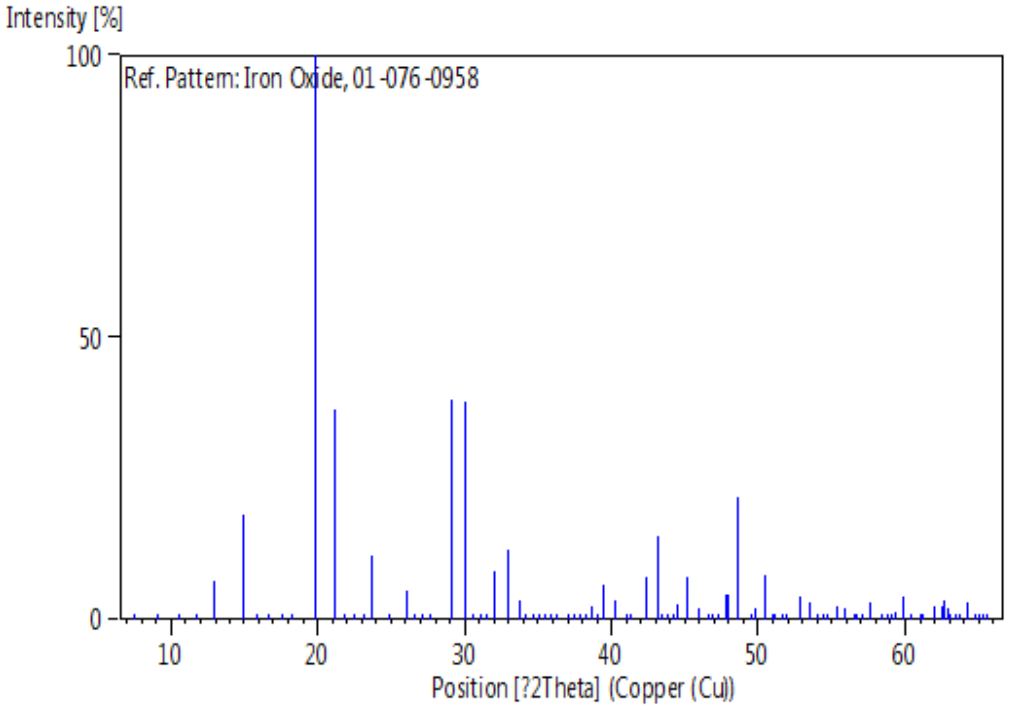

Appendix F: code reference 01-071-0161 of Wüstite

Name and formula

Reference code:	0161-071-01
Mineral name:	Wüstite, syn
Compound name:	Iron Oxide
ICSD name:	Iron Oxide
Empirical formula:	$Fe_{0.872}O$
Chemical formula:	$Fe_{0.872}O$

Crystallographic parameters

Crystal system:	Orthorhombic
Space group:	Abm2
Space group number:	39
a:(ʕ)	21.4700
b (?):	21.4700
c (?):	21.4700
Alpha (°):	90.0000
Beta (°):	90.0000
Gamma (°):	90.0000
Calculated density (g/cm^3):	5.35
Volume of cell (10^6 pm^3):	9896.83
Z:	500.00
RIR:	1.66

Subfiles and quality

Subfiles:	Alloy, metal or intermetalic Corrosion ICSD Pattern Inorganic Mineral
Quality:	Calculated (C(

Comments

ICSD collection code:	000981
Creation Date:	1970-01-01
Modification Date:	1970-01-01
ICSD Collection Code:	000981
Test from ICSD:	Calc. density unusual but tolerable

Calculated Pattern Original Remarks:	REM B Distances Fe20-Fe24, Fe26-Fe68, Fe47-Fe61, Fe60-Fe67, Fe46-061, Fe54-073 were too short, vacancies discussion
Sample Preparation:	Quenched from 1273 K
Test from ICSD:	At least one TF missing
Additional Patterns:	See PDF 00-046-1312 (cubic subcell with a/5 (
Calculated Pattern Original Remarks:	y(Fe46, Fe54) were misprinted as O, z(Fe61) as .195, z(Fe67) as .295, Fe57 taken as Fe24, Fe24 and Fe68 deleted
Test from ICSD:	Published coordinates have been corrected. Decomposition and ordering in Fe(1-x) O. d90 c50 b a (ABM2). A107X125 .

References

Primary reference:	*Calculated from ICSD using POWD-12 ++*
Structure:	Andersson, B., Sleines, J.O ،.*Acta Crystallogr., Sec. A* ،268 ،**33** ، (1977)

Peak list

No.	h	k	l	d [A]	2Theta[deg]	I [%]
0.1		4.112		21.47000	0	0	1	1
3.5		7.126		12.39570	1	1	1	2
19.6		8.230		10.73500	2	0	0	3
4.6		9.203		9.60168	2	0	1	4
17.8		10.084		8.76509	1	1	2	5
1.5		11.649		7.59079	2	2	0	6
1.1		12.358		7.15667	0	0	3	7
1.7		13.668		6.47345	3	1	1	8
1.5		14.279		6.19785	2	2	2	9
1.1		14.865		5.95471	2	0	3	10
7.0		15.430		5.73810	1	3	2	11
2.1		16.502		5.36750	0	4	0	12
4.4		17.014		5.20724	4	0	1	13
3.4		17.511		5.06053	1	1	4	14
1.8		17.995		4.92556	3	1	3	15
2.8		18.466		4.80084	2	4	0	16
1.4		18.926		4.68514	2	4	1	17
0.7		19.376		4.57742	3	3	2	18
1.0		20.246		4.38255	2	4	2	19
0.8		20.668		4.29400	4	0	3	20
2.2		21.082		4.21061	1	3	4	21
1.7		21.489		4.13190	5	1	1	22
2.2		22.280		3.98688	2	4	3	23
0.3		22.666		3.91987	1	5	2	24
0.5		23.420		3.79540	4	4	0	25
1.6		23.788		3.73745	4	4	1	26
0.5		24.151		3.68207	3	3	4	27
3.9		24.509		3.62909	3	1	5	28
0.6		24.863		3.57833	0	0	6	29
0.6		25.211		3.52965	6	0	1	30
1.5		25.555		3.48289	1	1	6	31
3.9		26.231		3.39471	2	6	0	32

5.0	26.562	3.35305	2	6	1	33
0.6	26.890	3.31289	1	5	4	34
1.6	27.215	3.27414	3	3	5	35
1.6	27.536	3.23672	2	6	2	36
0.3	27.853	3.20056	2	4	5	37
1.3	28.167	3.16558	3	1	6	38
0.2	28.786	3.09893	4	4	4	39
2.5	29.091	3.06714	2	6	3	40
0.9	29.393	3.03632	3	5	4	41
2.5	29.692	3.00640	7	1	1	42
1.0	29.988	2.97735	0	4	6	43
1.2	30.282	2.94913	4	6	1	44
3.6	30.573	2.92170	1	7	2	45
2.5	31.148	2.86905	2	6	4	46
0.7	31.432	2.84377	2	2	7	47
10.1	31.994	2.79516	5	3	5	48
4.9	32.546	2.74895	4	6	3	49
1.8	32.819	2.72669	3	7	2	50
5.3	33.360	2.68375	0	8	0	51
1.5	33.627	2.66303	8	0	1	52
3.0	33.893	2.64277	1	1	8	53
3.0	34.156	2.62298	7	3	3	54
2.0	34.418	2.60362	2	8	0	55
2.1	34.678	2.58468	4	2	7	56
0.5	34.936	2.56616	3	5	6	57
3.2	35.448	2.53026	2	8	2	58
3.2	35.702	2.51287	8	0	3	59
3.8	35.954	2.49584	1	3	8	60
51.0	36.204	2.47914	7	1	5	61
1.2	36.701	2.44673	2	8	3	62
0.3	36.947	2.43100	7	5	2	63
1.1	37.435	2.40042	8	4	0	64
2.4	37.677	2.38556	4	4	7	65
0.5	37.918	2.37096	3	3	8	66
1.4	38.157	2.35664	7	3	5	67
1.9	38.395	2.34257	8	4	2	68
0.9	38.632	2.32875	0	2	9	69
3.4	38.868	2.31517	1	9	2	70
0.3	39.335	2.28871	6	6	4	71
2.9	39.568	2.27582	4	8	3	72
0.6	39.799	2.26314	1	5	8	73
0.7	40.028	2.25067	3	1	9	74
0.2	40.485	2.22634	8	2	5	75
1.7	40.712	2.21446	9	3	2	76
0.6	41.162	2.19127	4	8	4	77
0.5	41.386	2.17995	4	0	9	78
100.0	42.051	2.14700	10	0	0	79
3.2	42.924	2.10531	2	0	10	80
0.8	43.140	2.09526	4	8	5	81
0.5	43.356	2.08535	3	9	4	82
0.4	43.570	2.07558	9	1	5	83
0.8	43.784	2.06595	2	2	10	84
0.6	43.996	2.05645	6	8	3	85
0.3	44.208	2.04708	7	5	6	86
0.2	44.839	2.01973	4	4	9	87

0.4	45.048	2.01085	1	7	8	88
1.1	45.256	2.00209	3	9	5	89
1.2	45.464	1.99344	10	4	0	90
0.6	45.670	1.98490	6	0	9	91
0.5	45.876	1.97647	9	1	6	92
0.7	46.286	1.95993	2	4	10	93
0.7	46.489	1.95182	6	2	9	94
0.4	46.692	1.94380	9	5	4	95
0.3	46.895	1.93588	5	7	7	96
0.7	47.297	1.92034	2	0	11	97
0.9	47.498	1.91270	11	1	2	98
0.2	47.897	1.89770	8	8	0	99
0.7	48.095	1.89033	4	8	7	100
0.6	48.490	1.87584	7	9	1	101
0.7	48.687	1.86872	10	4	4	102
1.0	48.883	1.86169	4	6	9	103
0.9	49.079	1.85473	11	3	2	104

Stick Pattern